

In silico folding and aggregation study of human amylin, an amyloidosis protein

Jiang, Ping

2011

Jiang, P. (2011). In silico folding and aggregation study of human amylin, an amyloidosis protein. Doctoral thesis, Nanyang Technological University, Singapore.

<https://hdl.handle.net/10356/50957>

<https://doi.org/10.32657/10356/50957>

**IN SILICO FOLDING AND AGGREGATION STUDY OF
HUMAN AMYLIN, AN AMYLOIDOSIS PROTEIN**

JIANG PING

School of Biological Sciences

A thesis submitted to the Nanyang Technological University
in fulfillment of the requirement for the degree of
Doctor of Philosophy

2011

Abstract

Abnormal self-assembly of proteins converting their native conformations into β -sheet rich fibrillar structures is the hallmark of several so called “misfolding diseases” including Type 2 Diabetes Mellitus (T2DM), Alzheimer's and Parkinson's diseases, etc. Human islet amyloid polypeptide (hIAPP or amylin) is the major component of amyloid deposits found in the pancreas of 90% T2DM patients. Although extensive studies have been performed in the recent decades, detailed information about hIAPP aggregation and the related pathology remains missing.

The aim of this work is to use computational methodologies to understand (1) the mechanism underlying the abnormal structural transition; (2) how the other molecules modulate the process either as catalysts or anti-aggregation factors. Several amyloidogenic segments rather than full-length hIAPP were chosen as peptide models to compare with their nonamyloidogenic counterparts of rodent species. Even for these short peptide models thorough conformational sampling is still a tough issue. Thus an enhanced sampling computational method – replica exchange molecular dynamics (REMD), was adopted in most simulations

To resolve the multifaceted characteristics of hIAPP aggregation, multiple systems comprising of pure peptide, peptide-lipid, peptide-compound, or peptide-protein have been constructed and undergone extensive simulations. The aggregation behaviors of pure peptides were studied to understand aggregation mechanism and the impacts of sequence variation. In the early stage of peptide aggregation, a dual-path mechanism was clearly observed in our simulations. One path referred to as “reptation

mechanism”, which was observed in experiments with higher peptide concentrations, predominates over the other detachment/re-association path which is believed to occur at lower peptide concentrations. The aggregation-prone activity of a peptide can be completely reversed by sequence variation, especially by proline substitution. In addition to pure peptide systems, interactions between the peptides and other molecules including lipid (a catalyst), resveratrol (a small molecule inhibitor), and insulin (a protein inhibitor) were studied with the aim of acquiring more pathologically related information. The aggregation process of hIAPP segments can be promoted by lipid binding. In the peptide-lipid system we found that a DOPC lipid molecule selectively interacts with hydrophobic patches on a low-level peptide oligomer and prevents them from dissociation. Lipid binding enables the overall complex to enhance its thermal stability and thereby pushes it towards a higher level aggregate. In another peptide-compound system, as a small molecule inhibitor, resveratrol molecules were found to be capable of blocking inter-sheet side chain stacking. The compounds redistribute the oligomer species by eliminating species in a double-layered β -sheet arrangement which are regarded as competent seeds for fibrillar elongation. Insulin is known as a protein inhibitor of IAPP aggregation even in the presence of aggregation catalyst – cellular membranes. To a great extent, interactions of IAPP segments with insulin resemble that with membrane, which leads to a putative inhibitory mechanism that the competition between the two entities for binding to IAPP eliminates the enrichment effect on membranes and the consequent peptide aggregation.

Our studies on the aggregation mechanism deepen the understanding of the early stage of amyloid formation on the atomic level. The acceleration of aggregation

induced by a lipid molecule provides insights into the catalysis activity of membranes and the cytotoxicity to cellular membranes as well. Detailed interactions of IAPP with small molecule inhibitors and a protein inhibitor will be useful to develop inhibitors with higher efficacy to amyloid aggregation and toxicity.

Acknowledgement

It is a pleasure to thank the many people who made this thesis possible.

First and foremost, I wish to express my deep and sincere gratitude to my supervisor Assist Prof. Mu Yuguang. He is a talent scientist with serious attitude and insistent enthusiasm for science. He is a good mentor who is always available for providing advice on my messy projects and always patient to answer many naive questions. Mathematics and physics become so easy when he explains them vividly. His insight into the confusions during projects inspired me to think further and deeper. He offered me opportunities to attend many conferences, academic visiting, and workshops. The precious experience he shared in academic writing, presentation, and searching literature was of great help. This thesis was never going to be finished if without him.

I wish to thank all my colleagues in the computational biology lab at School of Biological Sciences (SBS). Dr. Xu Weixin presented me the background of my projects and we had many inspiring discussions on the project. Mr. Yang Ye demonstrated how to use GROMACS when I knew nothing about simulation. Dr. Lin Xin helped me clear out the mathematical algorithm behind those complex methodologies. Mr. Li Weifeng explained to me the annoying equations in quantum mechanics, and helped me out with the free energy calculation. Thanks also go to two junior graduate students Ms. Han Nanyu and Mr. Zhang Tong who have kindly shared their knowledge and techniques in bioinformatics and other basic disciplines of biology. At last, I would like to thank all these colleagues for their good suggestions on my projects and encouragements during thesis writing.

I would like to present my special thanks to our collaborators from the lab of A/Prof. Konstantin Pervushin at SBS. A/Prof. Pervushin kindly directed the simulation setup to correlate with experimental data. Mr. Wei Lei had conducted most NMR and AFM experiments on the project of amyloid aggregation. Ms. Bai Yang performed NMR experiments on another project of antimicrobial peptides. Without their hard work and collaboration, we cannot do a good work on these projects.

I want to thank all the group members from Prof. Philippe Derreumaux from Institut de Biologie Physico-Chimique (IBPC) for their kind help with using OPEP package. Prof. Derreumaux helped me with choosing the project topic and revised the simulation setup. A/Prof. Samuela Pasquali helped me analyze the preliminary results and amend the system setup. Ms. Yasmine Chebaro taught me the usage of OPEP and analysis tools. I am also grateful to their warm welcome when I visited their lab in Paris.

My special thanks go to my family for their faith in me all the time and their first support for me to pursue doctoral degree in Singapore.

Finally, I would like to thank Nanyang Technological University for the financial support and School of Biological Sciences for the academic opportunities offered during my PhD study.

Abbreviations

aa	amino acid
A β	Amyloid β peptide
ACE	acetyl
AFM	atomic force microscopy
APM	added peptide monomers
BPTI	bovine pancreatic trypsin inhibitor
BSO	β -sheet oligomer
CLO	collapsed oligomer
CR	congo red
DOPC	dioleoyl phosphatidylcholine
dPCA	dihedral angle principal component analysis
DSSP	define secondary structure of proteins
<i>E. coli</i>	<i>Escherichia coli</i>
EM	electron micrograph
ER	endoplasmic reticulum
FTIR	Fourier transform infrared spectroscopy
GB	generalized born
GROMACS	Groningen machine for chemical simulations
hIAPP	human islet amyloid polypeptide
IAPP	islet amyloid polypeptide
kJ/mol	kilo joule per mole
MD	molecular dynamics
MM	molecular mechanics
MM-GBSA	molecular mechanics – generalized born surface area
NCC	nucleated conformational conversion
NME	N-methyl
NMR	nuclear magnetic resonance
ns	nanosecond
OPLSAA	optimized potentials for liquid simulations all atom
PBP	preformed β peptides
PCA	principal component analysis

PCM	polarizable continuum model
PDB	protein data bank
PME	Particle Mesh Ewald
PG	phosphatidylglycerol
POPG	palmitoyl oleoyl phosphatidylglycerol
PS	phosphatidylserine
ps	picosecond
REM	replica exchange method
REMD	replica exchange molecular dynamics
R _g	radius of gyration
rIAPP	rat islet amyloid polypeptide
RIP	residue interface propensity
RMSD	root mean square deviation
SASA	solvent accessible surface area
SPC	simple point charge
ssNMR	solid-state nuclear magnetic resonance
SS	secondary structure
SSP	secondary structure propensity
T2DM	type 2 diabetes mellitus
ThT	thioflavin T
TI	thermodynamic integration
μs	microsecond

Contents

Abstract	i
Abbreviations	vi
Contents	viii
List of Figures	xi
List of Tables.....	xiv
1. Introduction	1
1.1. Protein Misfolding Diseases	1
1.2. Structure of Amyloid Fibrils Derived from hIAPP.....	3
1.3. Sequence Variation between Rodent and Human IAPP	7
1.4. Aggregation Mechanism	8
1.5. Nature of Amyloid Cytotoxicity	14
1.6. Inhibitors of Aggregation and Toxicity.....	18
1.7. Research Objectives	20
2. Computational Methodologies	22
2.1. Molecular Modeling and Molecular Dynamics Simulations.....	22
2.1.1. Mechanical Molecular Representation	23
2.1.2. Potential Energy Function	24
2.1.3. Molecular Dynamics Simulation.....	26
2.1.4. Replica Exchange Molecular Dynamics Simulation.....	28
2.2. Define Secondary Structure of Proteins	30
2.3. Dihedral Angle Principal Component Analysis	31
2.4. Binding Energy Calculation	32
3. Sequence Variation of IAPP ₂₀₋₂₉ Affects Peptide Aggregation.....	33
3.1. Simulation Setup.....	34

3.2.	Divergent Aggregates derived from hIAPP ₂₀₋₂₉ and rIAPP ₂₀₋₂₉ Tetramers	36
3.3.	Orientation and Alignment Patterns of β -Sheet Oligomers.....	38
3.4.	Critical Residues of hIAPP ₂₀₋₂₉ to β -Sheet Formation.....	40
3.5.	Origins of Disrupting Effect of Proline Residues.....	41
3.6.	Conformational Reorganization of Pre-nucleus Oligomers in Two Pathways.....	44
3.7.	Summary.....	49
4.	Lipid Acts as an Aggregation Catalyst	51
4.1.	Lipid Stabilizes Low-Level β -Sheet Oligomers	52
4.2.	Lipid Binds to the Hydrophobic Patches on Peptide Oligomers.....	54
4.3.	Summary.....	56
5.	Inhibitory Effect of Resveratrol on hIAPP ₂₂₋₂₇ Aggregation.....	57
5.1.	Parameterization and Validation of Resveratrol Molecule	58
5.2.	Simulation Setup.....	59
5.3.	Evolution of β -Structures in the Absence/Presence of Resveratrol.....	61
5.4.	Thermodynamic Evidence of the Inhibitory Effects of Resveratrol.....	64
5.5.	Early hIAPP ₂₂₋₂₇ Oligomers in a Double-Layered β -Sheet Arrangement	66
5.6.	Destabilization of Double-Layered β -Sheet Aggregates by Resveratrol	70
5.7.	Characterizing Six Binding Sites of Resveratrol on Pentameric Protofibril	72
5.8.	Inhibitory Activities of Resveratrol by Blocking Inter-sheet Side Chain Contacts.....	75
5.9.	Summary.....	78
6.	pH Effect on IAPP-Insulin Interactions	79
6.1.	Simulation Setup and Clustering Algorithm	80
6.1.1.	Simulation Setup	80

6.1.2. Clustering Algorithm.....	81
6.2. Insulin Binding Preserves Helical hIAPP at Acidic pH.....	83
6.3. Residue Interface Propensities.....	86
6.4. Ensembles of Bound-IAPP at Three Binding Sites on Insulin.....	90
6.5. Residual Contact Maps.....	93
6.6. Characterization of IAPP-Insulin Interfaces.....	95
6.7. Summary.....	99
7. Discussion	101
7.1. Aggregation Activity Modulated by Key Residues.....	101
7.2. Insights into the Mechanism of Short Peptide Self-assembly.....	102
7.3. Resveratrol Redistributes Oligomer Species.....	104
7.4. Insulin and Membrane Compete for Binding to hIAPP.....	107
8. Conclusion.....	111
References	115
Publications	127

List of Figures

Figure 1.1 Gallery of negatively stained insulin fibrils, showing the diversity of fibrillar structures..	3
Figure 1.2 Molecular structural models for the protofilament in hIAPP fibrils with striated ribbon morphologies.....	5
Figure 1.3 Fibrillar model of hIAPP based on crystal structures of NNFGAIL and SSTNVG..	6
Figure 1.4 Sigmoidal self-assembly process.....	10
Figure 1.5 Hypothetical self-assembly pathway of A β	12
Figure 2.1 Schematic diagram of conformational sampling on the potential energy surface by MD simulation.....	28
Figure 3.1 Initial arrangements of four identical hIAPP ₂₀₋₂₉ peptides.....	35
Figure 3.2 Time evolution of percentage of residues in β -sheet structure.....	36
Figure 3.3 dPCA free energy landscapes and representative structures.	37
Figure 3.4 Time evolution of average number of antiparallel and parallel β -bridges..	38
Figure 3.5 β -bridge contact maps.	39
Figure 3.6 Secondary structure propensities of residues.	41
Figure 3.7 Exceptional distributions of ϕ dihedral angles of three proline residues on rIAPP disrupt the continuity of hydrogen bonding network.....	43
Figure 3.8 Time evolution of radius of gyration and total number of atomic contacts.	45
Figure 3.9 Distribution of tetrameric aggregates on different N _B and increasing size of β -sheet oligomers with the increase of N _B	46
Figure 3.10 Parallel-to-antiparallel transition path 1.....	48
Figure 3.11 Parallel-to-antiparallel transition path 2.....	49
Figure 4.1 Molecular structure of DOPC.....	52

Figure 4.2 Distribution of aggregates on different N_B and increasing size of β -sheet oligomers with the increase of N_B in the presence of DOPC.....	53
Figure 4.3 Temperature dependence of averaged number of β -bridges, N_B	53
Figure 4.4 Atomic contacts of DOPC with $C\alpha$ on peptides and secondary structure propensities of residues in hIAPP/lipid system.....	54
Figure 4.5 Representative structures with the largest number of β -bridges in the absence and presence of DOPC.....	55
Figure 5.1 Molecular geometry of trans-resveratrol.....	58
Figure 5.2 Cartoon representation of four initial configurations of seven strands of hIAPP ₂₂₋₂₇	60
Figure 5.3 Time evolution of the β -content of PBP and APM in the absence and presence of resveratrol.....	62
Figure 5.4 Tracing the survival ratio of the preformed hydrogen bonds and its histogram statistics.....	64
Figure 5.5 Temperature-dependent proportion of peptide monomers.....	65
Figure 5.6 Temperature-dependent β -content of peptide aggregates and decomposing β -content into contributions from PBP and APM.....	65
Figure 5.7 Species distribution of β -sheet aggregates and collapsed aggregates.....	68
Figure 5.8 Representative structures of aggregates with double β -sheets in the absence of resveratrol.....	69
Figure 5.9 Representative structures of aggregates with double β -sheets in the presence of resveratrol.....	71
Figure 5.10 Representative structures of aggregates belonging to species 7 in a β -barrel (A) or single-layered configuration (B).....	72
Figure 5.11 Six binding sites of resveratrol molecules on β -sheet hIAPP ₂₂₋₂₇ pentamers and representative structures at each binding site.....	73
Figure 5.12 Correlation of side chain atomic contacts of the primary β -sheet with the rest peptides and with resveratrol molecules.....	76

Figure 5.13 Contact maps of heavy atoms on resveratrol (abscissa) and on the residues of peptides (ordinate).	77
Figure 6.1 Convergence of insulin-IAPP complex simulation by monitoring secondary structure propensity.	84
Figure 6.2 Convergence of isolated peptide simulation by monitoring secondary structure propensity.	85
Figure 6.3 Residue interface propensity (RIP) of residues on insulin.	87
Figure 6.4 Residue interface propensity (RIP) of residues on IAPP segments.	87
Figure 6.5 Chemical shift perturbations of rIAPP in the presence of insulin.	89
Figure 6.6 Residual structures of rIAPP ₁₁₋₁₈ by NMR and rIAPP ₉₋₂₀ -insulin complex by REMD.	90
Figure 6.7 Representative structures displaying the multiple binding sites.	92
Figure 6.8 Residual contact maps for hIAPP(His ⁺)-, hIAPP-, and rIAPP-insulin interactions.	94
Figure 6.9 Salt-bridges and hydrophobic interactions formed between hIAPP(His ⁺) (A), hIAPP (B), rIAPP (C) and insulin.	95
Figure 6.10 Hydrophobic residues on the interfaces of hIAPP(His ⁺)-insulin heterocomplex and insulin dimer.	99
Figure 7.1 Nucleation process through two paths one of which is accelerated by lipid molecules.	103
Figure 7.2 Self-assembly of amyloidogenic peptides and suggested inhibitory mechanism of resveratrol.	105

List of Tables

Table 5.1 Percentages and binding energies of resveratrol at six binding sites of β -sheet pentamers.	74
Table 6.1 Structural and energetic analysis on IAPP-insulin complexes.	96
Table 6.2 Breakdown of interface characteristics of hIAPP(His ⁺)-insulin complex clusters.	97

1. Introduction

1.1. Protein Misfolding Diseases

The mechanism by which a polypeptide chain folds to a unique three-dimensional conformation has been studied for years by experimental and computational methods, but generally still remains a mystery. Nevertheless, the systematically stochastic search of all possible conformations of one polypeptide is considered to be unrealizable in biologically feasible timescale because of the large number of degrees of freedom in an unfolded polypeptide system [1]. In small biological organisms such as *E. coli*, short polypeptides fold spontaneously in a millisecond or microsecond timescale. Living organisms also have evolutionarily selected the favorite peptide sequences for the large proteins to fold at high rate and developed several mechanisms (chaperons, enzymes [2], quality-control system [3], etc.) to increase the correctness and fidelity of folding. In eukaryotic cells, some proteins undergo the major part of folding in cytoplasm after release from ribosome, whereas others fold in specific compartments, such as mitochondria or endoplasmic reticulum (ER). Many newly synthesized proteins initiate folding after translocation into ER where molecular chaperons and folding catalysts are abundant [4]. Molecular chaperons do not themselves increase the rate of certain folding steps (as the catalysts usually do). They rather function to increase the efficiency of the overall process by reducing the probability of other competing pathways, especially aggregation. Some chaperons contain a hydrophobic cavity allowing unfolded or partially folded protein inside to prevent highly nonpolar and amyloidogenic regions from exposing to surrounding proteins. Besides, the quality-control mechanism proves to be efficient by experiments which suggest that a large fraction of

Introduction

polypeptides fail to pass the quality-control check and undergo the degradation process [5].

The biological functions are premised upon the correct folding of proteins. The release into cytoplasm or extracellular secretion of misfolded proteins will give rise to malfunctioning of cells or organs, and hence diseases. Misfolded proteins which can escape all protective mechanisms and form intracellular or extracellular fibrillar amyloid deposits in tissues, have been linked to more than twenty misfolding diseases (or amyloidogenic diseases), namely, Alzheimer's disease, Parkinson's disease, the spongiform encephalopathy and type 2 diabetes [6-8], etc. The phenomenon of universally existing amyloid deposits in patients' tissues once provoked debates on the role as either the cause or the effect that amyloidogenesis plays in misfolding diseases [8]. This is currently still a controversial issue [4] although certain species of amyloidogenic proteins are discovered to be cytotoxic [9, 10].

The ability to form amyloid fibrils is not restricted to a small number of disease-related proteins as it was thought to be, and now it seems to be a generic feature of almost all proteins [11, 12]. The most compelling evidence is that fibrils can be formed by nondisease-related muscle myoglobin [13], and also by *de novo* polyamino acids such as polythreonine or polylysine[14]. Most amyloidogenic proteins have no sequence similarity and their native structures range from globular proteins to randomly coiled peptides. However, the amyloid fibrils that they form contain a uniform cross- β scaffold and consist of several (typically 2-6, Figure 1.1) protofilaments twisted together, with β -strands perpendicular and β -sheet hydrogen

Introduction

bonds parallel to the fibril axis. The fibrils also have the ability to bind specific dyes such as thioflavin T (ThT) and Congo red (CR) for visualization [15]. Although the ability to aggregate into amyloid is generic and probably inherent for distinct proteins, the aggregation rates and conditions greatly vary and correlate with physicochemical properties of proteins such as hydrophobicity, aromaticity, charges, and secondary structure propensities [15].

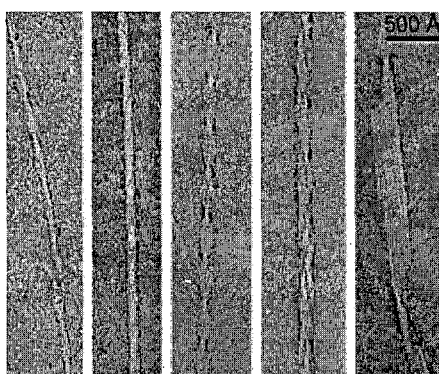


Figure 1.1 Gallery of negatively stained insulin fibrils, showing the diversity of fibrillar structures. The fibrils with different morphologies contain different numbers of filaments. Adapted from Ref [16].

1.2. Structure of Amyloid Fibrils Derived from hIAPP

Type 2 diabetes mellitus (T2DM) is a group of metabolic disorders characterized by insulin resistance, defective insulin secretion, loss of β -cell mass with increased β -cell apoptosis. T2DM is also classified within the localized misfolding diseases due to the amyloid pancreatic deposits found in 90% of the T2DM necropsies. Human islet amyloid polypeptide (hIAPP or amylin) is the major component of amyloid deposits found in pancreas of patients suffering from T2DM (non-insulin-dependent) [17, 18]. Biological function of its native state remains unknown, but hIAPP has

Introduction

been identified as a 37-residue peptide hormone cosecreted with insulin by β -cells of the pancreatic islets [19]. Soluble hIAPP seems to form a random-coil conformation indicating that it may be a natively unfolded protein in aqueous solution [19]. The detailed structural information of hIAPP amyloid fibrils from X-ray crystallography and NMR is limited; however, these techniques have helped to propose two tentative models for the fibrils.

Luca *et al.* described a protocol for preparation of morphologically homogeneous hIAPP fibrils, named as striated ribbons, which leads to high-quality solid-state NMR data [20]. Based on the NMR and EM (electron microscopy) data, tentative structural models (Figure 1.2) were constructed. According to the models, the basic structural unit of the striated ribbons contains two layers of hIAPP peptide, with C2 rotational symmetry about fibril axis (Figure 1.2B). The tertiary fold of monomer is stabilized by side chain contacts (Figure 1.2C, D) and intermolecular conformation within one layer is maintained by in-register parallel hydrogen bonds (Figure 1.2A). Molecules from neighboring layers stack their side chains tightly to increase the rigidity of protofilaments (Figure 1.2B, C, D). The peptide contains two β -strands to form β -sheet core which comprises of residues 8-17 and 28-37; while the most amyloidogenic decapeptide segment, 20-29, resides in the less ordered turn part linking the two β -strands.

Introduction

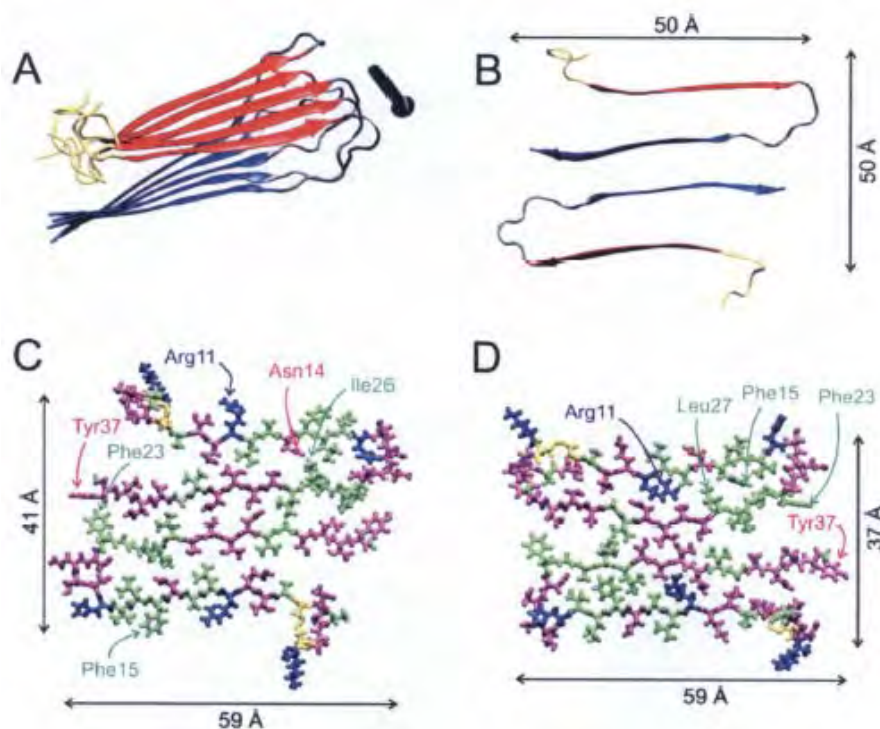


Figure 1.2 Molecular structural models for the protofilament in hIAPP fibrils with striated ribbon morphologies. The structures were generated using restrained Langevin dynamics simulations. A. Ribbon representation of one cross- β -molecular layer, with N- and C-terminal β -strand segments in red and blue, respectively. The black arrow indicates the fibril axis. B. Cross-sectional view of two hIAPP molecules in the protofilament. C, D. All-atom representations of two possible models, with hydrophobic residues in green, polar residues in magenta, positively charged residues in blue and disulfide-linked cysteine residues in yellow. Adapted from ref [20].

Another tentative model of hIAPP amyloid fibril was constructed on the basis of two crystallized segments, N²¹NFGAIL²⁷ and S²⁸STNVG³³, which themselves form amyloid-like fibrils [21]. The atomic structures of these two segments were determined and their topologies in microcrystals were used to fit the most commonly observed full-length hIAPP polymorph [22]. The model fibril has a width of 64Å and crossover distance of 250Å (Figure 1.3C and D). It shows great similarity to the one built based on the NMR data (Figure 1.2) in the spine of the model fibril and only differs slightly in the side chain packing inside the fibril. One hIAPP monomer is in a

Introduction

strand-loop-strand conformation, and its C terminus is stacked on the C terminus of another rotationally symmetrical monomer to form two β -sheets (Figure 1.3A and B). Thus, the fibril contains four parallel β -sheets, the central two constituting the dry steric zipper (Figure 1.3C). Such strand-loop-strand arrangement is common in amyloid fibrils derived from full length peptides and proteins [16, 23-25]. Amyloid fibrils constitute several β -sheet filaments, and the stacking of side chains forms a dewetting steric zipper motif to help stabilize the overall structure of amyloid fibrils.

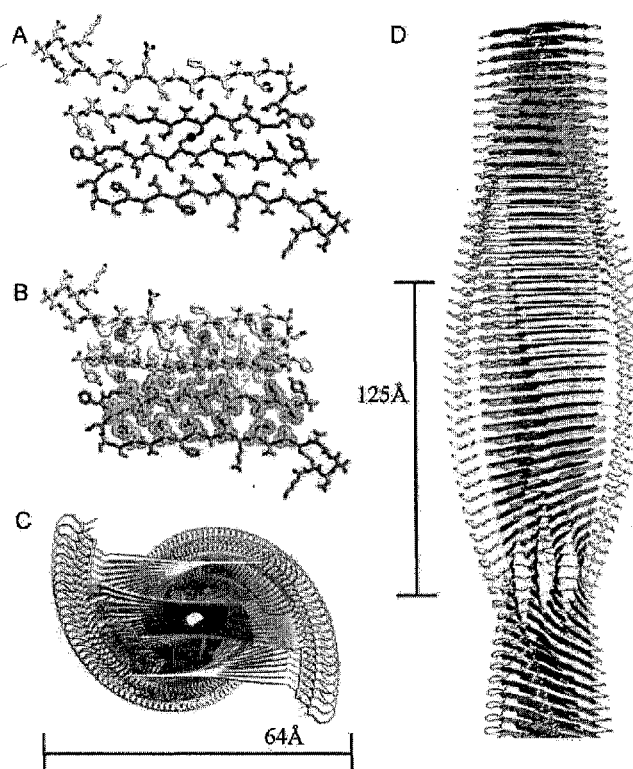


Figure 1.3 Fibrillar model of hIAPP based on crystal structures of NNFGAIL and SSTNVG. A-C. Views down the fibril axis with a diameter of 64 Å. The modeled residues are shown in white and the residues corresponding to the crystal structures are shown in blue for NNFGAIL and green for SSTNVG. D. View perpendicular to the fibril axis of the same fibril with a length of 125 Å (one-quarter of a full turn). This model has a mass per unit length and crossover distance that agrees closely with the experimental value for the most commonly observed polymorphic fibril. Adapted from ref [21].

1.3. Sequence Variation between Rodent and Human IAPP

Humans are not the unique species that develop islet amyloid. Some other species such as non-human primates [26] and cats [27] can form similar amyloid that is closely related to T2DM. And some species (raccoons [28] and the degu) show ability to form amyloid but its association to T2DM is not clear. A segment of hIAPP positioned from amino acid 20 to 29 (hIAPP₂₀₋₂₉) is a strongly amyloidogenic peptide, whose sequence variation seems responsible for differential level of occurrence of amyloid deposits in different species. Five out of six amino acid mutations in rodent IAPP (rIAPP) which lacks the ability to aggregate are located in this decapeptide. The IAPP sequences for human and rodent are shown here. Six residues disparate between the two sequences are highlighted.

KCNTATCATQ¹⁰RLANFLVHSS²⁰NNFGAILSST³⁰NVGSNTY (human IAPP)
 KCNTATCATQ¹⁰RLANFLVRSS²⁰NNLGPVLPPT³⁰NVGSNTY (rodent IAPP)

The segment hIAPP₂₀₋₂₉ itself forms unbranched fibrils with similar properties to full-length hIAPP [29-31]. Thus the segment hIAPP₂₀₋₂₉ and its mutant counterparts have been utilized by a great number of experiments and simulations as an ideal model to study characteristics of amyloid fibrils and mechanism of aggregation. Westermarck *et al.* have synthesized segments 20-29 of various species and unnatural mutants with one or two amino acid substitutions [30]. The segment of hIAPP₂₀₋₂₉ immediately formed a gel (amyloid); comparatively, rIAPP₂₀₋₂₉ did not give rise to fibrils in any of the conditions tested. In the single mutation study, replacement of Ser28 with proline (S28P) almost completely inhibited amyloid formation, indicating its significant role with respect to amyloidogenesis. In contrast, the other four single substitutions (A25P, S29P, F23L, and I26V) had minor or no effects on

Introduction

fibrillogenesis. Rodent IAPPs (rat, mouse, hamster, etc.) have drawn considerable attentions of researchers because they are not only a negative control but a potential inhibitor of amyloid aggregation [32, 33]. The three proline substitutions in rIAPP₂₀₋₂₉ are believed to be at least partially responsible for the lack of amyloid formation ability. A study reported a profound effect of a single-point mutation I26P on amyloidogenesis of hIAPP₂₀₋₂₉ that the mutant abolished amyloid formation [34]. Three aromatic residues (Phe15, Phe23, and Tyr37) were suggested to be critical for amyloid formation. The aggregation was inhibited when they were substituted by alanine residues in alanine-scanning measurements [35] or in computational simulations [36]. However, proline to alanine mutation is not a conserved mutation and alanine substitution changes not only aromaticity but also hydrophobicity and secondary structure propensity of the aromatic residue. Marek *et al.* found in their recent study [37] that aromatic interactions do influence the rate of amyloid formation and fibril morphology but are not absolutely necessary for fibril formation. It is now widely accepted that the reduced aggregation ability of rIAPP is a combinational effects of several mutations rather than one single mutation [38]. Another missense mutation S20G[39] was found to play some roles in early-onset of T2DM in a small population of Japanese and Chinese patients through accelerating formation of fibrils [40]. The small side chain of glycine may fit the tight packing of the turns in the three-dimensional fold of full-length IAPP better according to the aforementioned striated ribbon model [20].

1.4. Aggregation Mechanism

To understand the aggregation mechanism is on the same way to identifying and characterizing all the intermediate aggregate species and the final product in the

Introduction

overall aggregation process. As aforementioned, using amyloid- β -sheet specific dyes such as ThT and CR is a common technique to track aggregation process in *in vitro* experiments. A sigmoidal profile of fibrillogenesis kinetics was widely observed and usually interpreted by a nucleated growth mechanism (Figure 1.4). The sigmoidal aggregation process is characterized by two basic phases - a typical lag phase (nucleation) that is followed by a rapid exponential growth phase (elongation) [41-44]. The lag phase is assumed to be the time required for a “nucleus” of critical size to form (state “N” in Figure 1.4). The nucleus lacks typical fibrillar structures and usually exhibits a mixed coil and β -sheet conformation. This nucleation process is energetically unfavorable conversion of monomers (state “M1”) to a nucleus. Once the nucleus is formed, fibril growth is thought to proceed rapidly by association of monomers (or oligomers) to the nucleus, which is called an elongation process. The lag phase can be shorten or abolished by addition of preformed fibrillar species (states “N” or “PF”) known as “seeding” when the rate of aggregation process is no longer limited by nucleation [43]. In the plateau stage, the fibrillar state is still dynamic, in a balance of dissociation and re-association of free monomers in solution [45].

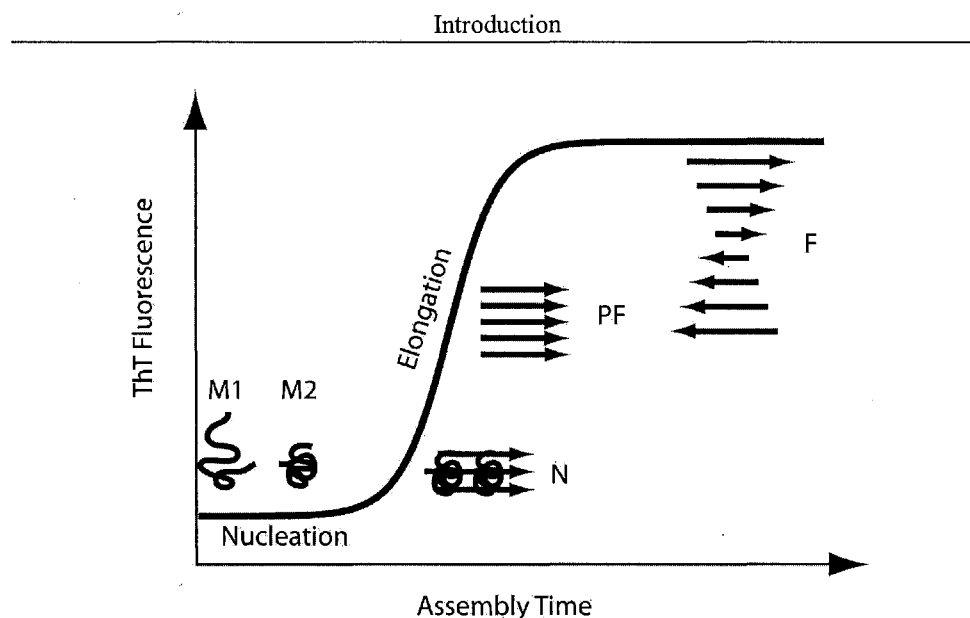


Figure 1.4 Sigmoidal self-assembly process. The process is characterized by two basic phases - a typical lag phase (nucleation) and then a rapid exponential growth phase (elongation). The species emerging during the overall process include monomer of native folded protein or intrinsically disordered protein (M1), monomer in partially unfolded state or any abnormal states which facilitate aggregation (M2), nucleus (N) of critical size which is competent to induce exponential growth, protofibril (PF), and the end product – fibrillar state (F).

The observation of sigmoidal growth relies on the dye-binding characters of amyloid fibrils, however, the dyes are only sensitive to fibrils [46]. Aggregate species of pathological importance, such as aggregation-eligible monomers and transient small oligomers, lack fibrillar structures and are therefore impossible to be detected by this technique. To capture the low level aggregation species and to obtain high resolution structural data of these intermediate aggregates are a new focus of current studies. Two recent attempts to characterize low level aggregates included stabilization of intermediate oligomers by PICUP technology through chemically cross-linking [47] or protein engineering method to trap the aggregates in oligomeric states [48]. These approaches successfully purified oligomers on the basis of their sizes such as dimer, trimer, tetramer, etc. Through these new techniques it became clear that

Introduction

neurotoxicity is linked to pure oligomeric aggregates, but we still do not have a clear structural picture of these species. The purification and characterization of intermediate oligomers is crucial not only for understanding the abnormal self-assembly pathways and inhibitory mechanisms of known inhibitors, but also for designing novel effective inhibitors to target these toxic species [49, 50].

The usage of oligomer-specific antibodies and anti-aggregation protein inhibitors demonstrated a common structural moiety on the oligomeric states among proteins with different sequences and therefore suggest a common aggregation pathway [51, 52]. Besides, the antibody-specific oligomers are pathologically important [53, 54]. These toxicity associated binding sites might involve exposure of moieties that are usually hidden inside globular proteins, such as hydrophobic side chains, or main chain NH and CO groups in an abnormal β -conformation that could lead to the formation of non-native hydrogen bonds [51, 52]. The studies exploring the inhibitory mechanism of small molecule inhibitors also helped elucidate aggregation mechanism. An extensive study of more than 40 anti-aggregation or anti-toxicity compounds was systematically performed by examining their activities to inhibit aggregation of A β peptides (the amyloidogenic peptide associated with Alzheimer's disease) [55]. The inhibitory effects of these compounds were divergent: some inhibited fibrillization but not oligomerization; some only inhibited oligomerization but conversely promoted fibrillization; the rest inhibited both. The conclusion derived here was consistent with many other studies that rather than a single multi-step cascade, amyloid aggregation is most likely through two or more parallel pathways [56]. As shown in Figure 1.5, aggregation might be initiated by collision of oligomers (through I_3 state) or monomer addition to protofibrils (through I_1 state).

Introduction

There are still several controversial issues such as whether any of the parallel pathways is off-pathway to fibrillization, and which pathways are pathologically relevant [56]. To answer these questions, future researches are needed.

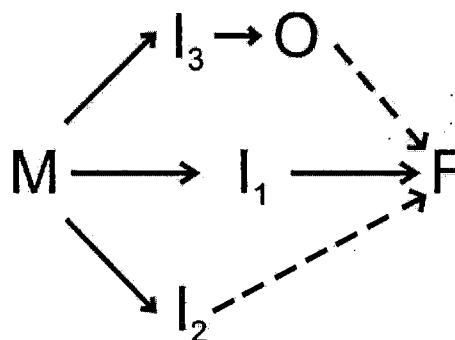


Figure 1.5 Hypothetical self-assembly pathway of A β . *In vitro* freshly dissolved A β mostly exists as an unfolded monomer (M). Class I compounds stabilize an A β intermediate conformation (I₁) that is assembly-competent and can aggregate directly into fibrils without previous association into oligomers. Class II compounds stabilize an A β intermediate conformation (I₂), that does not favor A β assembly into either oligomers or fibrils. Class III compounds stabilize an A β intermediate conformation (I₃) that supports A β oligomer formation but is incompetent for assembly into fibrils. Adapted from Ref [55].

Due to the dilemma of obtaining high resolution structures of intermediate states confronted by experimental techniques, the computational approaches have been employed to gain the insight into the aggregation mechanisms [57-62]. A mechanism for single β -strand to surmount unnatural registry without dissociation was proposed before experimental characterization, which later an *in silico* study confirmed and coined “reptation”. [57, 63]. In a study of self-assembly of A β , a simplified model which included only torsion angles and treated hydrogen bonds explicitly was used [64]. With this simplified model, Monte Carlo simulations were able to be performed on 20 copies of A β fragments. They observed early-stage aggregation events and obtained an atomic-detailed description of “nucleated conformational

Introduction

conversion” (NCC) [43] model for amyloid formation. The simulations which aimed at studying *ab initio* folding of peptides to form β -sheet oligomers usually started from unstructured peptides. And more simplified models will allow studying larger systems of peptides in a feasible time scale of computation. In principle, a feasible system for short peptides (4-10 residues) can be dozens even hundreds in coarse graining models, but for all-atomic models the computational power drops to less than 10 peptides in most cases. For either simplified or atomic models, usually a truncated segment rather than full length protein is used. The reason behind it is the hypothesis that mechanisms underlying aggregation of all amyloidogenic peptides are the same, which makes an amyloidogenic segment a perfect study subject in understanding peptide self-assembly.

Compared to coarse grained models, all-atom explicit solvent models can reproduce amyloid aggregation in aqueous environment more accurately and supply more information on side chain contacts [65]. Studies using atomic models usually started from a protofibril which are truncated from NMR or crystalline structures of mature fibrils. Free monomers were added to study how the monomers identify binding sites and how the fibril elongates. Because of the steric zipper motif in mature fibrils, side chain contacts become significantly important, which makes atomic models valuable. Two studies representing such application of atomic models were performed on segments of A β and Sup35 [66, 67]. The extensive simulations were able to probe the inter-peptide side chain contacts and large conformational fluctuations upon monomer addition to preformed β -sheet oligomers in a “dock-lock” mechanism. There were also a certain amount of computational studies which attempted to

Introduction

understand how residual mutations alter the distribution between native folded states and aggregation-prone states and therefore affect the aggregation rates [68, 69].

1.5. Nature of Amyloid Cytotoxicity

In most amyloidogenic diseases, there is typically cell loss associated with abnormal aggregation of locally expressed protein. In the case of insulin-resistant T2DM, to increase insulin yield, β cell reproduction could ameliorate the conditions, but the pathological β -cell loss due to high-rate β -cell apoptosis only aggravates the symptom. The interaction between membrane and amyloidogenic proteins has been long-time detected and studied. Since the first study published by Lorenzo *et al.* in 1994, several groups have observed dramatic cell morphological changes (such as blebbing, cell shrinkage, nuclear fragmentation etc.) typical of cell apoptosis and identified hIAPP amyloidogenesis as the inducer of β cell apoptosis [70-72].

Recently more and more studies on interactions between amyloidogenic peptides and cellular membranes challenged the early concept that fibrillar form was the toxic species [70]. As a result, it gave rise to a modified amyloid hypothesis [4]. Take hIAPP as an instance. According to the modified hypothesis, the toxic hIAPP functions intracellularly and more importantly, the toxic species is intermediate-sized non-fibrillar oligomers rather than fibrils [71]. There were clear observations that rapid loss of β cells precedes formation of extracellular islet amyloid [73] and preformed fibril solution does not induce cell apoptosis. More convincingly, nonfibrillogenic rIAPP is also capable of permeabilizing membranes under conditions that permit rIAPP membrane binding [74]. By applying an antibiotic rifampicin, hIAPP amyloid aggregation can be inhibited, but the formation of toxic oligomers can not be blocked [75]. Some researchers accordingly proposed that the

Introduction

toxic species is off-pathway of amyloid fibril formation, and any inhibitors of fibrillization could stabilize the toxic oligomers on the bypass and sustain the toxicity. These oligomers regardless of primary sequences displayed a common epitope that can be recognized by a conformational-specific antibody [53, 54]. The antibody ameliorates toxicity of several types of amyloid oligomers, indicating that the special conformation motif rather than sequence is related to their generic toxicity to membranes [76].

Membranes have been implicated in abnormal behaviors of hIAPP in two ways. First, lipid membranes have been shown to promote conformational conversion and aggregation behavior of hIAPP. Aggregation of hIAPP can be promoted by several types of lipid phases including free fatty acids or lipids [77-79], lipid micelles [80], and bilayers. Several types of free fatty acids have been studied, and most of them seemed to potentiate hIAPP aggregation when the concentration reached a critical value [78]. The mature fibrils were found to contain a portion of lipids which were suggested to be taken up from lipid membranes and wrapped into the fibrils while aggregation was going on [81-84]. As an indication, free lipid molecules tended to contact with certain exposed parts on hIAPP fibrils and probably helped maintain the rigid structure of amyloid fibrils near membranes [85]. Bilayer was the most utilized model and its composition appeared to be a critical factor that determined the extent to which membrane promoted hIAPP aggregation. Membranes that contain negatively charged lipids, such as phosphatidylglycerol (PG) or phosphatidylserine (PS) at physiological concentrations showed the strongest enhancement of hIAPP aggregation [86]. It was thought that electrostatic interactions between negatively

Introduction

charged lipids and positively charged (carried by K1, R11, and H18 at acidic pH) hIAPP play an important role in hIAPP accumulation and/or insertion.

The precise molecular mechanism by which membranes catalyze hIAPP aggregation is not yet fully elucidated. Nonetheless, transitions, i.e., random coil \rightarrow α \rightarrow β conformational changes, found in other amyloidogenic peptides have been observed when hIAPP was proximate to the membrane [74, 87]. In solution, hIAPP adopts a predominantly random coil structure with only small components of β -sheet/ β -turn and α -helical conformation [88]. When it approaches membrane, a clear transition to α -helical conformation shows up transiently and the α -helical structure probably acts as an intermediate conformation to β -sheet, since α -helical portion disappeared rapidly as β -sheet content increased [74, 86]. Only a small fraction of the peptide (mainly residues 8-18 [86]) participates in the helical structure and C-terminal that contains the core part of β -sheet (residues 20-29) remains unstructured. Of interest is the observation that rIAPP was able to form similar α -helical structure involving around 50% residues, but did not proceed to generate β -sheet secondary structure [74, 86]. This shed insight on distinct roles of N- and C-termini [89, 90]. Generally, N-terminus which has a higher propensity for α -helical structure [86] is responsible for membrane adsorption, probably insertion as well; while C-terminus which favors β -sheet conformation remains disordered at first and readily initiates aggregation process at high concentration on membrane surface. Besides, appealing observation on rIAPP suggested that its inability of amyloid aggregation may be due to the mutations of three proline substitutions located in C-terminus.

Introduction

The second respect of membrane-hIAPP interaction lies in the fact that membrane is the target for hIAPP toxicity, as discussed above. The leakage of membrane affects the membrane homeostasis and further disrupts the natural barriers of cell and/or organelles to the outside environment. Although most researchers agreed on the conclusions that prefibrillar forms were the toxic species and N-terminus insertion into membranes occurred commonly in most cases studied, the precise molecular mechanism of hIAPP-induced membrane damage remained a controversial question. And the most debatable part was whether the membrane damage involves peptide insertion only or the following fibril growth is even more crucial. Some studies that supported the former notion attributed hIAPP-induced membrane permeabilization to an “ion-channel” model [91-94]. The AFM (atomic force microscopy) images indicated that hIAPP amyloid channel was composed of five subunits [93] and these channels which showed poor ion selectivity were permeable for Na, K, Ca, and Cl ions [94]. A recent study in which hIAPP₁₋₁₉ fragments were utilized to disrupt membranes found that these truncated fragments insert into membranes stably without forming typical ion channels or further aggregating into fibrils. Therefore, the authors argued that N-terminus insertion is sufficient to cause membrane disruption which is a separate process from fibril formation. This agrees with the ability of rIAPP to cause membrane damage, noting that rIAPP is a non-amyloidogenic peptide but able to bind and insert into membranes [74]. Meanwhile, fibril-growth-dependent mechanism has been supported by a number of studies as well [84, 90, 95, 96]. Green *et al.* have observed the formation of small defects on lipid surface instead of well-defined ion channels and postulated nonspecifically generic perturbation of membranes in a “detergent-like” manner [96]. Likewise, Sparr *et al.* found lipids are extracted from membranes and taken up in the growing

Introduction

amyloid deposits [84]. Indeed, analysis of amyloid tissue from patients showed that *in vivo* formed amyloid fibrils contained up to 10% lipids [82]. More recently, Engel *et al.* studied the kinetic profile of hIAPP-induced membrane damage and matched it well with kinetic profile of hIAPP fibril growth [95]. Variables that affect hIAPP fibrillization also have the same effect on membrane damage. Thus, they proposed a hypothesis that growth of hIAPP fibrils at the membrane causes membrane damage. However, unlike the previous studies, Engel *et al.* attributed membrane leakage to a forced change in membrane curvature induced by fibril growth rather than lipid extraction.

1.6. Inhibitors of Aggregation and Toxicity

So far, we know the toxicity of amyloid is attributed to certain intermediate oligomeric states whose structures remain unclear. The amyloid aggregation process is believed to be complicated and most probably involves multiple parallel pathways. Despite the great progress of characterizing all the early-stage species made in recent years, our current knowledge of oligomer structures and related toxicity is still not adequate for rational drug design. Nonetheless, high-throughput searches for candidate drugs have led to the identification of several peptide/peptidomimetic and small molecule inhibitors. Extensive studies have been performed on their efficacy and inhibitory mechanism [52, 55, 97-102]. Peptide/peptidomimetic inhibitors largely involve short fragments truncated from full length amyloidogenic peptides, methylated variants of these peptides [98, 99], natural protein inhibitors [52, 103, 104], as well as some engineered binding protein, peptidomimetics and retro-inverso peptides [97, 105, 106]. These peptides or peptide-like inhibitors can be efficient in blocking the formation of amyloid fibrils *in vitro* and associated toxicity. But the

Introduction

high flexibility and propensity for proteolysis of peptide inhibitors impede their usage as drugs. A more promising option from a therapeutic perspective involves the use of small molecule inhibitors which are easily administrated and can be designed to be rigid to reduce entropy loss upon binding [101].

The most common anti-amyloid small molecule inhibitors belong to the family of polyphenol compounds and contain two common functional moieties: aromatic rings and polar groups on the rings [107]. Initially, the inhibitory effects of these compounds were attributed to their antioxidative activities. But more recently, it has been suggested that their inhibitory properties are tied to the structural similarities between the inhibitors and the aggregating peptides. Aromatic residues are commonly found in aggregating peptides and it has been suggested that the aromatic interactions between the inhibitor and the peptide play a key role in promoting inhibition. Novel inhibitor molecules were designed based on the unique scaffold obtained from these compounds [101, 107]. The resulting small molecule inhibitors can be very active even in the presence of membranes [102, 108].

Investigating the inhibition mechanism of anti-aggregation inhibitors is rendered challenging by the lack of information on the molecular level regarding the interactions between the inhibitors and the aggregates. Molecular dynamics simulations provide a unique tool to obtain high resolution pictures of peptide-inhibitor interactions. The structures of fibrils or truncated fibrils obtained from experiments can be taken as a starting point for simulations, and several small molecule or peptide inhibitors are then added to the system to search for binding sites on fibrils [109-115]. Some small molecule dyes that also have inhibitory properties such as ThT and Congo red molecules prefer to bind on the shallow grooves on

Introduction

amyloid β -sheet surfaces formed by hydrophobic side chains [110-112]. Some studies showed that small molecules block elongation at the fibril edges by binding to the same positions as the free peptides and consequently inhibiting elongation of fibrils via a “dock-lock” mechanism [113, 114]. A few other studies showed the importance of polar groups in destabilizing fibrils by disrupting inter-peptide backbone hydrogen bonds or side chain salt bridges that maintain the stability of fibrillar β -sheets [114, 115].

1.7. Research Objectives

On the basis of the abovementioned experimental observations, the self-assembly of hIAPP has been unquestionably associated with type II diabetes. Aggregation mechanism of not only hIAPP but also other amyloidogenic peptides/proteins has been well studied although molecular details remain insufficient. Manipulations of the aggregation process which involve interactions with other biomolecules (e.g. membranes, proteins, small molecules, etc.) and alternating environments (salt concentrations, pH, temperatures, etc.) also have made great progress in helping understand aggregation and cytotoxicity mechanisms. The research area regarding amyloid aggregation is multifaceted and challenging. The aim of the current research is, by applying *in silico* methodologies, to understand a few aspects in this area on an atomic detailed level: (1) what are the major driving factors and determinants in the early stage of aggregation and specifically how can the primary sequences affect the aggregation activities? (2) How do free lipid molecules (usually taken up from membranes while in proximity to growing amyloid fibrils) interact with/integrate into amyloid aggregates? (3) How does the unique *in vivo* environment of β -cells (to be specific - pH and co-existing insulin) solubilize hIAPP molecules? (4) What is the

Introduction

anti-aggregation mechanism of a small molecule inhibitor – resveratrol on blocking hIAPP aggregation in the early stage? In the hope of at least partially solving these issues, several simulations were performed and based on the obtained results these questions were attempted to be answered in this thesis report.

2. Computational Methodologies

2.1. Molecular Modeling and Molecular Dynamics Simulations

The emerging field of molecular modeling by computer has been attracting increasing interest by scientists from varied disciplines in recent years. Molecular modeling is a collective term to include both theoretical methods and computational techniques. As written in her book, Tamar Schlick described molecular modeling as *“the science and art of studying molecular structure and function through model building and computation”* [116]. The accuracy of the models and the computational power has become the two foundations of all techniques that belong to the realm of molecular modeling and simulation. Nowadays, the availability of high-speed, powerful computing platforms at reduced cost greatly extends the complexity of modeling systems, as well as the depth and width of its application area.

The fundamental approach of molecular modeling in computational biology or chemistry is the description of molecules as particles (atoms) obeying certain physical principles. The conformation, energy, and many other associated properties can be calculated by the solution of Schrödinger wave equation using quantum mechanical methods. However, in spite of the development of computer software and hardware, quantum calculation is solvable and practical for a few simple systems, which greatly limits its application. Thus, a number of alternative approaches with less accuracy emerged, such as semi-empirical or empirical methods, which have introduced different degrees of approximation to the Schrödinger equation. Among them, molecular mechanics also referred to as force field is widely used because of its simplified formulation of potential energy feasible in complex systems, and the

readily available search algorithms (e.g. energy minimization, sampling, and dynamic simulations). Unlike quantum mechanics, molecular mechanics must be evaluated empirically. As a result, the accuracy of the model completely relies on how potential energy functions and parameters fit to the theoretical and experimental data. Recently, various molecular models and force fields based on molecular mechanics have been developed and brought both multiple choices and challenges to scientists for selection while studying different levels of biological systems.

2.1.1. Mechanical Molecular Representation

The molecules are described at atomic level in molecular mechanics (MM). Electrons are treated implicitly in contrast to quantum mechanics (nuclei and electrons are explicitly calculated), thus masses and charges of the atoms are concentrated on the nuclei. The chemical bonds between atoms are described as harmonic springs, around which the molecule stretches, bends, and rotates to change the whole conformation. Physical properties of the mechanical molecule including inter and intramolecular interactions are calculated based on classical mechanics or Newtonian mechanics. The critical component of MM modeling involves the construction of potential energy (or force field), a function of atomic coordinates combined with a set of parameters empirically and theoretically derived. The effectiveness of a molecular model depends heavily on the accuracy of parameters. Different force fields are parameterized individually to reproduce consistently experimental data, which increases the difficulty to transfer potentials from one force field to another.

2.1.2. Potential Energy Function

For a molecular system of N atoms (possibly including atom groups, methyl groups modeled as united atoms in GROMOS force field, for example), potential energy E_p corresponding to one molecular geometry or conformation depends on Cartesian coordinates of all atoms only:

$$E_p = E_p(\mathbf{x}) = \sum_{i=1}^N f_i(x, y, z)$$

The force F_i exerted on atom i by all the other atoms in the system is given by the negative gradient of the potential energy E_p :

$$F_i = -\frac{\partial E_p(\mathbf{x})}{\partial \mathbf{x}}$$

In molecular dynamics simulation, the forces F_i is calculated every time step to generate new position and velocity for each atom.

The potential energy E_p is separable and typically constructed as the sum of several terms:

$$E = E_{bond} + E_{angle} + E_{tor} + E_{vdw} + E_{elec}$$

$$E_{bond} = \sum_{i,j \in S_{bond}} \frac{k_{bond}}{2} (l - l_0)^2$$

$$E_{angle} = \sum_{i,j,k \in S_{angle}} \frac{k_{angle}}{2} (\theta - \theta_0)^2$$

Computational Methodologies

$$E_{tor} = \sum_{i,j,k,l \in S_{tor}} \frac{V_n}{2} [1 + \cos(n\phi - \phi_0)]$$

$$E_{vdw} = \sum_{i,j \in S_{nb}} 4\epsilon_{ij} \left[\left(\frac{\sigma_{ij}}{r_{ij}} \right)^{12} - \left(\frac{\sigma_{ij}}{r_{ij}} \right)^6 \right]$$

$$E_{elec} = \sum_{i,j \in S_{nb}} \left(\frac{q_i q_j}{r_{ij}} \right)$$

The five terms listed here are primary and typical for all force fields, although the energy equations differ slightly. The first three terms (E_{bond} , E_{angel} , and E_{tor}) which represent potential energy of bond stretching, angle bending, and torsions of dihedral angels constitute the bonded interaction energy. The bonded interactions can be described by a harmonic potential, and l_0 , θ_0 , ϕ_0 are the equilibrium constants defined well in the force field. Thus, the bonded interaction energy reflects the fluctuation of the structure away from its equilibrium state. The forth (E_{vdw}) and fifth (E_{elec}) terms both calculate the interactions between nonbonded atom pairs which are separated by three bonds or more. The van der waals interaction E_{vdw} is described by Lennard Jones potential, which divides into repulsion at short interatomic separations and attraction at long distances. The van der waals interactions quickly decay and normally only atom pairs within a cutoff distance (usually 10Å) are calculated in simulation. In contrast, electrostatic interaction is hard to deal with and also computationally expensive. The simple coulombic potential between pairs of charged nuclei described here is not a suitable approximation method [117]. The charge distribution about each nucleus is obviously much more complex than point charge. An accurate electrostatic potential representation is especially critical for highly

charged system (e.g. nucleic acid) and the notion of modeling electronic polarizability is now a current focus in force field design.

2.1.3. Molecular Dynamics Simulation

Since the first MD simulation of protein (BPTI, bovine pancreatic trypsin inhibitor) was published in 1977 [118], biomolecules (proteins and nucleic acids) have been considered as dynamic systems whose internal motions are critical for their functions [119]. The potential energy functions provide the foundations of MD simulation. A biomolecular model is treated as mechanical-body system, and the description of atom motions also applies classical mechanics – the well-known Newton's equation of motion.

When running a MD simulation, we need to assign initial positions (by offering starting structure) and velocities (scaled according to simulation temperature) for all atoms. The new positions and velocities after a short time step (usually 1-10fs) are updated accordingly by solving Newton's equation of motion.

$$\begin{aligned} \vec{F}_i &= -\frac{\partial E_p(\vec{x})}{\partial \vec{x}} \\ m_i \frac{d^2 \vec{x}_i(t)}{dt^2} &= \vec{F}_i \\ \frac{d\vec{v}_i(t)}{dt} &= \frac{\vec{F}_i(t)}{m_i} \end{aligned}$$

Each time step forms a loop. At the end of each loop, potential energy and forces are calculated. New positions and velocities are updated for the following loop. Thus,

Computational Methodologies

MD is a repetitive process and also deterministic (the future state is predictable and completely determined by present). Normally, coordinates of atoms are output for visualization and stored as a *frame* after every hundreds of time steps (1ps, for example). A series of frames sequentially along the simulation time is output as a *trajectory*. There is always a dilemma that experimental observables are averaged over an ensemble (a collection of all possible microstates at an identical macroscopic or thermodynamic state), while results from MD simulation are time averages. Resolving the problem leads to *Ergodic hypothesis*, which states time average can be equal to ensemble average with the circumstance that all accessible microstates in phase space have passed by over a long period of time. In this sense, MD simulation is basically a sampling process seeking to search all possible conformations of the target system. However, within the current simulation time ($\sim 100\text{ns}$ - $1\mu\text{s}$), the states that MD can sample in conformational space are finite, especially rare for high-energy states. Furthermore, when MD simulation is performed under room or physiological temperature (as it is normally done), it is extremely difficult to surmount high energy barriers ($>\sim 10\text{kJ/mol}$) and to jump over from one local minimum to another or even to the global minimum (Figure 2.1). Therefore, to overcome this quasi-ergodicity problem suffered by MD, enhanced sampling methods, such as REMD (replica exchange molecular dynamics) are developed to sample wider space by taking a “random walk” in potential energy space.

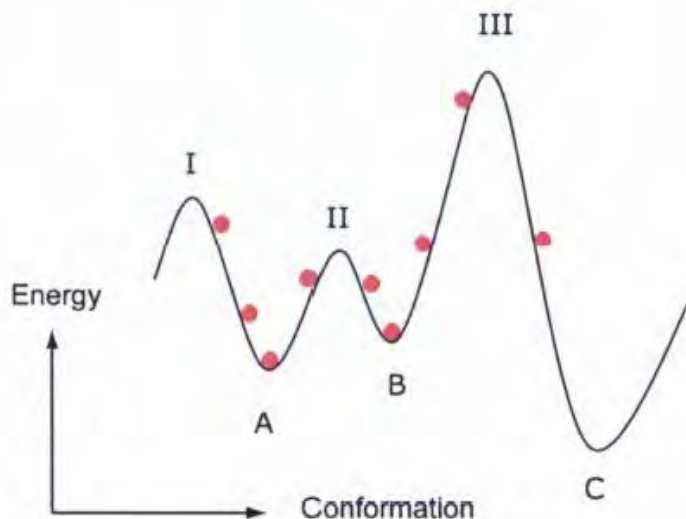


Figure 2.1 Schematic diagram of conformational sampling on the potential energy surface by MD simulation. The solid curve shows the one-dimensional energy surface, and red balls represent different conformations on the energy surface. At low temperature, MD simulation starting from minimum A is able to overcome lower energy barrier II and sample in minimum B, but difficult to overcome barrier III which separate minima B and C. Thus, simulation seldom samples conformations in global minimum C compared with the other two local minima A and B.

2.1.4. Replica Exchange Molecular Dynamics Simulation

In REMD simulation, a number of independent copies (or replicas) at different temperatures are simulated simultaneously by conventional MD method. Every few time steps, pairs of neighboring replicas i and j are attempted to exchange their thermodynamic states T_i and T_j (temperatures) with Metropolis criterion.

$$P_{accept} = \min \left[1, \exp \left[-\frac{1}{k_B} \left(\frac{1}{T_j} - \frac{1}{T_i} \right) (E_i - E_j) \right] \right]$$

Computational Methodologies

Here, k_B is the Boltzmann constant; T_i and T_j are the temperatures of replica i and j ; E_i and E_j represent the potential energy in replicas i and j . Thus, the weight factor is just the product of Boltzmann factor and constants of states, which are essentially known. The acceptance probability P_{accept} is calculated every trial and compared with a randomly generated number ε ($\varepsilon \in [0,1]$). According to the criterion, a state with a lower potential energy at high temperature is definitely accepted by the replica at low temperature ($E_i > E_j$, when $T_i < T_j$). Meanwhile, high-energy states at high temperatures ($E_i < E_j$, when $T_i < T_j$) still have a non-zero probability to come to the lower-temperature replicas (if the exponential term is larger than ε). Therefore, even if one replica is temporarily trapped in a local minimum, the simulation can escape via an exchange with a higher-temperature configuration.

Despite the limitations of REMD (a great many replicas needed for large systems, the speed bottleneck by frequent communication between processors, and information loss in kinetics, etc. [120]), it is considered as a very powerful sampling method and universally utilized. Several biomolecular simulations have investigated the efficiency of REMD relative to conventional, constant temperature MD simulation [121-124]. And for some systems, there are indications that REMD simulation may be an order of magnitude more efficient than conventional MD in sampling wider space or equilibrating within less simulation time [125]. Until now the method is still under development on how to make different parameter choices [126], how to choose the maximum temperature [127], how frequent to try the exchanges [128], and so forth. In our studies, we utilized GROMACS package [129] to perform REMD, and the method was proved to be an efficient tool for our systems.

2.2. Define Secondary Structure of Proteins

The DSSP algorithm written by Wolfgang Kabsch and Christian Sander is a standard method to extract secondary structure and geometrical features of proteins from atomic coordinates [130]. The algorithm is mainly based on identification of hydrogen-bonding patterns. Hydrogen bond is the basic and common element for all secondary structures and different hydrogen bonding patterns discriminate different types of secondary structures. Hydrogen bond is examined by calculating the electrostatic interaction energy between two hydrogen bonding groups as followed,

$$E = q_1 q_2 \left(\frac{1}{r(ON)} + \frac{1}{r(CH)} - \frac{1}{r(OH)} - \frac{1}{r(CN)} \right) * 332 \text{ kcal/mol}$$

where $q_1 = 0.42e$ and $q_2 = 0.20e$, and $r(AB)$, the interatomic distance from A to B. This is based on assignment of partial charges of $-0.42e$ and $+0.20e$ to the carbonyl oxygen and amide hydrogen, and the opposite charges to the carbonyl carbon and amide nitrogen, respectively. A good hydrogen bond has about -3 kcal/mol binding energy. Here, a generous cutoff is chosen (hydrogen bond is recognized if $E < -0.5 \text{ kcal/mol}$) and well tested to allow for an (N)H-O distance up to 2.2\AA .

Depending on the patterns of hydrogen bonds, DSSP recognizes mainly seven types of secondary structures which are summarized here.

"H"	= 4-helix (α -helix)
"G"	= 3-helix (3_{10} -helix)
"T"	= 5-helix (π -helix)
"B"	= isolated β -bridge
"E"	= extended strand, participates in β -ladder
"T"	= hydrogen bonded turn
"S"	= bend

Each residue is assigned a single letter to define its secondary structure in the output file of DSSP program. In our aggregation simulations, β structures (β -bridge, β -ladder, and β -sheet) are the dominant secondary structures, thus we only focus on the definition of these structures and the other structures are well defined and described in details in Ref [130].

β -bridge is the basic unit of β -ladder and β -sheet. Either a parallel or antiparallel β -bridge forms between residues i and j , if there are two hydrogen bonds between two nonoverlapping stretches of three residues each, $i-1, i, i+1$ and $j-1, j, j+1$. Then a β -ladder can be defined accordingly as a set of consecutive bridges of identical type (parallel or antiparallel). β -sheet is a set of one or more ladders connected by shared residues. In output file, a lone β -bridge is symbolized by “B”, whereas longer sets of β -bridges of the same type are symbolized by “E” for extended β -strand. β -sheets with β -bridges are likewise assigned as “E”.

2.3. Dihedral Angle Principal Component Analysis

Analyzing free energy landscape of large biomolecules simulated by either MD or REMD methods has promoted much progress in understanding kinetics of protein folding and aggregation. Since it is impractical to involve the total number of degrees of freedom ($3N-6$ coordinates) in the system, a principal component analysis (PCA) method has been introduced, in which a dominant part of the system's fluctuations can be described in terms of only a few PCA eigenvectors. However, before application of PCA method, the overall translation and rotation of a molecule need to be eliminated from the internal motion, which is somehow impossible, especially for flexible molecules. We have adopted a modified version, referred to as dPCA [131],

in which only dihedral angles of peptide backbone are considered and other internal fluctuations such as bond lengths and bond angles and overall motions are efficiently removed because they contribute little to the folding of the peptide. The dPCA method is appealing for our system in that peptide aggregation into β -sheet conformation, to a large extent, involves changes in backbone dihedral angles and hydrogen bond formation between backbone carbonyl oxygen and amide hydrogen. We find that most of structures extracted from a single local minimum on the free energy surface constructed by dPCA method are classified into one group by pair-wise structural clustering method. On the other hand the pair-wise clustering method cannot be directly exploited to construct free energy landscape. Thus the accuracy and efficiency of dPCA method is verified.

2.4. Binding Energy Calculation

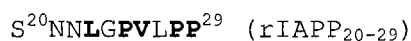
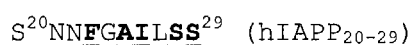
The binding energy of ligand-target complex can be estimated by equation:

$$\Delta E_{bind} = E_{complex} - E_{target} - E_{ligand}$$

$E_{complex}$, E_{target} , and E_{ligand} are the total potential energy of ligand-target complex, target-only and ligand-only, respectively, all of which can be decomposed into two terms: intra-molecule potential energy calculated by Gromacs package and solvation energy estimated by using Generalized Born surface area (GBSA) model in the sander module of AMBER package [132, 133]. The source code of the amber leap program was modified to import nonbonded parameters from OPLS-AA force field.

3. Sequence Variation of IAPP₂₀₋₂₉ Affects Peptide Aggregation

As a peptide hormone, IAPP widely exist in a variety of mammalian species, among which the variant of rodent species does not aggregate into amyloid fibrils and is not cytotoxic. There are six mutation positions on the full length rIAPP, five of which locate in a hydrophobic core from residue 20 to 29. The sequences of IAPP₂₀₋₂₉ in human and rodent species are listed herein.



Five residues of total six disparate between the two sequences are underlined. The sixth mutation is H18 substituted by R18 in the sequence of rIAPP. Within the decapeptide, three proline substitutions are particularly of interest because of the well known role of proline in breaking secondary structure elements including α -helix and β -sheet. The segment of hIAPP has a high tendency to aggregate into amyloid fibrils with a similar morphology to the fibrils derived from full-length peptide. It was assumed to form the hydrophobic core in full-length fibrils according to some structural models; while in the other models, it forms a turn which probably initiates the amyloid folding. Due to the importance of the two versions of the segment in either initiating or abolishing aggregation, we studied this decapeptide from both human and rodent species. By comparing the distinct aggregation behaviors of two decapeptides, REMD simulation was found to be robust to study peptide self-assembly system. Critical residues which are negatively tolerant to mutation were

disclosed. Several structural features and aggregation behavior of hIAPP₂₀₋₂₉ in the early stage was also discovered.

3.1. Simulation Setup

One REMD simulation was performed on four copies of hIAPP₂₀₋₂₉. Four copies of rIAPP₂₀₋₂₉ were subjected to the same simulation scheme as a negative control of peptide aggregation. For abbreviation, the two systems are referred to as hIAPP and rIAPP respectively within the scope of chapter 3 and 4. The peptides capped by groups in N and C termini were initially constructed in a fully extended conformation and separated by at least 2 nm from each other to avoid close contacts (Figure 3.1). In each system, the four identical peptides were arranged in parallel or mixed parallel/antiparallel patterns to allow for all four possible arrangements: (i) N-termini of all four peptides were placed upwards; (ii) N-termini of three out of four peptides were placed upwards; (iii) N-termini of two peptides on one side were placed upwards, and (iv) N-termini of two peptides on the diagonal directions were placed upwards. The four structures in different arrangements were alternately used as the starting structures of 36 replicas to avoid bias in favor of parallel or antiparallel β -sheet alignments during REMD simulations. The peptides were solvated in a 4*4*4nm cubic box keeping a minimum distance of 1 nm between the solute and each side of the box. The peptides were immersed in explicit simple point charge (SPC) water molecules [134]. The final setup of the systems contained 1833 water molecules for rIAPP system and 1841 water molecules for hIAPP. All systems were neutral and no extra counterions were added.

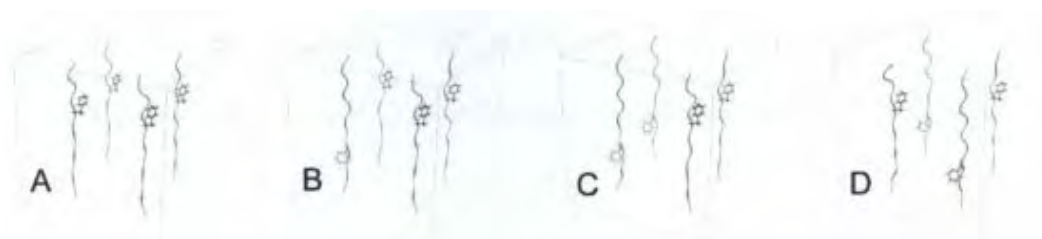
Sequence Variation of IAPP₂₀₋₂₉

Figure 3.1 Initial arrangements of four identical hIAPP₂₀₋₂₉ peptides. Backbones of peptides are shown in cartoon. Side chains of F23 are explicitly represented in sticks for readily identification of N-termini. A. N-termini of all four peptides point upwards; B. N-termini of three out of four peptides point upwards; C. N-termini of two peptides on one side point upwards; D. N-termini of two peptides on the diagonal point upwards. The four starting states allow for all possible parallel and antiparallel arrangements. System of rIAPP was set up in the same way.

The GROMACS program suite [135] and OPLS-AA force field [136, 137] were used. All bonds involving hydrogen atoms were constrained in length according to LINCS protocol [138]. Electrostatic interactions were treated with Particle Mesh Ewald method [139] with a cutoff of 0.9 nm, and a cutoff of 1.4 nm was used in the calculation of van der waals interactions. The integration time step of simulation was set to 0.002 ps. The protein and the water groups were separately coupled to an external heat bath with a relaxation time of 0.1 ps. Non-bonded pair lists were updated every 5 integration steps (0.01 ps). After 500 steps of steepest-descent minimization, 100 ns REMD simulations continued. The temperatures of the 36 replicas used in the REMD simulations are listed herein: 315.0K, 318.9K, 322.9K, 327K, 331.2K, 335.4K, 339.7K, 344.1K, 348.6K, 353.2K, 357.9K, 362.6K, 367.5K, 372.5K, 377.5K, 382.7K, 388.0K, 393.4K, 398.9K, 404.6K, 410.4K, 416.3K, 422.3K, 428.5K, 434.9K, 441.4K, 448.1K, 454.9K, 461.9K, 469.1K, 476.5K, 484.1K, 491.9K, 499.9K, 508.2K, and 516.7K. Exchanges between neighboring replicas were tried every 1000 steps (2 ps). The proper temperature intervals were selected to result in approximately 30% exchange rate for each replica. The conformation coordinates

were output every 500 steps (1 ps). After 100 ns REMD simulation, each system generated an ensemble of 100,000 structures at each temperature and total 3,600,000 structures at all temperatures.

3.2. Divergent Aggregates derived from hIAPP₂₀₋₂₉ and rIAPP₂₀₋₂₉ Tetramers

It has been well demonstrated that full-length (37-aa) rIAPP and truncated rIAPP₂₀₋₂₉ segment do not form amyloid fibrils *in vivo* or *in vitro* [30, 140, 141]. Content of β -structure in the tetrameric aggregate was assessed by the percentage of residues that adopt β -sheet conformation and its evolution is shown in Figure 3.2. Consistent with experimental studies, aggregates derived from rIAPP₂₀₋₂₉ seldom exhibit β -structures, as indicated by ~3% β -content all over the simulation. Meanwhile, ~20% residues in hIAPP adopt in β -sheet structures from 40ns to the end of simulations. The convergence of the simulations is also certificated by the steady level of β -contents for the last half of both simulations.

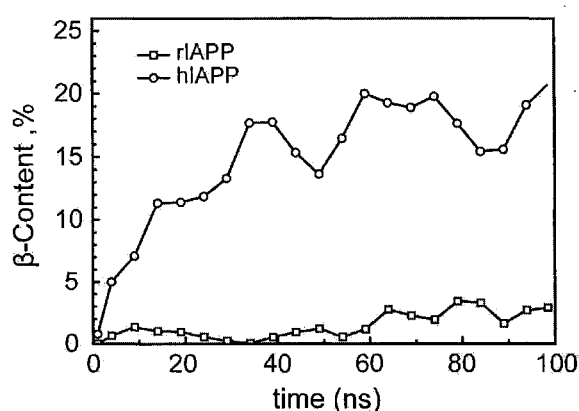


Figure 3.2 Time evolution of percentage of residues in β -sheet structure. The data was extracted from trajectories at 315K and averaged per 5 ns.

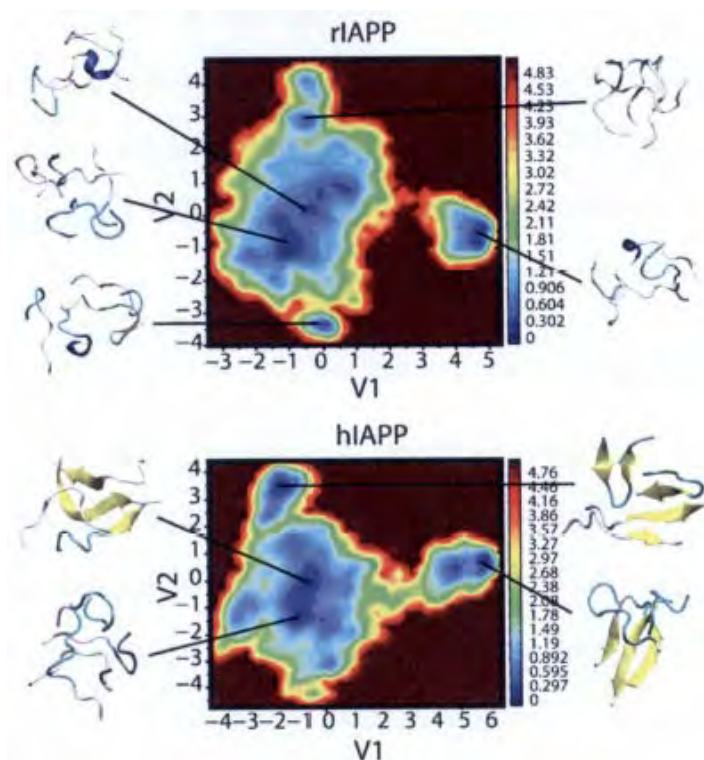


Figure 3.3 dPCA free energy landscapes and representative structures. The structures represent all the conformations that fall in the corresponding local minimum. The secondary structures, i.e. β -sheet (yellow), helix (blue), coil (white), and bend (cyan) were identified and colored by VMD [142]. The data was extracted from trajectories at 315K after the first 50 ns equilibrium. Energy bars are shown on the right. The unit of energy is kJ/mol.

On the dPCA free energy landscapes, several dominant minima are separated by small free energy barriers (Figure 3.3). The corresponding representative structures were obtained by RMSD clustering. The aggregates of rIAPP are compact. Coils and turns are the predominant structural motifs together with a small portion of helices. Without long extended β -structure, single strands twist to form coils. The overall structure of rIAPP aggregate is less structured. In contrast, hIAPP aggregates are consisted of ordered β -sheet dimers or trimers together with coiled monomers. The mixture of ordered and amorphous structures illustrates the dynamical equilibrium between the two states. Both parallel and antiparallel hydrogen bonding patterns are

Sequence Variation of IAPP₂₀₋₂₉

observed in the hIAPP β -sheet oligomers. Combined the results of β -content evolution and dPCA, it is clear that after 100 ns simulation, while rIAPP₂₀₋₂₉ aggregates remain disordered, hIAPP oligomers are on divergent ways to form amyloid nuclei in the form of β -sheet dimer, trimer, or even tetramer.

3.3. Orientation and Alignment Patterns of β -Sheet Oligomers

By using both FTIR (Fourier transform infrared spectroscopic) [143] and ssNMR (solid-state NMR) [144-146] techniques, it has been found that Unlike full-length hIAPP, truncated segment hIAPP₂₀₋₂₉ form amyloid fibrils which contain both antiparallel and parallel β -sheets. In the structures representing local minima (Figure 3.3), a mixture of parallel and antiparallel β -sheets were observed. When the two opposite orientation patterns were monitored along simulation at 315K, it was found that they have different occurrences (Figure 3.4). At first antiparallel β -bridges (ap- N_B) and parallel β -bridges (p- N_B) increase at different rates and eventually ap- N_B is two times more favored than that of the parallel orientation. The p- N_B of hIAPP is at the same level as rIAPP, indicating an overwhelming prevalence of ap- N_B .

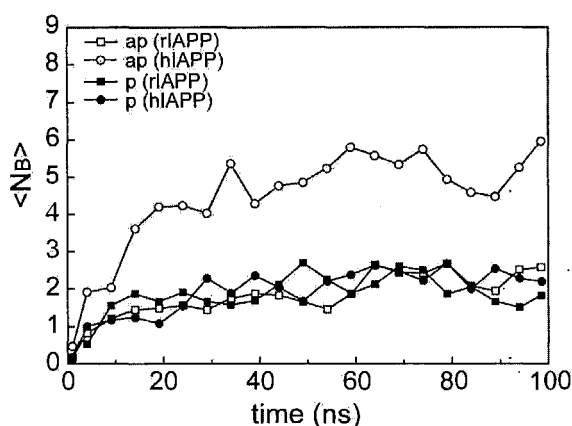


Figure 3.4 Time evolution of average number of antiparallel and parallel β -bridges. The data was extracted from trajectories at 315K and averaged per 5 ns.

Sequence Variation of IAPP₂₀₋₂₉

The same orientation preference of the hIAPP decapeptide was demonstrated in β -bridge contact maps showing the occurrences of pairs of interstrand residues linked by β -bridges (Figure 3.5). In principle, contact numbers from left panels (B1, ap- β -bridges) are overwhelmingly greater than those from right panels (B2, p- β -bridges) indicating antiparallel β -sheets are of higher probability than parallel β -sheets. A similar observation was reported in a Monte Carlo simulation: for the lower-level aggregates, antiparallel β -sheets are dominant [65].

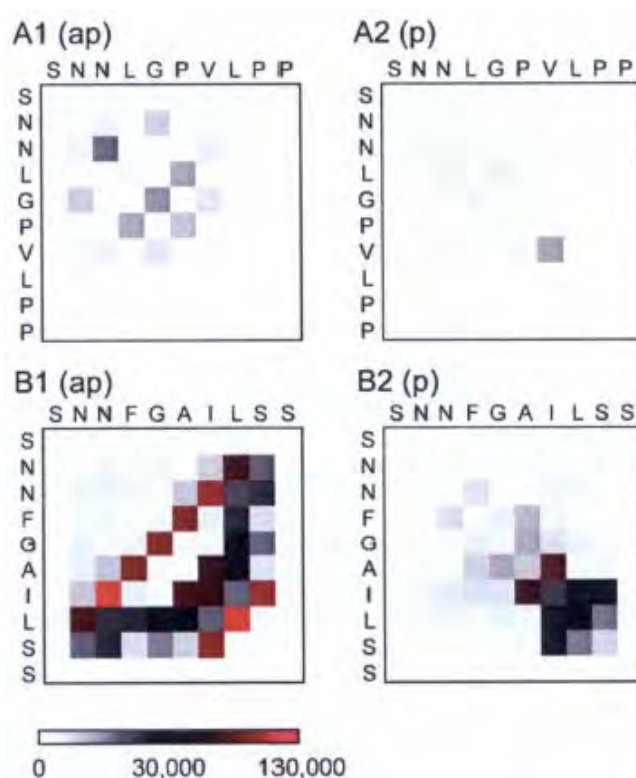


Figure 3.5 β -bridge contact maps. One contact is defined when a pair of interstrand residues is linked by β -bridges. Figures A1-2 show the contact maps of rIAPP and B1-2 show the contact maps of hIAPP. Left and right panels separate antiparallel and parallel β -bridges. In-register patterns are those on the antidiagonals for ap- β -sheets and diagonals for p- β -sheets. Out-of-register patterns are those off-diagonals /off-antidiagonals.

Furthermore, the registry patterns of interacting β -strands are also demonstrated in contact maps. Both parallel and antiparallel β -sheets exhibit a mixture of in-register and out-of-register patterns. In principle, in-register patterns are able to extend β -sheet to a longer length and to maximize the formation of hydrogen bonds. Although the perfect in-register patterns are not the dominant patterns, the occurrences of those near-in-register patterns are higher and the β -sheet region is prolonged to involve maximally seven pairs of residues. In the sequence of hIAPP₂₀₋₂₉, the C-terminal region contributes more in the β -bridge formation and tends to form more β -bridges. The reason behind it is probably the same as folding mechanism. The burial of hydrophobic residues such as A25, I26, and L27 in this sequence initiates the early collapse of peptides, followed by conversion into β -sheets within the hydrophobic core.

3.4. Critical Residues of hIAPP₂₀₋₂₉ to β -Sheet Formation

From the β -bridge contact maps, the probability of C-terminus of hIAPP₂₀₋₂₉ to form β -structures is much higher than N-terminus. To further investigate the role of each residue in aggregation, secondary structure propensity (SSP) of the ten residues were accessed (Figure 3.6). It is obvious that three hydrophobic residues A25, I26, and L27 in hIAPP₂₀₋₂₉ show high propensities for β -structures. The hydrophobic region (residues 25-27) is considered to be the core part of β -sheets for fragment hIAPP₂₀₋₂₉ by experiments [143, 144]. Residues N22, F23, and G24 show high propensities for bend/turn. This may be due to G24 with a high backbone flexibility and F23 being likely to be present at turn/bend structures. The terminal residues (S20, N21, and S29) are generally unstructured, as their preferences for any of the three sorts of secondary

Sequence Variation of IAPP₂₀₋₂₉

structures are very low. The overall sequence of hIAPP₂₀₋₂₉ shows a rather low propensity for helical structures.

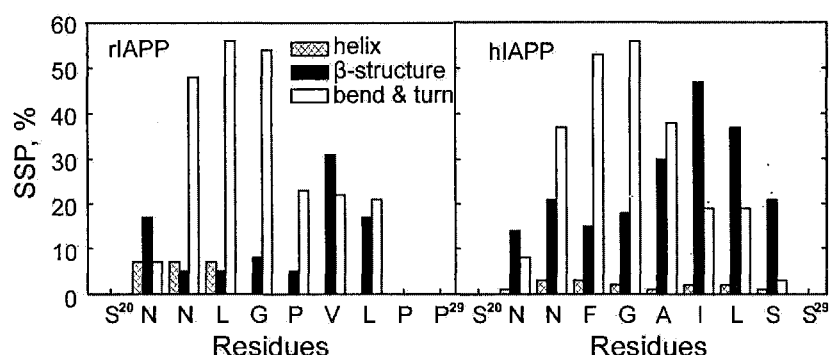


Figure 3.6 Secondary structure propensities of residues. Secondary structure element helix includes all three kinds of helical structures (α -helix, 3-helix, and π -helix). Element β -structure includes both β -sheets and isolated β -bridges. Definition and identification of different types of secondary structures were described in chapter 2 for Methodology and ref[130]

Compared to hIAPP, rIAPP shows a similar propensity for bend/turn in residues 22-24, but the probability of adopting β -structures in the whole sequence is greatly decreased with only V27 and L28 remaining a relatively high level. It has been shown that single mutation I27V only slightly reduces the aggregation ability of hIAPP₂₀₋₂₉, which is probably due to the hydrophobicity of valine and a similar propensity for β -structures to isoleucine [30].

3.5. Origins of Disrupting Effect of Proline Residues

The cyclic structure of proline's side chain locks its backbone dihedral angle, ϕ , at a narrow range between -90° to -60° , which thereby brings an extra conformational rigidity to the proximal region on the protein sequence. Proline is a well know

structural disruptor of either of the secondary structure elements. Similarly, in our simulations, proline dihedral angle ϕ is found to be restrained in a narrow range which cannot accommodate β -sheet structure (Figure 3.7A). As a rule, the ϕ angle for a β -sheet structure is between -120° to -140° . The distributions of ϕ dihedral angle of the three proline residues (P25, P28, and P29) on rIAPP as well as their counterpart residues on hIAPP show clear differences. The counterpart residues on hIAPP₂₀₋₂₉ all have a considerable probability for ϕ angle to locate in the β -sheet range. However, distributions of ϕ angles of three proline residues show no overlapping region (-90° to -60°) with β -sheet structure. Thus backbone structure around proline would induce considerably unfavorable high energy if it adopted a β -sheet conformation.

Figure 3.7B presents a snapshot of the region on the C-termini of two rIAPP strands from the simulation. The two rIAPP strands are in a perfect in-register alignment with only one parallel β -bridge (two hydrogen bonds) between two Val26 amino acids. This alignment pattern makes a large contribution to rIAPP parallel β -sheet alignments (Figure 3.5 A2). The snapshot offers hints about influence of two proline residues (P25, P28) on the interstrand hydrogen bonding network. As illustrated in the sketch plot (Figure 3.7C), two V26 residues form interstrand hydrogen bonds but the extended hydrogen bond ladder is disrupted by the missing hydrogen atoms on proline amide groups.

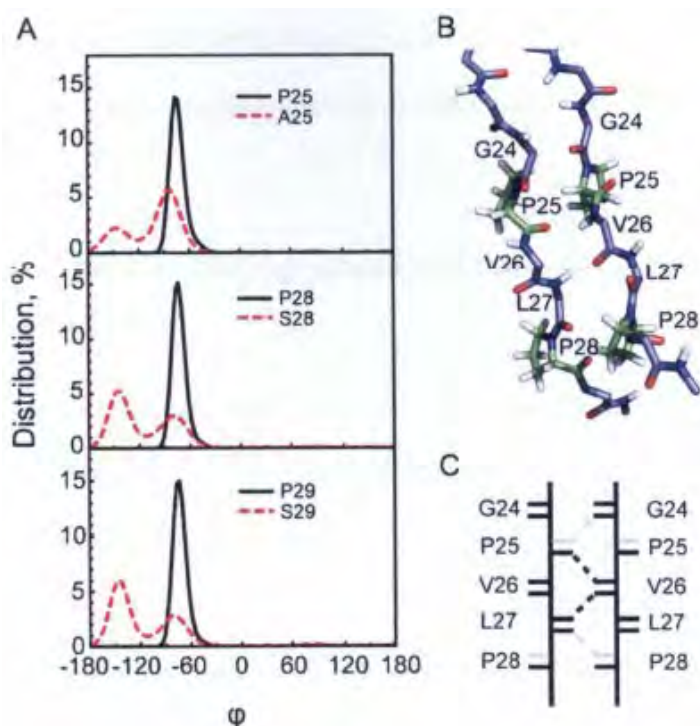
Sequence Variation of IAPP₂₀₋₂₉

Figure 3.7 Exceptional distributions of ϕ dihedral angles of three proline residues on rIAPP disrupt the continuity of hydrogen bonding network. A. Distribution of dihedral angle ϕ of three proline residues on rIAPP (black solid curves) as well as their counterpart residues on hIAPP (red dashed curves). B. A snapshot showing backbone hydrogen bonds on C-terminal region of two strands of rIAPP. Main chains of residues are shown in sticks by PyMOL package. Side chains of four proline residues (two P25, and two P28) are explicitly shown in green. Hydrogen bonds between V26 and two interstrand residues P25, L27 are presented as grey dash lines. C. An illustrative figure gives a simple demonstration of hydrogen bonding network of the structure in B. The real hydrogen bonds in structure B are shown in black dash lines; the grey dash lines show the missing hydrogen bonds which are supposed to form between proline residues and their partner residues.

The occurrence of β -bridges between V26 reaches a large number of over 10000 counts compared to the near-zero contacts of other residue pairs (Figure 3.5 A2). Finally, the total contact numbers around proline in either parallel or antiparallel patterns are at a comparatively low level, indicating that proline disrupts hydrogen bonding nearby in almost all alignment patterns. Both the β -bridge contact maps of rIAPP and the snapshot of parallel, in-register rIAPP dimer describe the same story

that the failure of proline to be in β -conformation and to act as hydrogen bond donor prevents extension of β -bridges and therefore avoids formation of stable β -sheets.

3.6. Conformational Reorganization of Pre-nucleus Oligomers in Two Pathways

In Figure 3.2, it is clear that hIAPP tetramers take ~ 50 ns to reach a relatively stable level ($\sim 20\%$) of β -content. But the decrease of radius of gyration (R_g) is much faster than the increase of length of β -sheet regions. Within 10 ns, $C\alpha$ - R_g of hIAPP rapidly drops from initially ~ 1.6 nm to ~ 1.1 nm (Figure 3.8). The contact number of $C\alpha$ atoms explodes simultaneously with the drop of R_g . Meanwhile, only 7% hIAPP residues are transformed into β -structures (Figure 3.2). In the following 45 ns (from 5 ns to 50 ns), R_g remains around 1.0 nm, while β -content increases from 7% to 20%. These early stage (5-50 ns) intermediate species are condensed (small R_g) but less structured (low percentage of β -structures), which could be the amorphous aggregates as described in other's simulations [64, 147, 148] as well as experiments [43, 63]. The rapid collapse of initially dispersed strands is followed by a slow structural reorganization to allow amorphous species to transform into a β -sheet oligomer which can act as a nucleus when it reaches to a critical size.

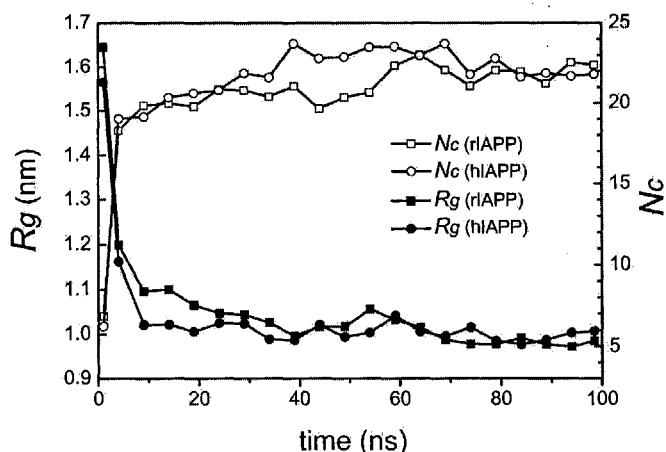
Sequence Variation of IAPP₂₀₋₂₉

Figure 3.8 Time evolution of radius of gyration and total number of atomic contacts. Only C α atoms of backbones are taken into consideration while calculating radius of gyration (Rg) and contact number (Nc). The value was averaged over every 5 ns at 315K.

The nucleation process of four hIAPP₂₀₋₂₉ peptides involves complex structural transition from initial amorphous aggregates to partially ordered β -sheets. The essential part of structural transition is the elongation of hydrogen bonds formed on backbones. Thus the number of extended β -bridges (N_B) should be a suitable reaction coordinate for describing the conversion process. On the other hand, the order level of a tetrameric aggregate can also be described by how many peptides are involved in forming β -sheet oligomers, namely to form β -sheet dimer, double dimers, trimer and tetramer. The evolution of different β -sheet oligomerization states as a function of N_B is elaborated based on the ensemble trajectories at 315K (Figure 3.9). Besides, following a replica trajectory that contains information of a continuous structural evolution, the transition from an amorphous state to an ordered state can be vividly demonstrated (Figure 3.10 and 3.11).

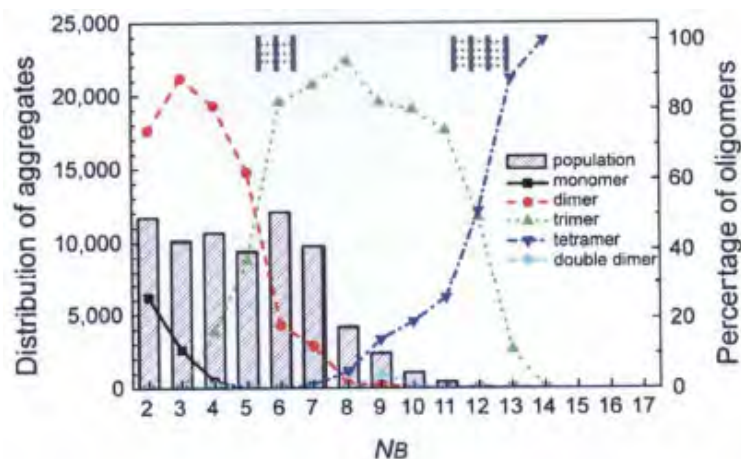
Sequence Variation of IAPP₂₀₋₂₉

Figure 3.9 Distribution of tetrameric aggregates on different N_B and increasing size of β -sheet oligomers with the increase of N_B . The population of aggregates forming certain value of N_B is shown in bar. Percentage of β -sheet oligomers (β -sheet dimer, trimer, tetramer, and double dimers) is represented by lines and symbols.

The population of aggregates with N_B value in the range of 2 to 7 is large (Figure 3.9). Those ordered aggregates with larger N_B (more than 7) are largely β -sheet trimers or tetramers but have relatively small population. The dominant β -sheet oligomer changes gradually with the increase of N_B : unstructured \rightarrow dimer \rightarrow trimer \rightarrow tetramer. The increasing size of the dominant oligomer indicates the transformation from amorphous aggregates to a more ordered state in a manner of monomer addition. The aggregates which have two individual dimers are less populated.

It is surprising to discover that when N_B is small ($N_B = 6$), the percentage of trimer is larger than that of dimer. Similarly, the percentage of tetramer is larger than that of trimer at $N_B = 12$. For a clear description, at the transition point (where the size of the dominant oligomer increases by 1), two illustrative sketches for trimeric and tetrameric β -sheets are drawn, with short dashed lines denoting β -bridges. Only three out of the ten residues in each strand forming hydrogen bonds are competent to stabilize a tetrameric β -sheet. This indicates that the β -sheet nucleation site is not

necessary to have a long and perfect in-register pattern; a short β -sheet region is capable of being a template to invite free monomers to join the nucleus. The “template” hypothesis was inspired and supported by the work of Kameda and Takada [149], as the hydrogen bond donors and acceptors on the template are in perfect positions for forming hydrogen bonds with free peptides.

The aggregation of oligomers is a transition process from amorphous states to ordered β -sheets. Among all folded trajectories, some of the aggregation pathways are simple and straightforward, in which the growth of the β -sheet oligomer is simply through monomer addition and sheet extension accomplished by forming more hydrogen bonds. Other trajectories show much more complicated pathways, particularly involving parallel-to-antiparallel transition. We have examined several folded replica trajectories of hIAPP aggregation, in two of which the key intermediate states are shown in Figures 3.10 and 3.11 to show parallel-to-antiparallel transition in distinct manners. As aforementioned, the short peptides prefer to form antiparallel β -sheets over parallel ones. There is a high chance for a parallel-to-antiparallel transition to occur. Such type of reorganization takes place mainly through two paths: global conformational change involving detachment and reattachment of the aggregates (Figure 3.10) and local rotation of single strand without detachment (Figure 3.11). The second path is essential to large aggregates where detachment of peptides in the core of aggregates is impossible and only reptation of peptides is possible.

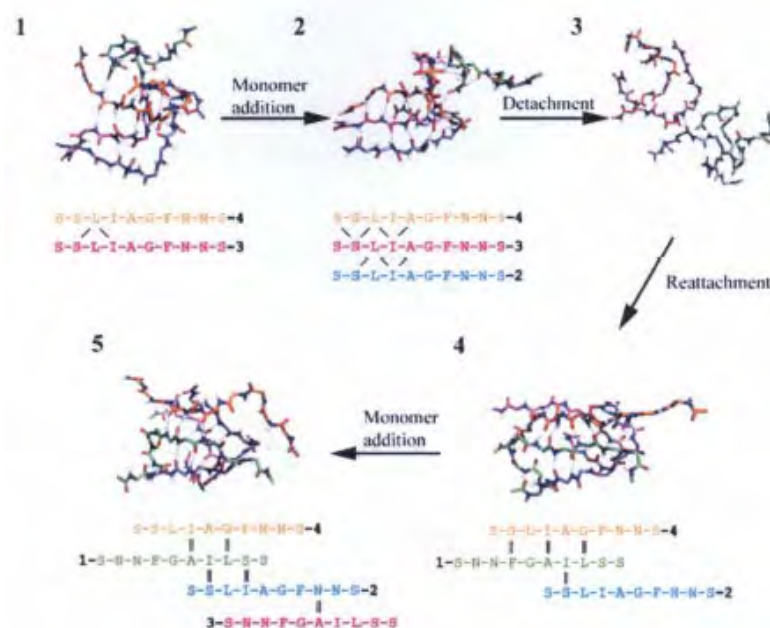
Sequence Variation of IAPP₂₀₋₂₉

Figure 3.10 Parallel-to-antiparallel transition path 1. Transition pathway of one replica trajectory is illustrated. Only main chain atoms of peptides are shown in sticks. Dashed blue lines indicate hydrogen bonds. Four strands are distinguished by different colors (strand 1, 2, 3 and 4 is in green, blue, magenta and orange color, respectively). The alignment patterns are also sketched beneath corresponding snapshots. The strand numbers are labeled at the N-termini. Hydrogen bonds involved in the predominant β -sheet regions are marked, with antiparallel hydrogen bonds labeled in double short lines, parallel hydrogen bonds labeled in forward/back slashes.

In Figure 3.10, snapshot 2 is a β -sheet trimer with parallel in-register hydrogen bonding pattern. It undergoes a complete detachment process. All the hydrogen bonds are lost in snapshot 3. The reattachment occurs in snapshot 4 where a new β -sheet trimer is formed. The three strands involved (1, 2 and 4) are arranged differently from the previous ones (2, 3 and 4). The hydrogen bonding pattern is changed to antiparallel. When the structure evolves to snapshot 5, a new strand is added to the trimer and a β -sheet tetramer forms.

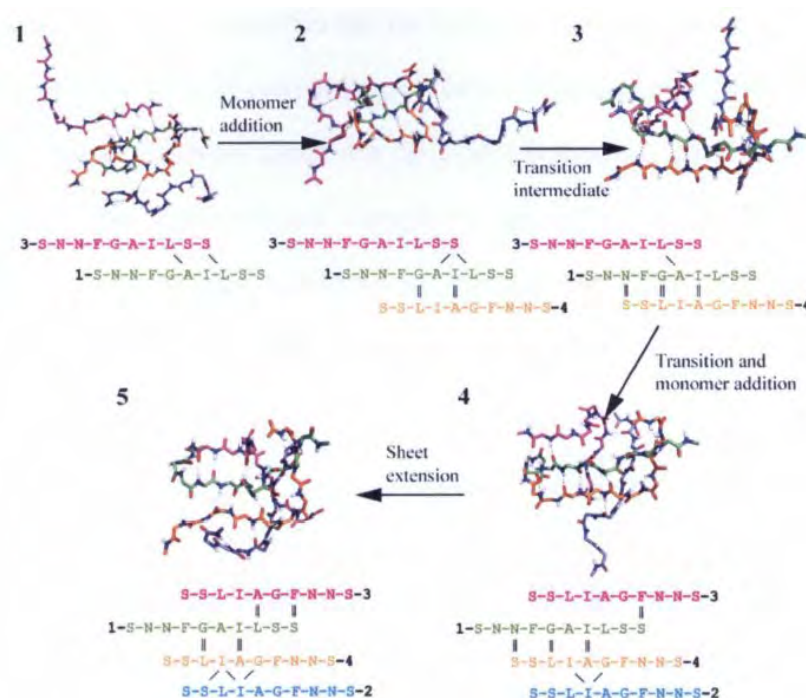
Sequence Variation of IAPP₂₀₋₂₉

Figure 3.11 Parallel-to-antiparallel transition path 2. The representation scheme is the same as in Figure 3.10.

The transition from parallel to antiparallel β -sheet also occurs through path 2 (Figure 3.11). Such transition does not need a complete detachment process as in path 1. It involves only internal reorganization. In this case, one single hydrogen bond in the parallel pattern remains and the whole strand rotates by 180° around the hydrogen bond. Afterwards the nascent antiparallel hydrogen bonds will form near the position of the original hydrogen bond.

3.7. Summary

Distinct aggregation behaviors of two variants of IAPP₂₀₋₂₉ were observed in two all-atomic REMD simulations. An explanation was suggested on how the proline substitutions influence the amyloid aggregation capacity of rIAPP₂₀₋₂₉. Preference for

Sequence Variation of IAPP₂₀₋₂₉

antiparallel interstrand orientation and the lack of uniform registration alignment are the two characteristics of early-stage per-nucleus oligomers of segment hIAPP₂₀₋₂₉. Critical residues which are responsible for β -sheet formation (A25, I26, and L27) are recognized. The rapid-collapsed amorphous aggregates can evolve to partially ordered β -sheets through conformational rearrangements and two pathways of parallel-antiparallel transitions are traced.

4. Lipid Acts as an Aggregation Catalyst

The disruption of integrity of cellular membranes induces cell apoptosis. The toxicity of amyloidogenesis is attributed to the interactions of amyloidogenic peptide with cellular membrane and the damaged integrity of cellular membrane induced by such interactions. On the other hand, peptide aggregation can be accelerated by acidic membranes [85], as well as some free fatty acids and lipid molecules [150, 151]. Furthermore, mature amyloid fibrils *in vivo* show a ~10% uptake of lipid molecules [85]. Therefore, it is attracting and important to study the interplay between amyloidogenic peptides and lipids, to learn how lipid molecules affect the aggregation process. In the published works, the lipid-associated peptide toxicity and aggregation has been widely established under a variety of lipid models such as micellar [152] and bilayer membranes [85], even free fatty acids and lipids [150, 151]. Bilayer membranes are the most potent lipid phase that accelerates aggregation and the most prevailing state of lipid molecules existing *in vivo*. Dioleoylphosphatidylcholine (DOPC), as a common lipid model to form bilayer membranes *in vitro*, was used in our simulation (Figure 4.1). The parameters of DOPC were derived from molecules with similar chemical structures or functional groups in OPLS-AA force field to be compatible with peptide parameters. The simulation protocol was applied to be consistent with the aforementioned REMD simulation for hIAPP system with the aim of comparing the two systems with or without lipid molecule. One DOPC molecule was added to all four initial structures of hIAPP in the middle of box parallel to peptide strands (Figure 3.1). To be differentiated from previous simulation without lipid, the current system was referred to as hIAPP/lipid hereafter.

Lipid as an Aggregation Catalyst



Figure 4.1 Molecular structure of DOPC.

The molecule was shown in ball-and-stick, with carbon atoms in black color, oxygen in red, nitrogen in blue, and phosphorus in orange. All hydrogen atoms were omitted for the sake of clarity.

4.1. Lipid Stabilizes Low-Level β -Sheet Oligomers

Similarly to Figure 3.9, we also plotted the distribution of peptide aggregates on different numbers of β -bridges (N_B) for hIAPP/lipid system (Figure 4.2). In hIAPP/lipid system, ordered aggregates with $N_B > 7$ have larger population compared to hIAPP. The transition points for dimer to trimer and trimer to tetramer in hIAPP/lipid are slightly smaller than hIAPP system ($N_B = 5$ verse 6 and $N_B = 11$ verse 12). The two illustrative sketches for trimers and tetramers at transition points clearly shows that one less β -bridge is needed for the transition of β -sheet oligomers in the presence of DOPC. It is likely that in the absence of lipid molecules, lower-level β -sheet oligomers are transient and very soluble which makes it incompetent to act as a template for monomer addition. However, binding to lipid molecule helps stabilize the lower-level oligomers from dissociation and thereby accelerates the emergence of higher-order β -sheet oligomers.

Lipid as an Aggregation Catalyst

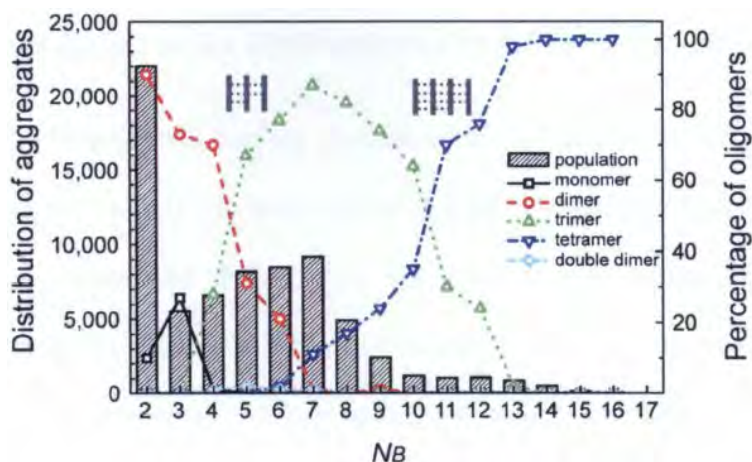


Figure 4.2 Distribution of aggregates on different N_B and increasing size of β -sheet oligomers with the increase of N_B in the presence of DOPC. The population of aggregates forming certain value of N_B is shown in bar. Percentage of β -sheet oligomers (β -sheet dimer, trimer, tetramer, and double dimers) is represented by lines and symbols.

The β -sheet oligomers are thermally stabilized by the lipid molecule. Figure 4.3 shows the temperature dependence of averaged number of β -bridges N_B . Because hydrogen bonds are not thermally stable at high temperature, in both two systems N_B decreases slowly to zero when the temperature increases to over 500K. But at nearly all temperatures, N_B of hIAPP/lipid is greater than hIAPP indicating the increased thermal stability of oligomers by binding to lipid. The melting temperature (where $N_B=3.5$) is 380K for lipid-free aggregates and increases to 400K in the presence of lipid.

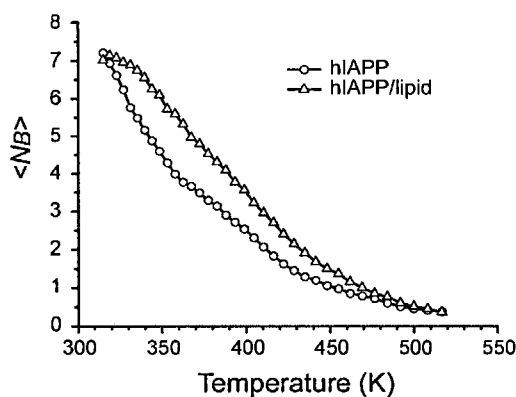


Figure 4.3 Temperature dependence of averaged number of β -bridges, N_B .

4.2. Lipid Binds to the Hydrophobic Patches on Peptide Oligomers

To probe the lipid-peptide binding manners in a statistical way, the occurrences of atomic contacts (N_C) between heavy atoms on lipid head/tail groups and $C\alpha$ atoms on hIAPP₂₀₋₂₉ are calculated (Figure 4.4). All residues have similar probabilities of interacting with the head group. The normal way of having such contact is through hydrogen bonding between the head group and polar side chains. In contrast, the probabilities of contacts with the tail group for different residues are quite distinct. Nonpolar residues show obviously higher inclination, especially for residues F23, G24, and A25, indicating a specific lipid binding site. The binding site is the exact region which has high SSP for turns and bends in the absence of lipid (Figure 3.6). Specific binding of the hydrophobic lipid tail on hIAPP has increased the propensity for β -structure of two residues F23 and G24 in this region (Figure 4.4B) and their propensities for turns and bends are correspondingly reduced.

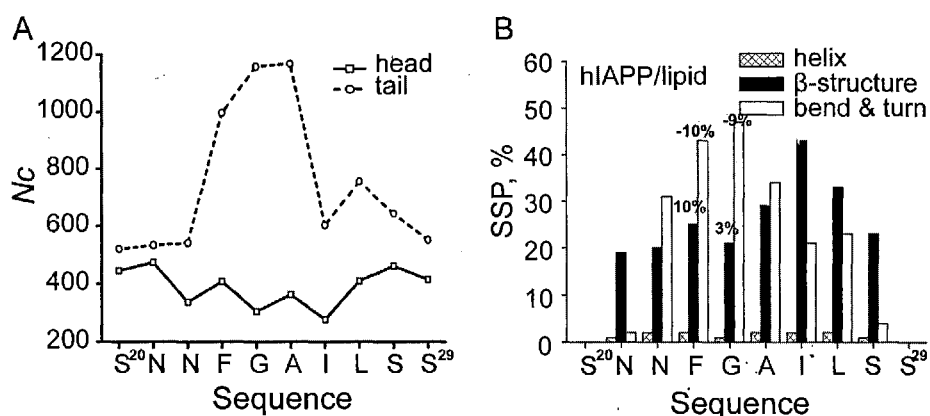


Figure 4.4 Atomic contacts of DOPC with $C\alpha$ on peptides and secondary structure propensities of residues in hIAPP/lipid system. A. Atomic contacts between lipid heavy atoms on head/tail groups and $C\alpha$ atoms on peptides. B. Secondary structure propensities of residues in the presence of DOPC. Compared to the pure peptide system (Figure 3.6), the increased SSP percentages for β -structure of F23 and G24 and the corresponding decreased SSP percentages for bend and turn are indicated.

Lipid as an Aggregation Catalyst

It is well known that amyloid β -sheet structure is stabilized not only by backbone hydrogen bonds network but also by close side chain packing. In Figure 4.5, two representative structures with the largest number of extended β -bridges from two hIAPP simulations are shown. Nonpolar surfaces are coalescent into a patch because the hydrophobic residues are prone to contact with each other. In the presence of DOPC, the lipid molecule is selectively docked onto the hydrophobic patches. The β -sheet region is undoubtedly stabilized through lipid binding on such hydrophobic patch which makes the hydrophobic clusters dissociate much more difficult. This also explains why smaller value of N_B is needed to maintain β -sheet oligomer in hIAPP/lipid system. In contrast, large hydrophobic patches in pure hIAPP oligomer are exposed to solvent, which absolutely reduces the overall stability and solubility of the oligomer.

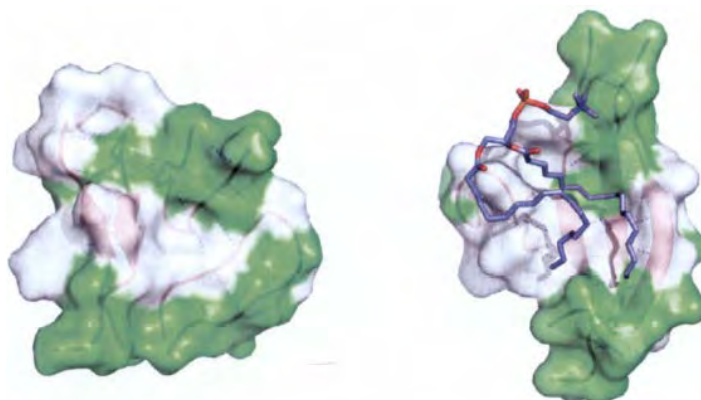


Figure 4.5 Representative structures with the largest number of β -bridges in the absence and presence of DOPC. The snapshot from hIAPP (left) contain 14 β -bridges. The snapshot from hIAPP/lipid (right) contain 16 β -bridges. Peptides are shown in cartoon, red and dashed lines indicate the backbone hydrogen bonds. White color indicates hydrophobic surface (residues F23, A25, I26, L27), green color indicates polar surface. The tail of the lipid molecule (right, in blue stick) binds to the hydrophobic surfaces of the oligomer.

4.3. Summary

The lipid-bound oligomers of hIAPP₂₀₋₂₉ are more thermal stable than lipid-free oligomers. A specific binding site was located at residues F23, G24, and A25. The specific interactions between the lipid tail and these hydrophobic residues are found to reduce the SSP for turns and bends, but correspondingly enhance β -structures, indicating a catalysis role of lipid molecule in peptide aggregation. The findings here are applicable to other types of amyloidogenic peptides and indicate a general pattern of interaction between lipid and amyloidogenic peptides [153, 154].

5. Inhibitory Effect of Resveratrol on hIAPP₂₂₋₂₇ Aggregation

In this chapter, we attempted to characterize the interactions between a small molecule, resveratrol, and an aggregating segment, hIAPP₂₂₋₂₇. A large body of experimental data on compounds which are active in anti-aggregation is available. Among many options, resveratrol was chosen for this study because the chemical structure is simple for molecular modeling. And the compound has been long studied in terms of its anti-oxidative, anti-inflammatory, and anti-cancer effect. It is a well known constituent of red wine and a small polyphenol compound found to be capable of inhibiting hIAPP fibril formation efficiently [102, 108, 155].

Up to date, using all atomic simulations to study peptide self-assembly, the length of the peptide is still sacrificed for copies of the peptide. The shortest amyloidogenic segment of hIAPP was chosen to be the subject peptide in our study. The hIAPP₂₂₋₂₇ segment alone was found to be amyloidogenic and capable of forming the typical amyloid fibrils [156]. The sequence NFGAIL was rendered three residue mutations in rodent IAPP (NLGPVL), which together with three other mutations in full-length IAPP define the divergent aggregation ability of rodent species [30, 156]. Segment hIAPP₂₂₋₂₇ is hydrophobic and the aromatic residue F23 is believed to play a key role in aggregation through the formation of aromatic interactions. Given the aromatic nature of resveratrol, similar aromatic interactions could be important in the inhibitory activity [107, 157]. Therefore, hIAPP₂₂₋₂₇ is a suitable model peptide to study amyloid aggregation. Our goal was to investigate the effect of the inhibitor on the early steps of aggregation rather than the interaction of the inhibitor with pre-formed fibril. Extensive REMD simulations were performed on seven copies of the

Inhibitory Effect of Resveratrol

short peptide. To accelerate the aggregation process a β -sheet tetramer was preformed as aggregation starting point and three free peptides were added. The self-assembly of the short peptide was studied with and without resveratrol. By comparing the aggregation behaviors of the two systems, inhibitory effect was observed and some insights into the underlying mechanism were disclosed. Characterizing the interactions between the two entities not only help understand the inhibitory mechanism of anti-aggregation compounds but also help develop novel drugs with higher efficacy.

5.1. Parameterization and Validation of Resveratrol Molecule

The structure of the small molecule resveratrol is shown in Figure 5.1. The initial topology of trans-resveratrol was generated in Spartan and energy minimized [158]. After geometry optimization at HF/6-31G* level using Gaussian09 [159], atomic partial charges were derived using R.E.D. III package [160]. Other bonded and nonbonded parameters of resveratrol were taken from the OPLSAA force field [161].

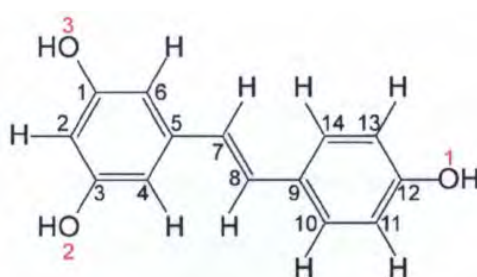


Figure 5.1 Molecular geometry of trans-resveratrol. All carbon atoms are distinguished by sequential numbers (black) and oxygen atoms on three hydroxyl groups are labeled by numbers in red.

To validate the force field parameters of resveratrol, we calculated the solvation free energy, ΔG_{sol} , in both Gaussian 09 and GROMACS simulation package [129]. By employing the PCM (polarizable continuum model) solvation model in Gaussian [162], we determined the value of ΔG_{sol} to be -20.56 kcal/mol at B3LYP/6-31G**

Inhibitory Effect of Resveratrol

level. We also calculated ΔG_{sol} using the thermodynamic integration (TI) method. One resveratrol molecule was inserted into a cubic box filled with 1356 SPC water molecules. Then the system was subjected to a series of NPT simulations by using an increasing coupling parameter, λ . 19 equally spaced values of λ were chosen ($\lambda=0.05, 0.10, 0.15 \dots 0.95$). The starting potential energy function of the system is the fully interacting resveratrol and solvent, and the end state is two completely decoupled systems: resveratrol in vacuum and pure solvent. Electrostatic and Lennard-Jones interactions were separately turned off, and a soft-core potential was used to scale Lennard-Jones interactions [163, 164]. We chose a set of run parameters similar to other's published work [164]. The production simulation at each λ lasted for 2ns. The determined value of ΔG_{sol} is -17.98 kcal/mol by TI method which is reasonably consistent with the estimate of -20.56 kcal/mol by Gaussian. Therefore, we conclude that our molecular model for resveratrol is reliable.

5.2. Simulation Setup

We chose a short segment of hIAPP₂₂₋₂₇, as a peptide model to study amyloid aggregation [157]. The initial conformation for our simulations contains a parallel- β -sheet tetramer centered in a dodecahedron box with a size of 40 Å. The tetramer is surrounded by three monomers, each of which is rotated 120° from one another and placed at least 10 Å from the β -sheet (Figure 5.2). We refer to the four peptide strands in the preformed β -sheet as “preformed β peptides” (PBP). The three peptide monomers which were initially positioned away from PBP are referred to as “added peptide monomers” (APM). To cover more sampling space, the APM were rotated around PBP 30° each time to generate totally four different initial configurations

Inhibitory Effect of Resveratrol

(after four-times rotation, APM peptides will construct the same conformational configuration as the one without rotation, therefore we do not consider further rotation). The N and C termini of hIAPP₂₂₋₂₇ were capped by acetyl (ACE) and N-methyl (NME) groups. We expect that PBP tetramer can act as an aggregation seed to accelerate the overall aggregation process. But the PBP was not subjected to any type of restraints during simulations because tetrameric β -sheet for such short peptide is neither stable nor competent to work as an aggregation nucleus. In fact, the PBP was found to be partially stabilized and undergo large structural fluctuation and reorganization as we expected.

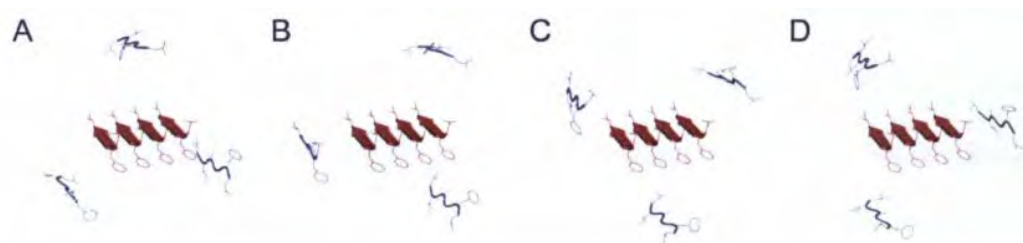


Figure 5.2 Cartoon representation of four initial configurations of seven strands of hIAPP₂₂₋₂₇. In each initial configuration, a preformed parallel- β -sheet tetramer (in red) is in the center surrounding by three added peptide monomers (in blue) placed at least 10 Å far from the tetramer. The rotational degrees for triple free peptides differ in four initial configurations to cover all the space 360° around the central tetramer.

The simulation of peptides enables us to look at the early stages of peptide aggregation. In order to study the inhibition mechanism, 12 resveratrol molecules were added to the peptide system. We chose a comparable concentration of resveratrol to most of the *in vitro* experiments and achieved an inhibitory effect in a computationally feasible timescale [102, 108, 155]. The insertion of inhibitors into the peptide system was random and close contacts with peptides were avoided.

Inhibitory Effect of Resveratrol

A temperature swapping REMD simulation scheme was performed by using the Gromacs simulation package with OPLSAA (all-atom) force field [129, 161]. 32 replicas were used and temperatures are listed here: 315.0K, 318.5K, 322.2K, 325.8K, 329.5K, 333.2K, 337.0K, 340.7K, 344.6K, 348.4K, 352.3K, 356.2K, 360.2K, 364.2K, 368.3K, 372.3K, 376.5K, 380.6K, 384.8K, 389.0K, 393.3K, 397.6K, 402.0K, 406.4K, 410.8K, 415.3K, 419.8K, 424.4K, 429.0K, 433.6K, 438.3K, and 443.1K. Each set of replica exchange simulations (one for the peptide system, and one for the combined peptide/inhibitor system) lasted for 500ns. The mixture of peptides and inhibitors was solvated in SPC water (1845 water molecules in hIAPP system and 1681 in hIAPP/resveratrol system). All bonds involving hydrogen atoms were constrained in length according to LINCS protocol [138]. Electrostatic interactions were treated with the Particle Mesh Ewald (PME) method with a cutoff of 9 Å, and a cutoff of 14 Å was used for the van der Waals interactions [139]. The integration step was set as 0.002 ps and non-bonded pair list was updated every 5 integration steps. The solutes and solvents were separately coupled to the external heat bath with the relaxation time of 0.1 ps. Replica exchange was attempted every 1000 integration steps (2 ps). The structure snapshots were output every 1 ps, and an ensemble of 500,000 structures at any temperature was produced for the analysis. Except properties monitored in a time period, all other analyses only used the data from the last 300 ns.

5.3. Evolution of β -Structures in the Absence/Presence of Resveratrol

The assembly progress of the hIAPP₂₂₋₂₇ peptide was monitored by examining the β secondary structure evolution in the presence and absence of the inhibitor (Figure

Inhibitory Effect of Resveratrol

5.3). All the data are obtained from the lowest temperature ensemble (315K). The formation of β secondary structure was quantified by β -content, the ratio of the number of residues in β secondary structure over the total number of residues (42 in this study). In the initial structures, a parallel β -sheet composed of four preformed β peptides (PBP) was formed, with three added peptide monomers (APM), as described in section 5.2. Because of the different initial states, the β -content of peptide aggregates was traced separately for PBP and APM.

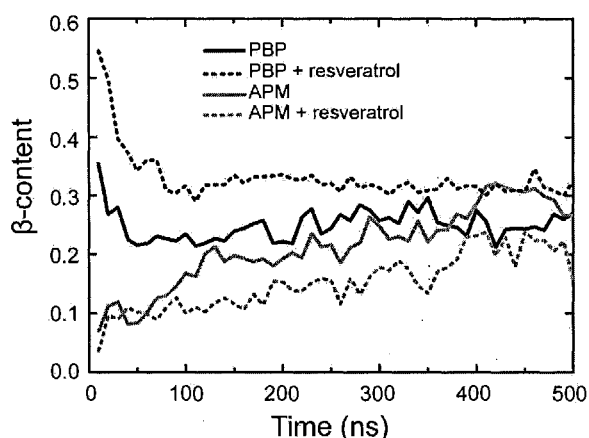


Figure 5.3 Time evolution of the β -content of PBP and APM in the absence and presence of resveratrol. β -content is the ratio of the number of residues in β secondary structure and the total residue number of 42. Each data point on the curves is an average over 10000 time frames (10 ns). The secondary structures of peptides were assessed by DSSP package [130].

During the first 50 ns simulation of resveratrol-free system, the β -content in PBP sharply decreases and loses nearly half of the β -structure (black solid line). Afterwards β -content of the PBP fluctuates around 0.25 until the end of 500 ns simulation. The β -content of the APM gradually grows during the first 400 ns. After that the β -content arrives at the plateau of 0.25 (grey solid line). It is interesting to find that regardless of the initial configurations the peptides adopt, either in

Inhibitory Effect of Resveratrol

preformed β sheet or in random monomers, the β -content approaches 0.25 at the end of 500 ns simulation.

When 12 resveratrol molecules were added into the system, the peptides showed distinct self-assembly behaviors. After 100 ns the β -content of PBP is stabilized around 0.3 (black dotted line) which is higher than the value of the counterpart in the absence of resveratrol (~ 0.25). The evolution of β structures in APM is much slower which nearly takes 400 ns to reach a steady level (grey dotted line) to a value of ~ 0.20 which is smaller than the value of the counterpart in the absence of resveratrol (~ 0.25). It seems that the action of resveratrol is to maintain the preformed β -structure, but to prevent the monomers from forming extra β -structure. The different inhibitory effects of resveratrol on PBP and APM are further analyzed in thermodynamic view.

In the initial configuration of PBP, 15 backbone hydrogen bonds formed which could be regarded as preformed hydrogen bonds. To trace their survival during the simulation, in each snapshot a ratio between the number of hydrogen bonds belonging to the preformed ones and the total number of hydrogen bonds was calculated. The evolution of the ratio was plotted in Figure 5.4A. The corresponding histogram statistics of the ratio were shown in Figure 5.4B. At the ratio of 0 where all preformed hydrogen bonds are lost, the population of cases without resveratrol nearly doubles the cases with resveratrol. The loss of preformed hydrogen bonds can happen in the process of dissociation and re-association of peptides, as well as reorientation from parallel to antiparallel β -sheets. On the other hand, the high peak at ratio of 0.65 for the system in the presence of resveratrol indicates that resveratrol stabilizes the preformed hydrogen bonds. The population analysis clarifies our

Inhibitory Effect of Resveratrol

aforementioned speculation about the higher β -content found in PBP that resveratrol molecules protect the existing β -sheet oligomers against reorganization.

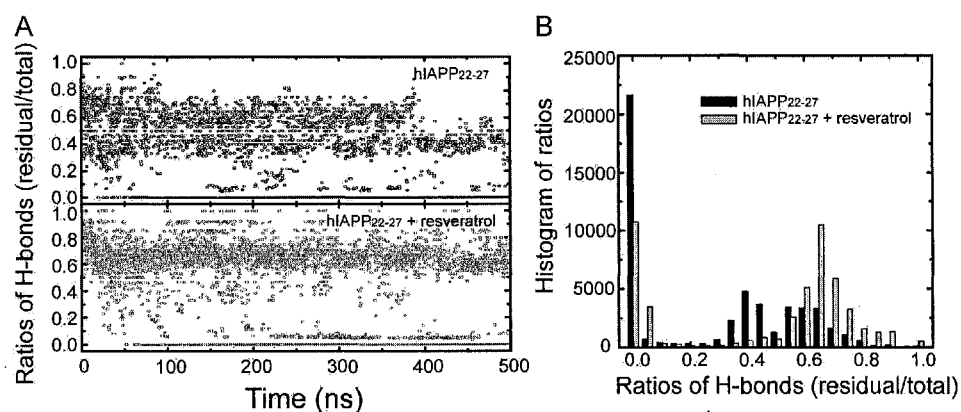


Figure 5.4 Tracing the survival ratio of the preformed hydrogen bonds and its histogram statistics. An amount of 15 backbone hydrogen bonds within PBP are regarded as preformed hydrogen bonds. The statistics is based on a subset of data from 500 ns simulations.

5.4. Thermodynamic Evidence of the Inhibitory Effects of Resveratrol

We compared the population of monomeric peptides and β -content as a function of temperature for the system with and without resveratrol (Figure 5.5 and 5.6). Data were analyzed based on the last 300 ns simulations at all temperatures. The amount of monomeric peptides remaining in solution is a normal measure in experiments to detect the extent of amyloid aggregation [165]. In the presence of resveratrol, the abundance of monomers unambiguously exceeds that in absence of resveratrol at all temperatures, indicating the inhibitory effect of the compound on peptide aggregation (Figure 5.5). The result of β -content illustrates the same effect (Figure 5.6A). Despite the equal amount of β -structure at low temperatures, the β -content at higher temperatures is evidently lower in the presence of resveratrol.

Inhibitory Effect of Resveratrol

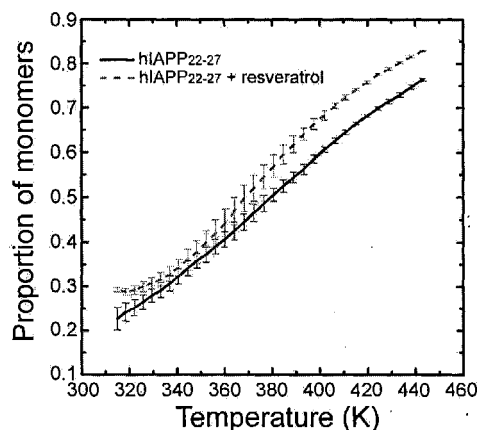


Figure 5.5 Temperature-dependent proportion of peptide monomers. Proportion of monomers is calculated as the ratio of the number of monomers and total number of peptide strands. Error bars are obtained from the standard deviation of three average values from nonoverlapping time blocks: 200-300 ns, 300-400 ns, and 400-500 ns.

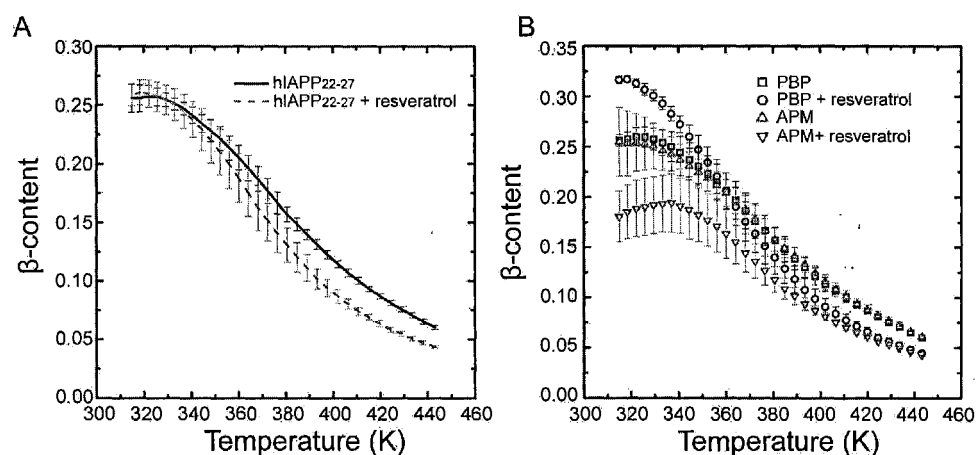


Figure 5.6 Temperature-dependent β -content of peptide aggregates and decomposing β -content into contributions from PBP and APM. Error bars are obtained from the standard deviation of three average values from nonoverlapping time blocks: 200-300 ns, 300-400 ns, and 400-500 ns.

In Figure 5.6B, the calculation of β -content is broken down into PBP and APM peptides. The plot clearly shows that resveratrol acts differently on preformed β -

Inhibitory Effect of Resveratrol

sheet and monomers in solution. PBP peptides possess ~17% more β -structure than APM peptides at 315K in the presence of resveratrol and the difference eventually vanishes when the temperature is above 400K. In contrast, without resveratrol, content of β -structure in PBP and APM is the same at each temperature indicating the independence upon the initial structures. In line with the previous results of β -structure evolution at 315K, the effects of resveratrol are conformational-state-dependent: inhibiting the β -sheet transition of monomeric peptides while holding the existing β -structure.

5.5. Early hIAPP₂₂₋₂₇ Oligomers in a Double-Layered β -Sheet Arrangement

After 500ns simulation, some of the initial β -sheet tetramers evolve to higher level oligomers such as pentamers, hexamers, and heptamers. Occasionally, a second oligomer other than the original tetramer could form either by the three initial monomers or also involving PBP dissociated from the β -sheet tetramers. To characterize all the aggregates with different configurations of oligomers at 315K, we defined hIAPP₂₂₋₂₇ oligomers based on two separate criteria. The first one is that at least two interstrand backbone hydrogen bonds are formed within two β strands. Under this criterion, peptide oligomers can be defined as different β -sheet oligomers (BSO). The second criterion is based on inter-residue distances regardless of the formation of hydrogen bonds: at least four pairs of residues must form interstrand atomic contacts. An atomic contact between two residues is considered to be formed when the minimum inter-residue distance between any pair of heavy atoms is less than 5 Å. Based on this criterion, oligomers can be defined as collapsed oligomers (CLO). In this definition, the criteria of two hydrogen bonds for BSO and 4 atomic

Inhibitory Effect of Resveratrol

contacts for CLO are somewhat arbitrarily chosen. We found that changing these thresholds could change the population of different aggregates; however, the relative results regarding the behavior in the absence or presence of resveratrol were tolerant to the changes. On the basis of either of the definitions, each aggregate comprising of the seven peptide strands can be characterized by its constituting oligomers (either BSO or CLO).

The configuration of heptameric aggregates can be described by the number of oligomers (either BSO or CLO) and the size of each oligomer *per se* which is the number of its constituting peptides. We used the following convention based on the size to label the species (or configuration) of the aggregates. For example, “7” or “7*” means the seven peptides form a heptameric BSO or CLO. The asterisk was used here to indicate CLO oligomers. “6.1” means two BSO oligomers in which one is hexamer and one is monomer. The digit “1” is omitted for simplicity so that “6.1” is simplified to “6”. Therefore, the system label of “4” is in fact “4.1.1.1” which means 4 different oligomers with one being tetramer and three being monomers. The reason we used two criteria is that they can provide complementary information. For example, for a configuration with two BSO, the information of whether the two BSO are close to each other in space is lost. If we know that the two BSO belong to one CLO, it is clear that the two BSO are close in space; otherwise, the two BSO are far away from each other. The species distributions of aggregates on the basis of two criteria are shown in Figure 5.7 A and B.

Inhibitory Effect of Resveratrol

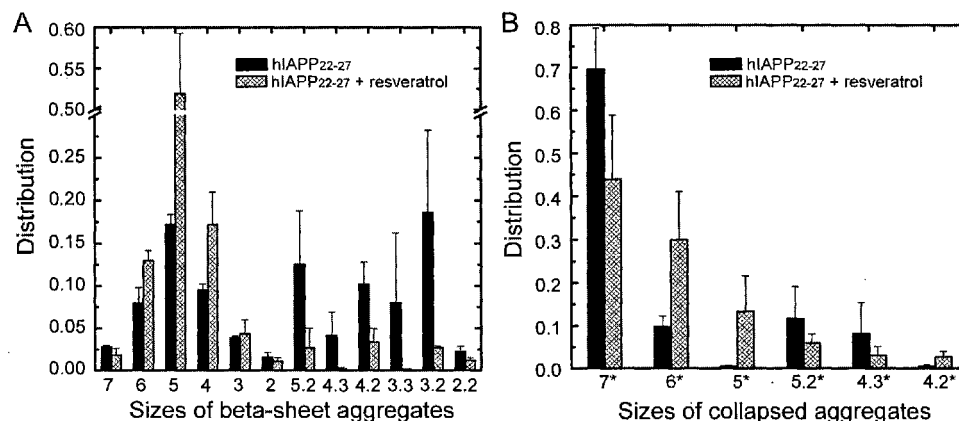


Figure 5.7 Species distribution of β -sheet aggregates and collapsed aggregates. The species of β -sheet aggregates are identified by using criterion for BSO (A), and species of collapsed aggregates are identified by using criterion for CLO (B). The definitions of BSO and CLO are described in the main text. Those aggregate species with very small population are excluded from figures.

In the absence of resveratrol, the species distribution of β -sheet aggregates (Figure 5.7A, black bars) indicate peptides have equal probability to form single-sheet (or single-BSO, including size 7, 6, 5, 4, 3 and 2) aggregates and double-sheet aggregates (size 5.2, 4.3, 4.2, 3.3, 3.2 and 2.2). The evidence that 70% of aggregates are heptameric CLO (size 7*, Figure 5.7B) implies that 70% of aggregates in all BSO configurations have their component strands packed into condensed aggregates. According to our simulations, high-level single-layered β -sheets, i.e., BSO species as 7 and 6 have very small population, which indicates that elongation along a single β -sheet may not be the primary mode of nucleation formation. Instead, the formation of double-sheet aggregates to a great extent is an unexpectedly critical event in the early stage aggregation.

To characterize the structures of the double-sheet aggregates, an RMSD clustering was performed. For different aggregate species, the structures of the cluster center of

Inhibitory Effect of Resveratrol

the top-ranked clusters were taken as representative structures and are shown in Figure 5.8. The percentage of the top-ranked cluster in each species is also shown in parentheses. The RMSD calculation was based on heptamers, and unstructured monomers can cause large RMSD fluctuations which result in bad clustering results without a dominant top-ranked cluster, such as for size 2.2 (only 8.0%).

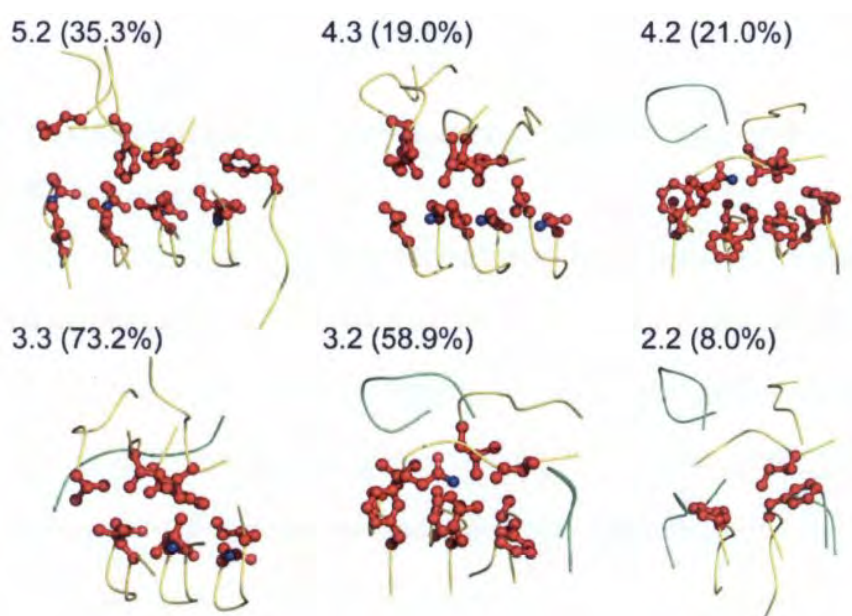


Figure 5.8 Representative structures of aggregates with double β -sheets in the absence of resveratrol. The percentages in parentheses show how populated the first-ranked cluster is in the overall aggregates of certain species. The stacking side chains are marked in red, ball-and-sticks. Peptide backbones are shown in ribbons, yellow for oligomers and green for monomers.

In these double-sheet aggregates we found that one layer of β -sheets usually evolves from the PBP which we refer to as primary β -sheet; and the other layer is formed by self-assembly of APM, which we refer to as the secondary β -sheet. The secondary β -sheet (upper β -sheet layer in Figure 5.8) tends to lay parallel with the primary β -sheet (lower layer) involving extensive side chain stacking interactions (explicitly shown

Inhibitory Effect of Resveratrol

in red balls-and-sticks), in a face-to-face configuration. Such arrangement prevents exposure of hydrophobic residues to solvents and thereby stabilizes the stacking β -sheets. Even in the small aggregates, such as double dimers (species 2.2), the face-to-face inter-sheet interaction is already formed, suggesting a natural pathway that lateral extension occurs simultaneously with elongation at the very early stage of amyloid aggregation.

5.6. Destabilization of Double-Layered β -Sheet Aggregates by Resveratrol

The species distributions of peptide aggregates in the presence of resveratrol are clearly different from those without resveratrol (see Figure 5.7 grey bars). Compared with inhibitor-free aggregates, the presence of resveratrol greatly increases the population of monomers, such as species “6”, “5”, “4”, as well as “6*”, “5*”, “4*”. The result agrees well with our previous observation which suggested the induction of a higher population of monomers by resveratrol molecules (Figure 5.5). On the other hand, the population of aggregate species with double β -sheet oligomers is greatly reduced. The representative structures of double-sheet aggregates with resveratrol are shown in Figure 5.9. In the presence of resveratrol, the hydrophobic residues are buried more favorably by the amphiphilic compounds than by side chains of the other strands. The double-sheet aggregates are more disordered than those in the absence of resveratrol. The two β -sheets do not have the feature of parallel stacking as seen in the inhibitor-free simulations.

Inhibitory Effect of Resveratrol

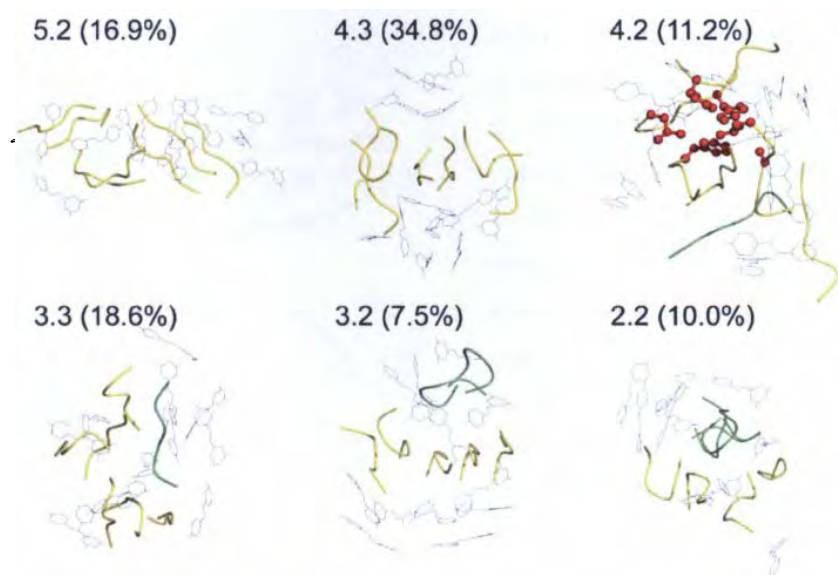


Figure 5.9 Representative structures of aggregates with double β -sheets in the presence of resveratrol. The percentages in parentheses show how populated the first-ranked cluster is in the overall aggregates of certain species. The stacking side chains are marked in red, ball-and-sticks. Peptide backbones are shown in ribbons, yellow for oligomers and green for monomers. The resveratrol molecules are shown in black, line representation. In the presence of resveratrol, except for species 4.2, aggregates have no side chain contacts between the two β sheets.

In fact, in the absence of resveratrol, the structure of single-layered aggregates with a large BSO, such as heptamer (species 7), is not a normal twisted β -sheet. Instead it takes a form of β -barrel by wrapping inwards several side chains (Figure 5.10A1-2). In contrast, with the interference of resveratrol, heptameric β -sheet shows single-layered, twisted sheet morphology (Figure 5.10 B1-2). Resveratrol bind at the grooves of the twisted β -sheet. The β -sheet structures of the microcrystal derived from hIAPP₂₁₋₂₇ also demonstrate intimately steric zippering of side chains [166, 167]. Therefore, in addition to backbone hydrogen bonds, side chain interactions are also the main driving forces in the early aggregation stage.

Inhibitory Effect of Resveratrol

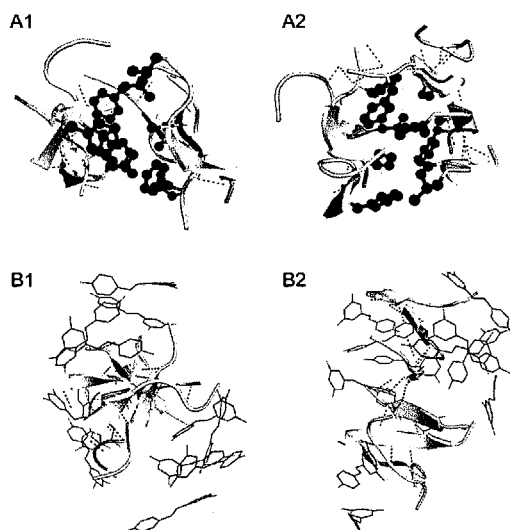


Figure 5.10 Representative structures of aggregates belonging to species 7 in a β -barrel (A) or single-layered configuration (B). Peptide backbones are shown in yellow, cartoon. In the absence of resveratrol (A1, A2), side chains wrapping inwards β -barrel are explicitly shown in red, ball-and-stick. In the presence of resveratrol (B1, B2), compounds surrounding peptides are shown. Dashed blue lines represent the hydrogen bonds formed on backbones.

5.7. Characterizing Six Binding Sites of Resveratrol on Pentameric Protofibril

A β -sheet pentamer (species 5) is the dominant species (>50%) of the aggregates in the presence of resveratrol (Figure 5.7). The formation of pentamers is via elongating the PBP tetramer by adding one APM peptide. Because of the abundance of such kind of aggregates, we focused on studying the binding preference of inhibitors on the pentamer. As a simple model, the β -sheet pentamer can be viewed as a truncated single-layer protofibril. The spatial distribution of resveratrol around the pentamer is illustrated in Figure 5.11.

Inhibitory Effect of Resveratrol

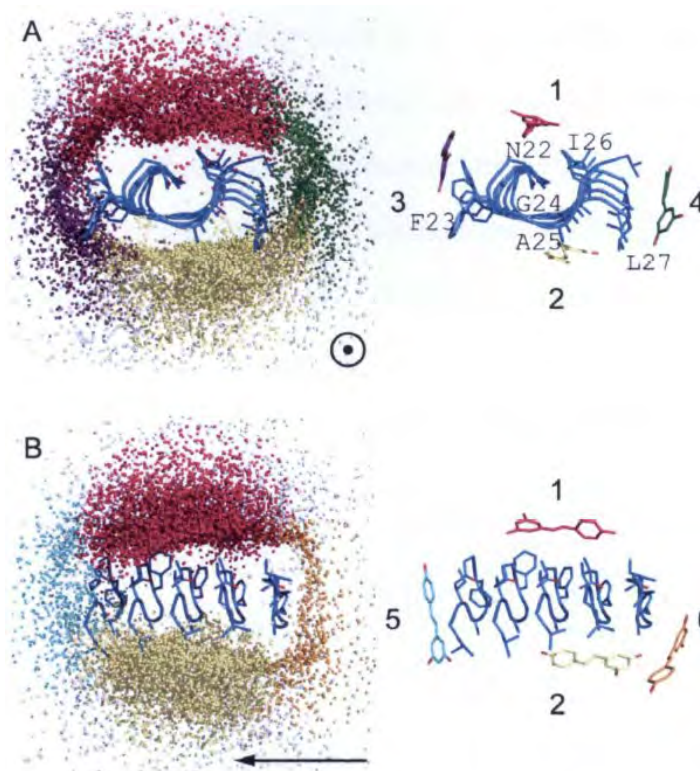


Figure 5.11 Six binding sites of resveratrol molecules on β -sheet hIAPP₂₂₋₂₇ pentamers and representative structures at each binding site. Oligomers of species 5 in Figure 5.7 was chosen and distribution of small molecules (colored dots) surrounding the β -sheet pentamers (blue) was drawn by superimposing the peptides in the middle. Roughly six binding sites are identified and presented by different colors (site 1 in hot pink, site 2 in yellow, site 3 in violet, site 4 in green, site 5 in cyan, site 6 in orange, and all the others in white). The corresponding representative structures are shown on the right. The arrows point to the direction of fibril elongation. Binding sites are shown in two directions: along direction of fibril elongation (A) and perpendicular to the direction (B). For the sake of clarity, sites on the front and back sides of the pentamers are not shown, corresponding to sites 5 and 6 in A and sites 3 and 4 in B.

The six-residue peptide is short and forms a turn-like, twisted parallel β -sheet instead of a flat β -sheet. The centers of mass of resveratrol molecules are marked as colored dots. Different colors differentiate six binding sites which are the most populated clusters in the rank of clustering all 12 resveratrol molecules in the aggregates of species 5. Structures belonging to the six binding sites cover 90.1% of all structures

Inhibitory Effect of Resveratrol

we examined. A generous RMSD cutoff of heavy atoms (1.25 nm) was used to consider only the positions of small molecules surrounding the pentamer and neglect their internal conformation and overall rotation. The preferences of the six binding sites are illustrated by the population of bound resveratrol there as well as binding energies calculated by MM-GBSA model (Table 5.1).

Table 5.1 Percentages and binding energies of resveratrol at six binding sites of β -sheet pentamers.

Binding site	Percentage (%) ^a	Binding energy (kJ/mol)		
		ΔE_{total} ^c	ΔE_{np} ^c	ΔE_{p} ^d
1	33.6	-51.0 \pm 8.7 ^b	-77.7 \pm 8.6	26.7 \pm 8.1
2	30.1	-36.6 \pm 7.2	-65.6 \pm 8.8	29.1 \pm 4.5
3	9.8	-21.7 \pm 5.6	-44.1 \pm 7.8	22.4 \pm 4.3
4	8.9	-35.7 \pm 8.2	-57.4 \pm 9.6	21.7 \pm 4.3
5	4.0	-34.1 \pm 6.4	-57.2 \pm 8.5	23.2 \pm 4.2
6	3.7	-18.6 \pm 6.4	-34.7 \pm 8.9	16.1 \pm 3.9

^a The value herein is the percentage of binding at each binding site in total binding on the β -sheet pentamers. Only those aggregates with a well-formed β -sheet pentamer (species 5) were taken into consideration and the percentage of these aggregates is \sim 50% as shown in Figure 5.7.

^b The values are standard deviations of 100 structures belonging to each class with resveratrol binding at different binding site.

^c ΔE_{np} is the sum of binding energies induced by van der waals interactions between resveratrol and peptides as well as SA (solvent accessible surface area) term in solvation energy.

^d ΔE_{p} is the sum of binding energies induced by electrostatic interactions between resveratrol and peptides as well as GB term in solvation energy.

^e ΔE_{total} is the sum of ΔE_{np} and ΔE_{p} .

High binding preference of resveratrol for the two surfaces of the protofibril (Site 1 and 2 in Figure 5.11) is clear, as indicated by both highest percentages (33.6% and 30.1% in Table 5.1) and lowest binding energies (-51.0 kJ/mol and -36.6 kJ/mol). To

Inhibitory Effect of Resveratrol

be noted, polar components ΔE_p are even higher than those binding at the other sites. But the unfavorable polar interaction is compensated by extremely favorable nonpolar component ΔE_{np} . The favorable van der Waals interactions benefit from the hydrophobicity of both side chains at the sites and the compound. In contrast, the compound binds less likely to the elongation edges (Site 5 and 6) as shown by the sparsely dot clouds along the elongation direction (Figure 5.11B). Percentages are the lowest for these two sites (4.0% and 3.7%) and binding energies are also higher (-34.1 kJ/mol and -18.6 kJ/mol). Although energy penalty originated from polar contacts is not as high as site 1 and 2 (23.2 kJ/mol and 16.1 kJ/mol at site 5-6 verse 26.7 kJ/mol and 29.1 kJ/mol at site 1-2), the hydrophilic nature of site 5 and 6 where backbone hydrogen bond donors and acceptors locate impedes the nonpolar contacts and makes them less preferential binding sites. The binding preference for site 3 and 4 is ranking in between the aforementioned two groups of binding sites in terms of percentages, ΔE_{total} , ΔE_{np} , and ΔE_p .

5.8. Inhibitory Activities of Resveratrol by Blocking Inter-sheet Side Chain Contacts

The lateral association of β -sheets is a prerequisite for further growth of amyloid fibrils and inter-sheet side chain interactions mainly drive and stabilize such kind of association. However, the extensively binding of resveratrol onto the surface of sheets can efficiently block the inter-sheet side chain interactions. We counted the atomic contacts of side chains of the primary BSO with the other peptides, and contacts of side chains of the primary BSO with resveratrol molecules (Figure 5.12). The two quantities have a strong anti-correlation, which unambiguously indicates

Inhibitory Effect of Resveratrol

resveratrol binding reduces probability of β -sheet formation in a double-layered arrangement.

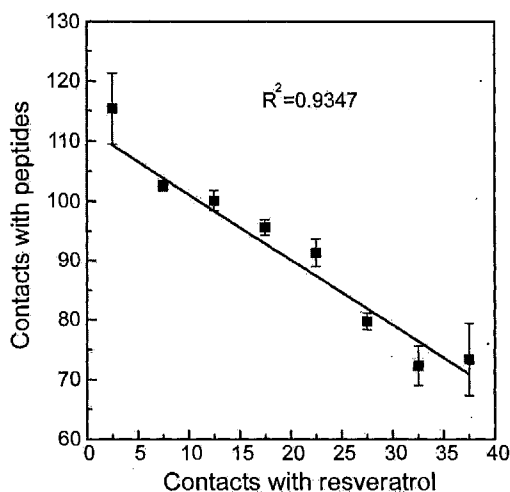


Figure 5.12 Correlation of side chain atomic contacts of the primary β -sheet with the rest peptides and with resveratrol molecules. Contact number with resveratrol (abscissa) was averaged over a bin of 5 contacts, and contact number with peptides (ordinate) was derived by averaging contacts of all data falling in the bin. Error bars indicate standard deviation of three time blocks: 200-300 ns, 300-400 ns, and 400-500 ns. The solid line is a linear fit to the data points. The two contacts are negatively linear-correlated.

To characterize the atomic detailed interactions between resveratrol and peptides, contact maps of four types of peptide-inhibitor interactions were drawn (Figure 5.13). Resveratrol interacting with four parts of peptides (side chains or main chains on BSO or monomers) was considered separately. One contact is believed to form when the distance of a pair of heavy atoms between two partners is smaller than 5 Å. We calculated the inhibitor-peptide contact numbers per frame per strand: 12.9 for BSO side chains, a similar value 12.7 for monomer side chains, 3.7 for BSO backbones, and 6.1 for monomer backbones. Transition from unstructured monomers to BSO limits the exposure of the backbones to the inhibitors by reducing nearly half of the contact numbers (from 6.1 to 3.7). Despite the similar contact numbers on side

Inhibitory Effect of Resveratrol

chains, when the peptide is in a monomeric state, resveratrol has an overwhelming preference for the aromatic F23 over the other two hydrophobic residues I26 and L27 (Figure 5.13D). The preference is attenuated when the peptide is part of a protofibril (Figure 5.13B). The result is consistent with the less frequently binding at site 3 where F23 locates as shown in Figure 5.11A. When inhibitors bind to the specific positions on ordered oligomers, stereospecific features, such as the existence of hydrophobic grooves on the surface are recognized by compounds. However, when inhibitors interact with unstructured monomers, there is no particular structural motif on the unfolded peptides. Therefore, rather than tertiary structures, physicochemical properties of the compound and single residue such as aromaticity or hydrophobicity determines the interactions.

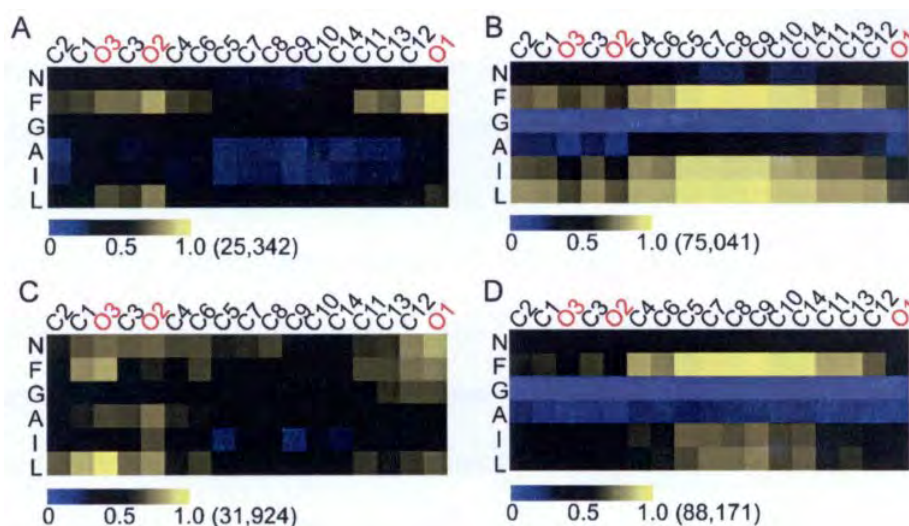


Figure 5.13 Contact maps of heavy atoms on resveratrol (abscissa) and on the residues of peptides (ordinate). The contact intensities have been normalized by dividing the individual largest contact occurrence number which is labeled next to the color bar. Contacts on residues have been divided into four groups: backbones of BSO (A), side chains of BSO (B), backbones of monomers (C), and side chains of monomers (D). The atoms of resveratrol are ordered according to the spatial proximity in chemical structure rather than sequence atomic numbers (see Figure 5.1 for the chemical structure).

Inhibitory Effect of Resveratrol

The middle region of resveratrol shows the largest contact intensities with side chains of peptides (Figure 5.13 B and D). In contrast, three hydroxyl groups on the resveratrol make polar contacts with peptides which are mainly located on the terminal residues (F23 and L27) and exclusively involved with backbones (Figure 5.13A). The information derived from contact maps confirm the previous results of the favorable nonpolar binding energies on site 1-4 and the less unfavorable polar binding energies on site 5-6 (table 5.1). And the differences of binding energies at different sites are mainly caused by physiochemical properties of the binding site.

5.9. Summary

Simulations conducted were used to compare aggregation behaviors of a short amyloidogenic peptide hIAPP₂₂₋₂₇ in the absence or presence of anti-aggregation compound, resveratrol. Inhibitory effect of resveratrol on the self-assembly of the short peptide was observed. A hypothesis of the underlying inhibition mechanism was suggested that resveratrol molecules redistribute the aggregate species. The double-layered β -sheet arrangement, which was believed to be important as an intermediate state on the pathway to mature multiple-layer fibrils, almost disappears when resveratrol interferes with the aggregation. Resveratrol molecules are capable of extensively binding to side chains of a single-layered β -sheet and therefore block the formation of double-layered β -sheets which is largely driven by side chain stacking interactions.

6. pH Effect on IAPP-Insulin Interactions

Human IAPP is known to be a peptide hormone co-expressed and co-secreted with insulin in β -cells of the pancreas [168]. It has been found that hIAPP remains soluble in secretory vesicles at a concentration range of 0.8-4 mM, whereas the critical concentration of hIAPP to convert into amyloid deposition is incredibly lower by orders of magnitude *in vitro* [169, 170]. Therefore, the *in vivo* environment, including pH values, ionic strength (Ca^{2+} , Zn^{2+}), and protein components such as insulin, proinsulin, and C-peptide, must play a critical role in avoidance of hIAPP misfolding into fibrillar amyloid [171, 172]. Among all the factors, acidic pH at ~ 6.0 and insulin whose concentration is at an ratio of $\sim 100:1$ to hIAPP in secretory vesicles are found to have significant impacts on the unnatural transition of hIAPP from soluble peptides to deposited amyloid fibrils [170]. Therefore, it is a fascinating subject of understanding how IAPP and insulin interact. A shortcoming of conventional MD for studying this subject is the difficulty to reach the convergence of binding sites within a computational feasible time scale, because the identified binding site depends heavily on the initial position of IAPP surrounding insulin. In this chapter, we used temperature-swapping REMD simulation scheme to enhance sampling of huge configuration space of insulin-IAPP complex at both neutral and acidic pH. The initial positions of IAPP relative to insulin allow for as more space as possible by rotating IAPP peptide around insulin. Simulations were performed for both rIAPP and hIAPP as ligands and hIAPP were simulated under both acidic and neutral pH. The influences of varied pH and H18R mutation on IAPP-insulin interactions are disclosed in the hope of providing information on devising potent peptide inhibitor of hIAPP amyloidogenesis.

6.1. Simulation Setup and Clustering Algorithm

6.1.1. Simulation Setup

A temperature swapping REMD simulation scheme was applied to dock rodent/human IAPP fragment comprising of residues 9-20 onto monomeric insulin (PDB entry code: 1MSO) [173]. The h/rIAPP sequences used herein are shown:



The one residue mutation at position 18 was underlined and shown in bold. To mimic the neutral and the low pH environments, all histidine residues whose pKa values are approximately 6.0 were modeled as deprotonated or protonated separately in two systems (referred to as hIAPP and hIAPP(His+) system hereafter). Because acidic pH does not change the protonated state of R18, rIAPP system was only simulated at neutral pH. The temperatures of 24 replicas are listed here: 315.0K, 318.1K, 321.2K, 324.4K, 327.6K, 330.8K, 334.0K, 337.3K, 340.6K, 344.0K, 347.4K, 350.8K, 354.2K, 357.7K, 361.2K, 364.8K, 368.3K, 372.0K, 375.6K, 379.3K, 383.0K, 386.8K, 390.6K, and 394.4K. The two simulations of hIAPP-insulin complexes lasted for 100ns. rIAPP simulations ended at 84 ns. N and C termini of IAPP₉₋₂₀ were capped by acetyl (ACE) and N-methyl (NME) groups, respectively. At the beginning of the simulations, IAPP peptide was modeled as an extended strand and randomly placed at a distance of approximately 15Å away from the insulin molecule. The protein complex was solvated by SPC water molecules in a dodecahedron box with a size of 50Å. The simulations were performed by using Gromacs simulation package with OPLS-AA force field [129, 161]. From our NMR data, the 3D fold of insulin is well

pH Effect on IAPP-Insulin Interactions

reserved in insulin titration experiments [104]. Thereby throughout all simulations, the positions of backbone atoms of insulin were restrained with side chains capable of rotating freely. All bonds involving hydrogen atoms were constrained in length according to LINCS protocol [138]. Electrostatic interactions were treated with the Particle Mesh Ewald (PME) method with a cutoff of 9 Å, and a cutoff of 14 Å was used for the van der Waals interactions [139]. The integration step was set as 0.002 ps and non-bonded pair list was updated every 5 integration steps. The solutes and solvents were separately coupled to the external heat bath with the relaxation time of 0.1 ps. Replica exchange was attempted every 1000 integration steps (2 ps). The structure snapshots were output every 1 ps, and an ensemble of 100,000 (or 84,000 for rIAPP) structures at 315.0K was produced for the analysis.

Two other control systems of an isolated hIAPP₉₋₂₀ segment were also subjected to similarly schemed REMD simulations. Residue H18 was modeled to be either protonated or deprotonated to mimic its charged state in neutral or acidic pH solution. The peptides were initially extended and placed in the center of a dodecahedron box with a dimension of 50*50*50Å. The simulations ended when they reached a logical convergence after 50 ns.

6.1.2. Clustering Algorithm

The REMD scheme enhances the IAPP-insulin complex configuration sampling in two aspects: recognition sites on insulin and conformations of bound-IAPP. Thus, the clustering analysis of conformational ensemble relied not only upon structure of IAPP but also upon recognition sites on insulin. A pair of intermolecular residues between IAPP and insulin is counted as a contact when the distance of any pair of

pH Effect on IAPP-Insulin Interactions

atoms is not larger than a cutoff distance, 4Å in our case. Several contacts can be grouped together as one binding site. Therefore, the first level of our clustering scheme is to search the correlated contacts and then group them together. Before grouping the correlated contacts, those random contacts each of which has an occurrence less than 5% were filtered out. After the filtering there were totally 44 contacts for hIAPP(His+), 79 contacts for hIAPP and 126 contacts for rIAPP left which were considered as the “conserved” contacts.

The correlation of these conserved contacts was analyzed in the following way. All contacts were ranked based on their occurrences. The first contact has the largest occurrence. The correlation degree of two contacts was defined as the ratio of the probability of the two contacts happening simultaneously to the probability of the contact with the lower occurrence. The correlation degrees for all contact pairs were calculated. Based on the distribution of the correlation degrees, a value of 62.5% was assigned to be the threshold of correlation: if the correlation degree is larger than this value, the two contacts are considered to be correlated and are classified into one contact group. Other contact can join the contact group only when the correlation degrees between this contact and all group members are larger than the threshold. One contact can be assigned into different contact groups. After the first level clustering all contacts were categorized into 13 contact groups for hIAPP(His+), 20 contact groups for hIAPP, and 21 groups for rIAPP, respectively.

The second level of clustering relies on heavy atom root-mean-square deviations (RMSD) of all structural snapshots belonging to a single contact group. The central structure of the most populated cluster was taken as the representative structure of

pH Effect on IAPP-Insulin Interactions

the group. After the first level of clustering by which contact groups were identified, we found that majority members of IAPP-insulin complex ensemble (62.37% and 97.58% for two hIAPP systems and 97.65% for rIAPP) have been selected which guarantees that the representative structures obtained from the second-level structure-based clustering have significant statistical meanings.

6.2. Insulin Binding Preserves Helical hIAPP at Acidic pH

To analyze the secondary structure propensity (SSP) of IAPP and also to verify the convergence of total five REMD simulations, the secondary structure (SS) composition of IAPP segments in the presence and absence of insulin was assessed. The SSP averaged over every 10 ns ensemble was plotted in Figure 6.1 A-C and Figure 6.2 A, B. The convergence of REMD simulations is demonstrated by the stable SSP values at the last half of the time blocks.

From the last 30 ns data of IAPP-insulin complexes, the SS compositions of hIAPP(His+) and rIAPP are quite similar, consisting of ~10% helices, ~15% turns, <1% β -hairpins (intra-peptide β -sheets), and ~75% bend and random coiled structures. By contrast, the structured content of hIAPP is extremely lower. The random coil structure dominantly takes up ~95% and the structured content (helices, turns, and β -sheets) only contributes ~5%.

pH Effect on IAPP-Insulin Interactions

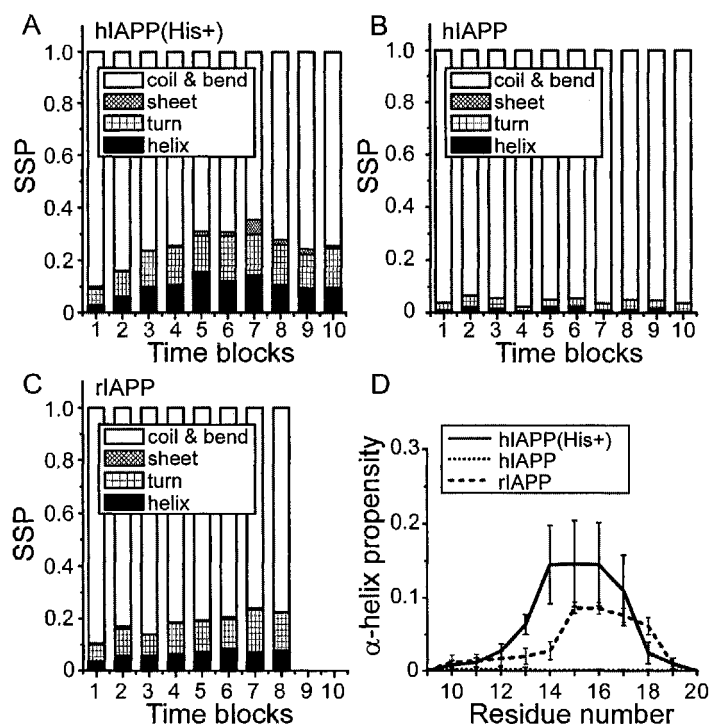


Figure 6.1 Convergence of insulin-IAPP complex simulation by monitoring secondary structure propensity. The trajectories at 315 K of the hIAPP(His+) (A), hIAPP (B), and rIAPP (C) were grouped every 10 ns. SSP of each time interval was calculated and shown in bars. D. Propensities for α -helix of each residue are compared. The helix propensities were calculated for every 20 ns of the last 60 ns trajectories at 315K. The values in figure D are averaged over the three time intervals. Error bars indicate the standard deviations of three calculated values.

Despite the different SS compositions of two bound hIAPP, their isolated forms seem to be of equal helicity because the helix compositions of both two maintain on a steady level of ~10% after 20 ns. (Figure 6.2 A, B). CD spectroscopy shows that random coil conformation dominates the SS composition of soluble IAPP in buffer and the helical conformation can be induced by membrane association [74, 86]. When the condition is changed from buffer alone to solution with lipid (DOPG), the helical content of IAPP increases from ~10% to 39-43% for hIAPP and 32-36% for rIAPP. The β -sheet content is reduced from ~30% to 10-15% for both peptides[74].

pH Effect on IAPP-Insulin Interactions

Although the ~10% helix of IAPP₉₋₂₀ segment in our simulations can not be directly compared with CD estimates (~10%) for full-length IAPP, the helical content of rIAPP segment is in good agreement with our previous NMR observation that 10-20% of residues 9-17 are estimated to be helical in the solution incubated with insulin [104].

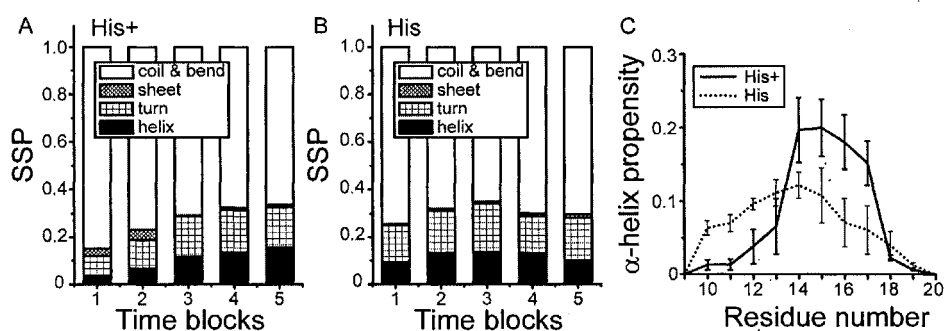


Figure 6.2 Convergence of isolated peptide simulation by monitoring secondary structure propensity. The trajectories at 315 K of the hIAPP(His+) (A) and hIAPP (B) were grouped every 10 ns and SSP of each time interval was calculated in the same way as in Figure 6.1. C. Propensities for α -helix of each residue are compared between simulations with H18 in different protonation states. The helix propensities were calculated for every 10 ns of the last 30 ns trajectories at 315K. Error bars indicate the standard deviation of three calculated values from their average.

The evidence of less helical content of bound hIAPP indicates that at neutral pH the peptide undergoes a conformational transition upon binding to insulin and unfolds most of its secondary structures which merely exist in isolated state. Unlike hIAPP with deprotonated H18, hIAPP(His+) reserves its α -helical region constituting residues 14-17 after binding to insulin (Figure 6.1D, 6.2C). It is noticeable that although helix proportion of hIAPP is on the same level to hIAPP(His+) in unbound form, its helical propensity is similarly ~10% for almost any residue, which is distinct from hIAPP(His+) whose helical region concentrates on only four residues

pH Effect on IAPP-Insulin Interactions

with a ~20% helix propensity. Therefore the helical structure of hIAPP transiently exists in neutral solution and the heterogeneous peptide ensemble makes it reasonable that most of the secondary structures are lost during insulin binding. Considering that insulin-bound rIAPP also has a similar propensity for helix to hIAPP(His+) (Figure 6.1D) but under a different pH condition, the change of electrostatic environment on insulin surface induced by two pH-sensitive interfacial His residues (H5 and H10 on B chain) is unlikely to be the determinant of helical ligand binding. The reduced helicity is due to the deprotonated H18 which possibly favors upstream helix in neither insulin-bound nor isolated hIAPP segment.

6.3. Residue Interface Propensities

The propensity for each residue taking part in the IAPP-insulin recognition, i.e., locating the binding interfaces, was evaluated by the ratio of occurrence that residues participate in the intermolecular contacts to the total number of examined snapshots (Figure 6.3 and Figure 6.4). It is encouraging to observe overwhelmingly higher residue interface propensity (RIP) values on insulin B chain (segment 9-18) and C-terminal regions (segment 20-30) than other regions. The interface regions predicted here are quite consistent with the two potential binding regions spanning residues 8-25 and 20-30 which was previously identified using peptide-array methodology [174].

In terms of RIP of insulin, the three simulation systems show a high degree of consistency. Residues with a higher interfacial preference are enumerated herein: Y14, N18, and N21 on A chain, and S9, H10, V12, E13, Y16, G20, E21, F24, F25, and Y26 on B chain. These kinds of amino acids were found to have high probability

pH Effect on IAPP-Insulin Interactions

of locating at protein binding interfaces according to the comprehensive screening of protein-protein complex database [175]. Considering the fact that the configurations of insulin-IAPP complex are heterogeneous and both components exist independently in solution, it is understandable that compared to hydrophobic residues hydrophilic residues are found on the binding interface to certain extent.

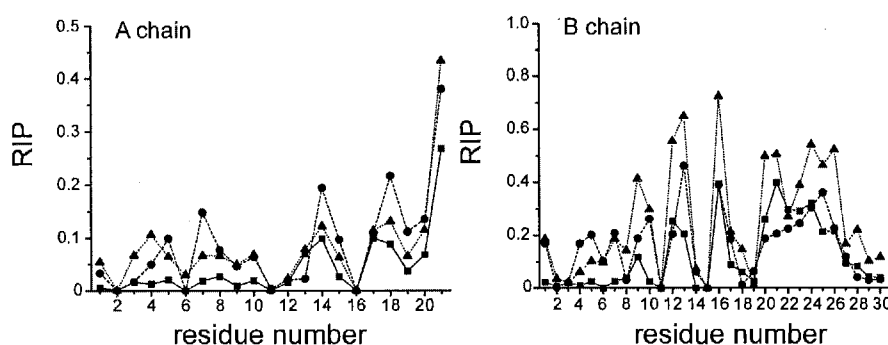


Figure 6.3 Residue interface propensity (RIP) of residues on insulin. A residue is counted as interface residue when any of its atoms is within a distance of no larger than 4Å with its binding partner. hIAPP(His+) is symbolized by squares, solid lines; hIAPP is shown in cycles and dashed lines; rIAPP is shown in triangles, dotted lines.

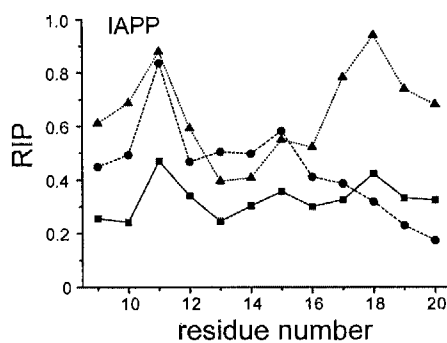


Figure 6.4 Residue interface propensity (RIP) of residues on IAPP segments. A residue is counted as interface residue when any of its atoms is within a distance of no larger than 4Å with its binding partner. hIAPP(His+) is symbolized by squares, solid lines; hIAPP is shown in cycles and dashed lines; rIAPP is shown in triangles, dotted lines.

pH Effect on IAPP-Insulin Interactions

We also detected several salt bridges and an amount of hydrogen bonds connecting the two interacting components, e.g., the charged R11 and R/H18 on IAPP have the highest RIP values (Figure 6.4), which indicates that the strong and enormous electrostatic interactions are a major contributor to the stability of the complex. Salt bridge is generally thought to be the strongest non-covalent interaction and renders additional restraints on distance and orientation between the two charged moieties. Therefore, not only stability but also specificity of insulin-IAPP recognition is enhanced by electrostatic interactions between side chains carrying opposite charges.

Aside from being polar amino acids, Tyr and His10 residues can form stable π -stacking interactions [176] by bringing aromatic side chains, benzene ring and imidazole ring, into close proximity. In the crystalline insulin dimer, aromatic residues Y16, F24, Y26 together with nonpolar V12 constitute a highly hydrophobic contact between the two monomeric B chains, rendering stability to insulin dimerization. The exact residues also show high occurrences on insulin-IAPP interface, suggesting a recognition mechanism that insulin binds to IAPP in an analogous mode through aromatic stacking and hydrophobic interactions. The significance of π -stacking in mediating insulin-IAPP complexation is also indicated by the high RIP value of F15 on IAPP which is ranked third after the two charged R11 and R/H18 in rIAPP and hIAPP(His⁺) systems and is ranked second after the neutral H18 in hIAPP system. Experimentally F15S and F15A substitutions were found to attenuate the inhibitory effect of insulin suggesting the critical role of F15 in insulin binding and inhibition behavior through aromatic stacking interactions [177].

pH Effect on IAPP-Insulin Interactions

The structural transition of full-length rIAPP during titration of insulin was studied using NMR by our collaborators. NMR chemical shifts indicate that the same region on rIAPP₁₁₋₁₈ is essential for interactions with insulin (Figure 6.5). When interacting with insulin, rIAPP shows the largest perturbations for R11, R18, and their surrounding residues, L12, A13, L16, and V17. The chemical shift result (Figure 6.5A) is strikingly consistent with our simulation result (Figure 6.4).

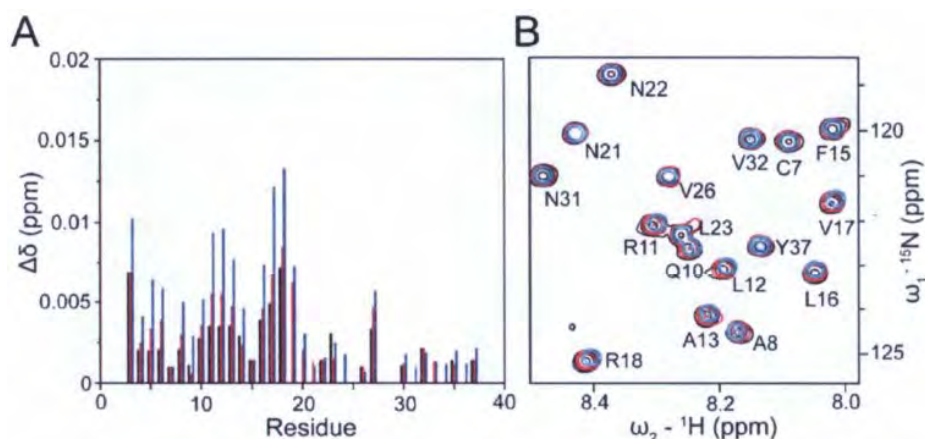


Figure 6.5 Chemical shift perturbations of rIAPP in the presence of insulin. A. Chemical shift perturbations ($\Delta\delta$ in ppm) of rIAPP in the presence of 0.5 mM, 1.0 mM, and 1.5 mM nonlabeled insulin (in black, red, and blue, respectively). The perturbations were calculated ($\Delta\delta = [(0.1\Delta\delta^N)^2 + (\Delta\delta^H)^2]^{1/2}$) for well-resolved peaks in the 2D [^1H , ^{15}N] HSQC spectra. The proline residues at positions 25, 28, and 29 were not included since prolines were not able to be detected by 2D [^1H , ^{15}N] HSQC. B. Overlaid 2D [^1H , ^{15}N] HSQC spectra of uniformly labeled ^{15}N rIAPP alone (in black) and upon binding to 0.5 mM (in red) and 1.5 mM (in blue) insulin. The figure was adapted from ref [104].

A structural ensemble of insulin-bound rIAPP₁₁₋₁₈ was modeled based on NMR data (Figure 6.6A). Residues with higher probability of interacting with insulin are shown in green, residues on medium interaction level are in gold, and the rest are in cyan. A representative structure of rIAPP₉₋₂₀-IAPP complex from the first 49 ns simulations is shown in Figure 6.6 B and colored in the same way as Figure 6.6 A (see caption). In the simulated model, rIAPP₉₋₂₀ takes a conformation with two short α -helical

pH Effect on IAPP-Insulin Interactions

segments corresponding to the same α -helical stretches found in NMR analysis [104]. Those residues (R11, L12, V17, and R18) with greater chemical shift during insulin titration are indeed in a proximity to the residues with greater chemical shift (magenta) on the helical region of the B chain.

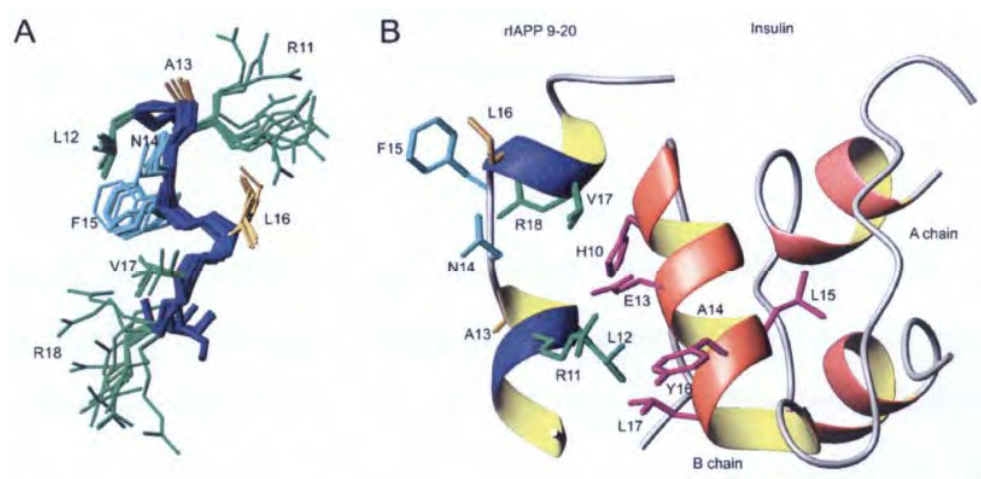


Figure 6.6 Residual structures of rIAPP₁₁₋₁₈ by NMR and rIAPP₉₋₂₀-insulin complex by REMD. A. Based on NMR data, a structural ensemble of rIAPP₁₁₋₁₈ was shown here are the best fit superimpositions of the backbones of all 20 structures (blue). The side chains are shown for residues with chemical shift perturbations (Figure 6.5) $\Delta\delta \geq 0.008$ ppm (green), $0.006 \text{ ppm} \leq \Delta\delta < 0.008 \text{ ppm}$ (gold), and the rest (cyan) upon insulin binding. B. Structural representation of the IAPP-insulin complex. Ribbon drawings illustrate the backbone of rIAPP₉₋₂₀ (blue) and the insulin A chain (light coral) and B chain (coral). Side chains of the residues involved in the interaction are illustrated according to their chemical shift perturbations for rIAPP (Figure 6.5) and insulin (magenta). The figure was adapted from ref [104].

6.4. Ensembles of Bound-IAPP at Three Binding Sites on Insulin

Extensive simulations of the three systems generated massive samples of IAPP-insulin complexes. A two-level clustering scheme was applied to divide the complex ensembles into groups based on the binding sites of both insulin and IAPP

pH Effect on IAPP-Insulin Interactions

conformation. The clustering scheme was described in details in section 6.1.2. The representative structures of the highly populated groups are superimposed and shown in Figure 6.7. Bound forms of hIAPP(His⁺) are relatively compact with a segment of helice mixed with coils. Comparatively, hIAPP at neutral pH is generally random coiled and wraps around insulin in an extended conformation. The SS composition of bound rIAPP has several features: coils in majority, a small portion of helices, and β -sheets formed with insulin C or N-terminus in the same binding mode as in insulin crystal.

Despite the structural heterogeneity of bound IAPP, three binding sites on insulin can be identified. The hot spots on insulin are located in the middle of the helical region and the C-terminal loop of B chain. The residue N21 of A chain is also classified into this binding site because of its spatial proximity to C-terminus of B chain. The second highly populated binding site is identified as the helices and N-terminus of B chain. The first 20 residues on A chain constitute the third binding site. It is found that hIAPP(His⁺) hardly bind at the second and third binding sites; both hIAPP and rIAPP at neutral pH could bind to these two binding sites, albeit less favorable than the first binding site. Consistent with RIP diagram (Figure 6.3), binding site 1 is the most favorable binding region for all three forms of IAPP.

pH Effect on IAPP-Insulin Interactions

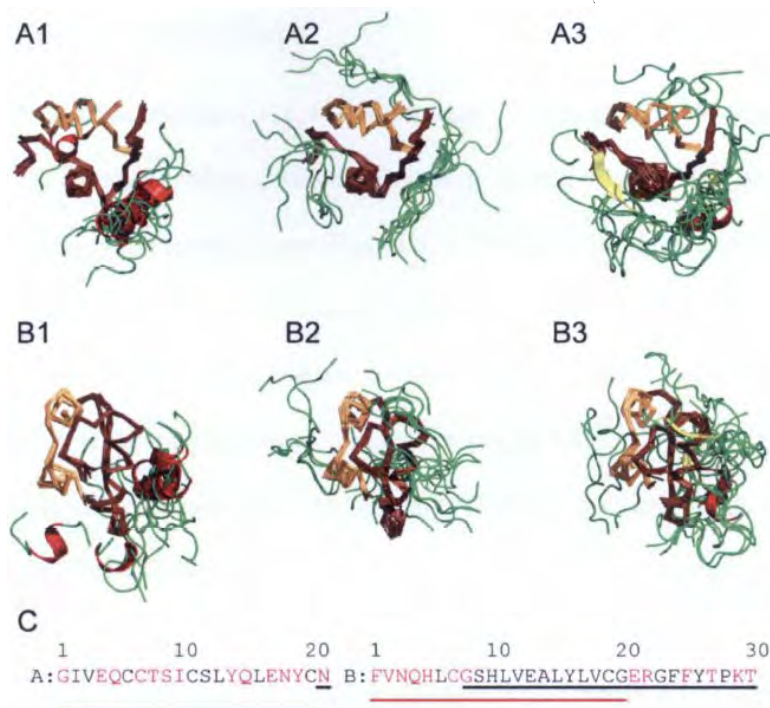


Figure 6.7 Representative structures displaying the multiple binding sites.

A1-A3, B1-B3. The filtering scheme of representative structures was specified in section 6.1.2. A chain (dark orange) and B chain (brown) of insulin are represented in ribbons and IAPP segments are shown in cartoon. Coloring of IAPP is based on secondary structure: coils in green, helices in red, and β -sheets in yellow. β -sheets here involve one strand from rIAPP and the other from insulin B chain. The structures are visualized from both top view (A1-A3) and side view (B1-B3). IAPP-insulin complexes from hIAPP(His⁺) (A1, B1), hIAPP (A2, B2) and rIAPP (A3, B3) systems are shown separately after superimposition. C. Three binding sites can be clearly seen in representative structures and are explicitly labeled in insulin primary sequence. Binding site 1 (black underline) consists of residues 8-30 on B chain and N21 on A chain C terminus; binding site 2 (red) spans from residue 1 to 20 on B chain with a overlapping region with site 1 at the helical region; binding site 3 (blue) consists of the rest of A chain excluding residue N21. Residues highlighted in red are those exposed to solvent in insulin crystal. The surface residues are selected when their solvent accessible surfaces are larger than 20 Å² in insulin hexamer.

6.5. Residual Contact Maps

The 1D RIP diagram (Figure 6.3, 6.4) demonstrates the engagement of each residue in forming the interfaces. More detailed information on pair-wise residue interactions is drawn in 2D residual contact maps (Figure 6.8). From the maps one can easily find that IAPP binding to insulin is of high specificity rather than in random nature. For hIAPP(His⁺)-insulin interaction, we can conclude from its contact map (Figure 6.8A) that recognition at the binding site 1 is led by charged R11 and H18 on IAPP through the formation of hydrogen bond to B chain Y16 or salt bridge to E21 and occasionally to E13 (Figure 6.9 A). The polar contacts with terminal carbonyl group and N21 of A chain are also present in the interfaces. Meanwhile, F15 (IAPP) associates with a small cluster of aromatic residues, F24, F25, and Y26 on B chain. The pattern of aromatic interactions is like a patch-patch hydrophobic association involving several flanking nonpolar residues, such as L12, A13, L16, and V17 on IAPP.

Likely, for r/hIAPP-insulin interaction, the presence of salt bridges of R11 on r/hIAPP and R18 on rIAPP formed with B chain E13 is clear from Figure 6.8 B and C. The representative structures indicating the interactions are shown in Figure 6.9 B and C. Other polar interactions and aromatic interactions at positions H5, S9, H10 on chain B also contribute to binding. The involvement of H5 and H10 on insulin brings out an explanation for the few contacts in this region for hIAPP(His⁺). The protonation state of H5 and H10 enhances electrostatic repulsive forces acting on the positively charged IAPP segment and thus perturbs hIAPP(His⁺) binding to insulin at binding site 2. IAPP occasionally binds to A chain, mainly through several polar

pH Effect on IAPP-Insulin Interactions

contacts involving residues such as Y14 and N18, albeit with a much lower affinity relative to that for B chain.

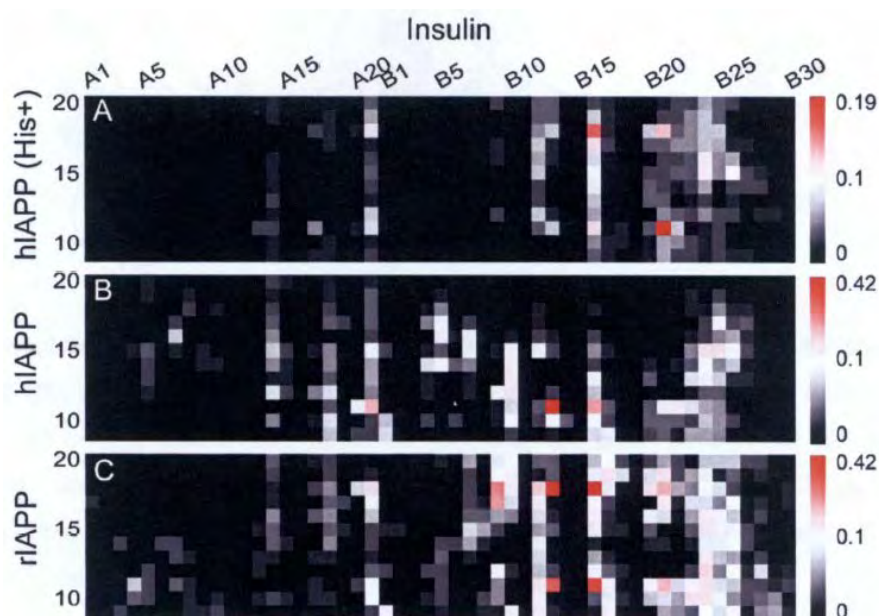


Figure 6.8 Residual contact maps for hIAPP(His⁺)-, hIAPP-, and rIAPP-insulin interactions. Contact maps are colored based on the occurrences of contact residue pairs derived from trajectories at 315 K. The color code is on the right side, labeled by the corresponding values of contact occurrences. To maximize the color saturation, a different upper limit for hIAPP(His⁺) is used, but the occurrence cutoff for the first gradient is the same, 0.1.

pH Effect on IAPP-Insulin Interactions

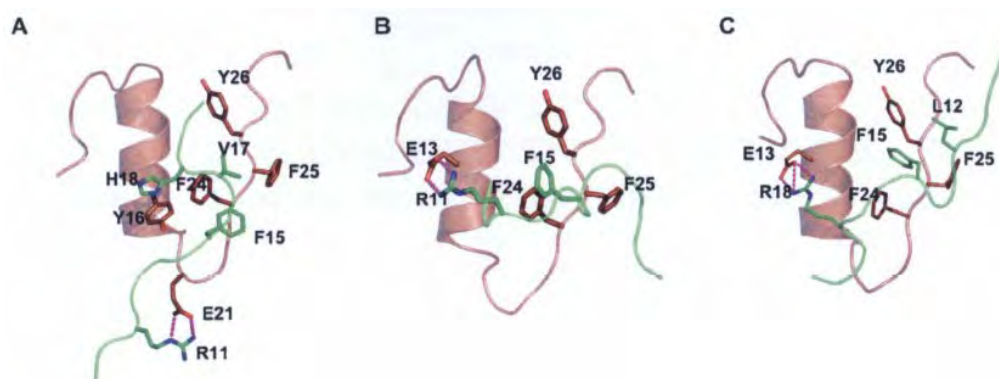


Figure 6.9 Salt-bridges and hydrophobic interactions formed between hIAPP(His⁺) (A), hIAPP (B), rIAPP (C) and insulin. In the selected representative structures, R11 on IAPP forms salt bridges with E13/21 on insulin B chain, and polar contacts are indicated by magenta, dashed lines. F15 and flanking hydrophobic residues (L12, V17; etc.) form hydrophobic interactions with an aromatic cluster (F24, F25, and Y26) on insulin B chain. Insulin A chain is hidden for clarity.

6.6. Characterization of IAPP-Insulin Interfaces

Several fundamental structural and energetic properties have been calculated to describe the characteristics of IAPP-insulin interfaces. The representative clusters of complexes (Figure 6.7) were selected to perform the characterization. Table 6.1 lists several basic quantities averaged over all filtered ensembles at the same binding site. These quantities include number of π -stacking, helix, interface area and interface hydrophobicity and related standard deviations.

pH Effect on IAPP-Insulin Interactions

Table 6.1 Structural and energetic analysis on IAPP-insulin complexes.

Simulation system	Binding site	helix		Hydrogen bond		pi-stacking		interface area ^e		interface hydrophobicity ^f		Binding energy (kJ/mol)	
hIAPP(His+)	1 ^a	0.5 ^g	0.50 ^d	3.3	1.88	0.8 ^h	0.75	2.25	0.909	0.50	0.173	-132.81	52.476
hIAPP	1	0.1	0.30	4.4	1.26	1.5	1.21	2.52	0.735	0.54	0.080	-157.60	24.646
	2 ^b	0.0	0.00	4.8	1.08	0.4	0.49	3.08	0.534	0.42	0.079	-157.12	14.952
	3 ^c	0.0	0.00	5.2	1.39	0.3	0.45	3.09	0.529	0.48	0.078	-142.81	18.043
rIAPP	1	0.2	0.39	5.4	1.43	1.1	0.65	3.11	0.590	0.51	0.084	-196.78	35.465
	2	0.0	0.00	8.2	1.17	0.4	0.68	3.49	0.413	0.50	0.047	-227.00	19.109
	3	0.4	0.48	6.3	1.47	0.3	0.53	3.15	0.589	0.40	0.056	-158.81	31.416

^aBinding site 1 is defined as IAPP binding to insulin B chain helix and C-terminal loop.^bBinding site 2 is defined as IAPP binding to insulin B chain helix and N-terminal loop.^cBinding site 3 is defined as IAPP binding to insulin A chain.^dThe second column of each field indicates the standard deviation of samples at one binding site.^eThe interface area was calculated as half of the sum of both insulin and IAPP buried area (Δ SASA) upon binding.^fInterface hydrophobicity was defined as the ratio of hydrophobic area to total interface area, Δ SASA.^gA helical structure is assigned to be 1, otherwise 0. Herein shows the average.^hThe average of total number of intermolecular pi-stacking interactions.

The interface hydrophobicity is defined as the ratio of the solvent accessible surface area (SASA) contributed by the hydrophobic residues to the total SASA. The interface hydrophobicity is around 0.50 suggesting that association of the two components is not exclusively driven by burying hydrophobic patches on surfaces. The interface area with a value of approximately 300 \AA^2 is only of a medium size [175]. However, the value of ratio of the number of hydrogen bonds (including salt bridges) to the interface area is relatively large which indicates that the abundant polar interactions make up the insufficient amount of residual contacts. The difference of the three binding sites is insignificant in terms of binding energy and

pH Effect on IAPP-Insulin Interactions

helix propensities. When the interface hydrophobicity is compared among the three binding sites, it is clearly seen that binding at site 1 involves more π -stacking interactions, fewer polar interactions and correspondingly the value of interface hydrophobicity is a little more than 0.5.

Based on our two-level clustering scheme, 13 clusters were identified for the hIAPP(His⁺)-insulin complexes. The characteristics of the binding interfaces from the 13 clusters have been quantified in Table 6.2. Without exception, these selected binding modes are stabilized by one or more salt bridges anchoring IAPP onto insulin. In general, decreased contacts (smaller interface area) reduce either polar or aromatic or both two types of interactions, and render the complex less stability (higher binding energy), such as in the cases of clusters 1-4.

Table 6.2 Breakdown of interface characteristics of hIAPP(His⁺)-insulin complex clusters.

cluster	helix	Hydrogen bond	pi-stacking	interface area	interface hydrophobicity index	Binding energy (kJ/mol)
1	0 ± 0 ^a	2 ± 0.5	1 ± 0.1	1.53 ± 0.310	0.38 ± 0.099	-102.68 ± 16.250
2	0 ± 0	2 ± 0.4	1 ± 0.1	1.52 ± 0.311	0.39 ± 0.105	-107.04 ± 11.982
3	1 ± 0.5	2 ± 0.7	1 ± 0.4	1.06 ± 0.473	0.24 ± 0.134	-66.77 ± 14.345
4	1 ± 0.3	3 ± 0.8	1 ± 0.5	1.40 ± 0.639	0.40 ± 0.162	-76.39 ± 23.117
5	0 ± 0	7 ± 0.9	0 ± 0	2.39 ± 0.370	0.48 ± 0.053	-151.04 ± 21.017
6	0 ± 0	6 ± 0.9	1 ± 0.6	3.14 ± 0.304	0.40 ± 0.052	-209.45 ± 19.330
7	1 ± 0.2	3 ± 1.0	2 ± 0.7	3.08 ± 0.332	0.59 ± 0.044	-168.61 ± 23.515
8	0 ± 0	4 ± 0.9	2 ± 0	3.41 ± 0.404	0.55 ± 0.041	-189.26 ± 16.678
9	0 ± 0.3	5 ± 0.8	2 ± 0.5	3.72 ± 0.445	0.50 ± 0.048	-221.80 ± 15.203
10	1 ± 0	2 ± 0.5	0 ± 0.2	2.09 ± 0.397	0.70 ± 0.063	-113.85 ± 17.022
11	1 ± 0	2 ± 0.6	0 ± 0.2	1.97 ± 0.465	0.71 ± 0.065	-109.21 ± 19.287
12	1 ± 0.2	1 ± 0.4	1 ± 0.3	1.84 ± 0.324	0.77 ± 0.056	-78.85 ± 16.178
13	0 ± 0.4	4 ± 0.5	0 ± 0.2	2.05 ± 0.484	0.40 ± 0.096	-131.57 ± 17.583

^aThe second column of each field indicates the standard deviation of samples at one binding site (100 snapshots per cluster).

pH Effect on IAPP-Insulin Interactions

Both ample hydrogen bonds and π -stacking interactions between bulky side chains from residues like Phe, Arg, and His are found to be capable of increasing the interface area and reducing the energy penalty of desolvation during molecular binding process. For instance, complexation in clusters 5 and 6 are relatively favorable due to the large amount of hydrogen bonds; in addition, in clusters 7-9, two or more π -stacking interactions allow formation of heterodimers of a high stability.

There are another three clusters 10-12 that have extremely hydrophobic interfaces with ~70% of contact area nonpolar, but without many polar or π -stacking interactions. Apart from the highly nonpolar interfaces, another common feature of these clusters is that hIAPP adopts helical conformations in bound states. Considering that insulin dimer is also packed by stacking two helices, we compared the hIAPP-insulin complex from the three clusters 10-12 with insulin crystal structure (Figure 6.10). The positions of three aromatic residues Y16, F24, Y26 and one nonpolar residue V12 on insulin dimer interface are replaced by S20 and three nonpolar residues L16, A18, and V17, correspondingly (Figure 6.10 A and B) in hIAPP(His⁺)-insulin complex. The packing and shape complementary of hIAPP(His⁺)-insulin complex is quite similar to those of insulin dimer (Figure 6.8 C and D).

pH Effect on IAPP-Insulin Interactions

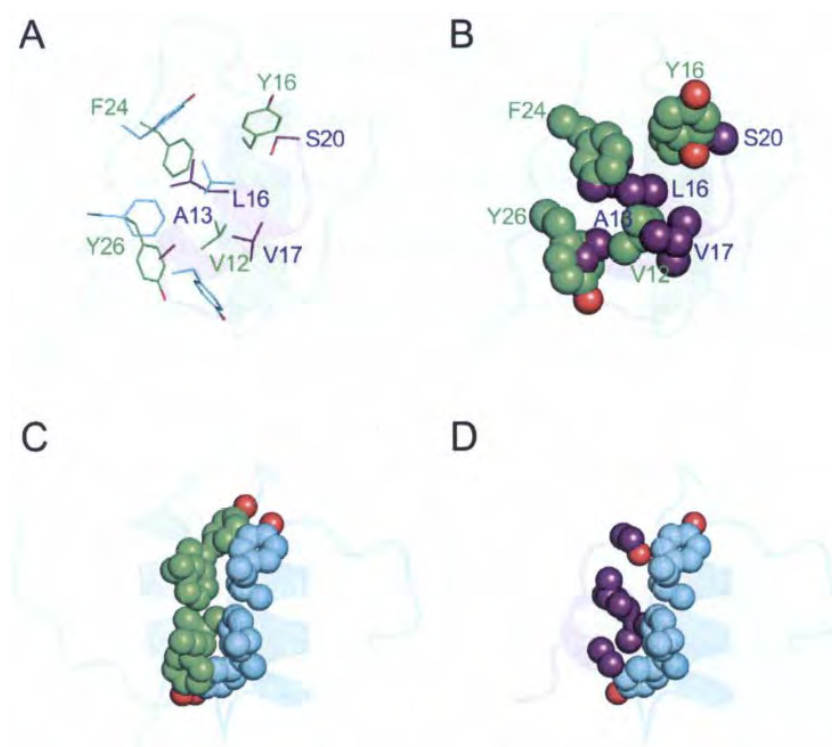


Figure 6.10 Hydrophobic residues on the interfaces of hIAPP(His⁺)-insulin heterocomplex and insulin dimer. hIAPP(His⁺) is colored in purple; one insulin is colored in green, another insulin is in cyan.

6.7. Summary

The three simulations reported here aim to systematically study the effects of varied pH on how IAPP recognizes and interacts with insulin. The N-terminal segment of IAPP shows an overwhelmingly high binding affinity for the middle helical region and its downstream extended loop on insulin B chain. The prediction of binding site agrees well with previous experiments. The interfaces are heterogeneous and moderately hydrophobic. Electrostatic interactions including salt bridges formed by R11 and H/R18 and a number of hydrogen bonds are crucial in IAPP-insulin

pH Effect on IAPP-Insulin Interactions

recognition. Abundance in aromatic interactions is another important feature of IAPP-insulin interfaces, which also contributes the majority of hydrophobic interactions. The two natural components, insulin and lipid membrane, co-existing with hIAPP *in vivo* present similarities in terms of IAPP recognition sites, critical residues, secondary structure, and pH dependence. Such knowledge may be utilized to design a competition-based inhibitor to interfere the toxic amyloidogenesis process of IAPP on the β -cell membrane.

7. Discussion

7.1. Aggregation Activity Modulated by Key Residues

The difference of five residues between hIAPP and rIAPP in the core region (residues 20-29) exerts evident effects on aggregation characteristics, among which three proline substitutions have the strongest influences. Proline is commonly found in turns exposed to solvent, which may benefit from its rigidity that costs less entropy penalty upon folding. The cyclic structure of side chain makes proline not compatible to any secondary structures, but it is occasionally found as the first residue of α helices and in the edge strands of β sheets to prevent protein self-assembly. In an atomic detailed level, we have studied how the special structural features of proline, including lacking of amide hydrogen atom and ϕ dihedral angle whose distribution does not overlap with β -structure, influence the aggregation ability of IAPP₂₀₋₂₉. The missing hydrogen atoms on proline backbones disrupt the hydrogen bond network and therefore the β -sheet stability is weakened. Besides, the rigid backbone of proline induces unfavorably high energy to β -conformation. The two reasons explain the loss of amyloid aggregation ability of rIAPP₂₀₋₂₉ brought by proline mutation. Comparatively, effects of the other two residue mutation (F23L and I26V) seem indifferent. Their SSP greatly resemble that of their counterparts on hIAPP and a certain amount of backbone hydrogen bonds formed by these two variant residues, indicating a less important function in abolishing rIAPP₂₀₋₂₉ aggregation.

Human IAPP₂₀₋₂₉ was thought to form a highly ordered hydrophobic core in fibrils. Nevertheless, recent studies by ssNMR [20] and X-ray [178] indicated a turn formed

Discussion

around residue G24 in mature fibrils derived from full-length hIAPP. Such secondary structure propensity most probably resorts to the combined features of small-sized G24 and aromatic ring of F23. A similarly conformational preference of the segment in membrane-mimicking environments was also found by solute state NMR [179] and MD simulation study [180]. We also found that the SSP of F23, G24, and A25 for bend and turn indeed is higher than that for β -structures. Moreover, a few hairpin monomers were also observed most likely as transient states. We found that the emergence of hairpin monomers can be reduced by lipid binding at this region. The small-sized side chains on G24 and A25 together with the nonpolar residue F23 comprise a perfect hydrophobic cavity for lipid tail to embed. The embedded lipid reduces the backbone flexibility of G24 and renders the segment in linear β -strands, which accounts for the increased propensities for β -structure of only residues 23, 24, and leaving SSP of other residues mainly unchanged in the presence of lipid molecule.

7.2. Insights into the Mechanism of Short Peptide Self-assembly

To summarize the aggregation process of hIAPP₂₀₋₂₉ tetramer, a sketch plot is shown in Figure 7.1. In the beginning, four dispersed monomers (state 1) rapidly collapse into a condensed but amorphous aggregate (state 2). The amorphous aggregate is characterized by small R_g and the lack of β -structures. Conformational reorganization within the aggregate converts two constituent monomers into a β -sheet dimer (state 3). The β -sheet dimer undergoes either of two paths to nucleation: following the first path, the dimer continues to grow into a trimer (state 4) by adding the third monomer (grey dashed line) through internal reorganization; following the second path, the third monomer dissociates from the aggregate (state 4') and then re-

Discussion

associates to elongate the dimer into a trimer (state 5'). Either of the processes iterates or alternates until the nucleus of a critical size forms. According to the nucleated growth mechanism [43, 181], the nucleation process is slow because it is energetically unfavorable before the critical nucleus forms. Therefore, the partially structured β -sheet oligomers (dimer, trimers, etc.) are prone to dissociate partially or completely (3 to 4' or 3 back to 1). However, binding to lipid stabilizes the intermediate states in the first path by preventing dissociation of the low-level aggregates. Thereby the growth of the aggregates is accelerated.

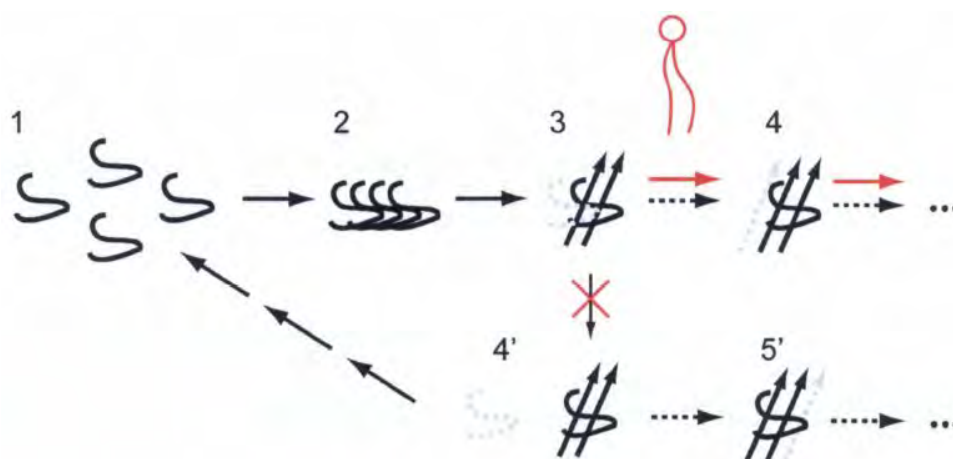


Figure 7.1 Nucleation process through two paths one of which is accelerated by lipid molecules. Dispersed monomers (state 1) rapidly collapse into a condensed but amorphous aggregate (state 2). Internal reorganization of the aggregates converts two constituent monomers into a β -sheet dimer (state 3). Following the first path to nucleation, the dimer continues to grow into a trimer (state 4) by adding the third monomer (grey dashed line) through internal reorganization. The process iterates until the nucleus of a critical size forms. Following the second path, the third monomer dissociates from the aggregate (state 4') and re-associates from the other side to elongate the dimer into trimer (state 5'). But more likely, the aggregate dissociates into a lower-level aggregate (4' back to 1). Binding to lipid stabilizes the intermediate states in the first path by preventing dissociation of the low-level aggregates. Solid arrows indicate processes that are energetically favorable and dashed arrows indicate those energetically unfavorable.

Discussion

A “reptation” mechanism was used to explain the growth of oligomers through the internal conformational reorganization as in the first path. Without disassembly of aggregates, reptation occurs only between neighboring strands within the oligomers and the natural registry (hydrogen bonding patterns) between strands is achieved by breaking the unnatural registry hydrogen bonds initially formed. Petty *et al.* provided the first experimental evidence for this phenomenon and further developed the reptation mechanism by suggesting two distinct mechanisms at high and low peptide concentrations respectively. Reptation only dominates at high concentrations; at low concentrations, repeated detachment and annealing of aggregated strands helped realign the strands. Unlike reptation mechanism, peptides at low concentration can dissociate from pre-nucleus into solution, while soluble monomers can associate with the aggregates to take part in the formation of nuclei.

7.3. Resveratrol Redistributes Oligomer Species

There are quite a few interesting experimental studies on the mechanism of inhibiting fibril formation of IAPP and A β proteins by resveratrol [102, 108, 155, 182]. When resveratrol was added, the usual fibrillation pathway was diverted to an off-pathway product, spherical amorphous oligomers with random coils as the dominant secondary structure. More importantly such spherical structures were not cytotoxic [102]. The link between cytotoxicity and IAPP fibril formation could be multifactorial, e.g., the incorporation of lipid when IAPP fibril grows on the membrane [155, 183], or the hydrophobic exposure on the fibrillar intermediates in which the hydrophobic interactions correlated with ordered structures play a major role [184].

Discussion

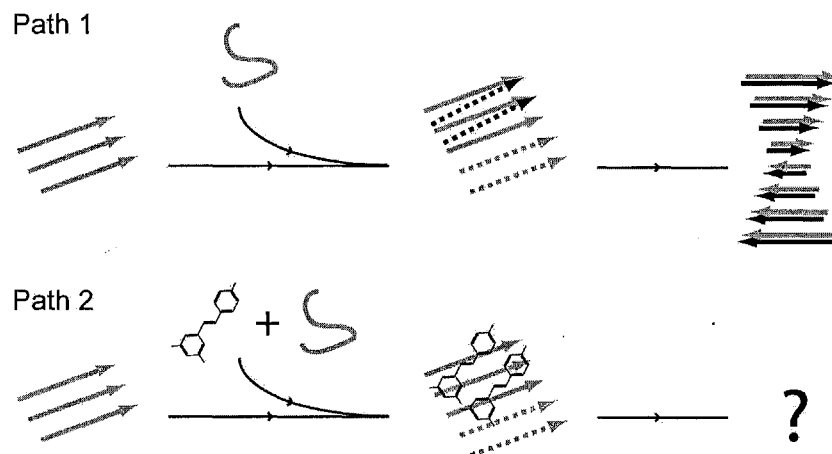


Figure 7.2 Self-assembly of amyloidogenic peptides and suggested inhibitory mechanism of resveratrol. When monomers attempt to integrate into a fibril nucleus, aggregates grow in two directions, lateral association and longitudinal elongation (path 1). The end product is a multiple-layered fibril. When peptides are incubated with resveratrol, resveratrol is capable of blocking the lateral growth, while longitudinal elongation nearly remains intact (path 2). Black and grey colors are used to distinguish β -strands belonging from different layers. Dashed arrows represent the nascent β -strands in oligomers.

In our simulations the presence of resveratrol caused the redistribution of oligomer species. One of the prominent features was that the ordered hydrophobic matched patterns which were demonstrated in the double-layered oligomer species were greatly diminished. We proposed the following putative inhibitory mechanism based on the results of our simulations (Figure 7.2). In a path leading to the native end product (path 1), aggregates grow both laterally and longitudinally driven by hydrophobic matching of the side chains as well as hydrogen bonds on the backbone. When the path is interfered by resveratrol (path 2), the aggregates only grow in the longitudinal direction. Based on our results, there was no hint about whether such single-layered β -sheet can continue to grow into a single-layered fibril or the intermediate species are just too fragile to grow further. It was found that there was no sign of typical fibrils formed when full length hIAPP was incubated with

Discussion

resveratrol *in vitro* [102, 155]. Such observations seem consistent with available protofibril structure models [20, 167, 185-188], in which inter-sheet side chains are interdigitated in a steric zipper to stabilize the fibril structures. Thus, if resveratrol acts on the full length hIAPP in the same mechanism as on hIAPP₂₂₋₂₇, it appears that inhibiting lateral growth is active enough to fully abolish fibril formation.

A large number of small molecules belonging to several chemical families have been studied for their anti-aggregation and anti-cytotoxicity efficacies by experiments [20, 55, 100, 107, 189-191]. The observation that these compounds bind to heterogeneous intermediate species (monomers, oligomers, and protofibrils) indicated the complexity of their functional mechanisms [55, 100]. Molecular dynamics simulations, on the other hand, have helped pinpoint the interactions between inhibitors and aggregates and brought out more details on the molecular level. Unlike resveratrol, other kinds of small molecules were found to primarily bind to the elongation edges of protofibrils. The underlying inhibition mechanism was suggested to lie in the ability of the inhibitors to interfere with the “dock-lock” stage during fibril elongation process [114, 115]. On the elongation edges where free peptides can be adsorbed, backbone polar groups, such as amide and carbonyl groups, are exposed. Through contacts with backbones, polar moieties on inhibitors substantially contribute to the compound-protofibril contacts. Two functional moieties that all inhibitors share in common are aromatic rings and polar substituent groups on the rings [107]. Besides resveratrol, other compounds studied all contain moieties of high polarity (such as carboxyl group) [113]. We hypothesized that for an inhibitor, in addition to its structural scaffold, the interplay of aromaticity and polarity is another critical determinant for its mode of action. The hypothesis gives an

Discussion

explanation on the origin of different binding preferences for the lateral or longitudinal sides and implies that the efficacy of inhibitors also relies on the amino acid composition of the peptide. High polarity may increase the probability for compounds to bind to the elongation edges, but suffer high desolvation penalty upon binding [111]. Optimization of the balance between polarity and aromaticity of small molecule inhibitors can be beneficial in de novo design of potent anti-amyloid drugs.

7.4. Insulin and Membrane Compete for Binding to hIAPP

Within the β -cells, soluble hIAPP molecules exist in between the crystalline insulin and lipid membranes, thus the peptide makes contacts with its natural inhibitor and enhancer of amyloidogenesis at the same time [192]. The amyloidogenesis inhibitory effect of insulin interaction has been confirmed either in the absence or presence of lipid membranes [192]. Combined our study with others' work, three common features of membrane and insulin bound IAPP are summarized as (1) N-terminus of IAPP excluding the first seven residues with one disulfide bond is responsible for initiating binding [193, 194]; (2) the protonation state of H18 modulates the interaction as an anchoring point [193]; (3) N-terminus adopts a transient helical structure upon binding which is divergent from β -sheet rich mature amyloid fibrils [74, 152].

We have studied the interactions between insulin and IAPP₉₋₂₀ and characterized the interfaces of their complexes at both neutral and acidic pH. The N terminal segment with the disulfide bond region truncated has been identified to be responsible for binding to insulin [104, 174]. According to our simulations, the segment showed a pronounced preference for binding to monomeric insulin mainly at two spatially

Discussion

close regions on B chain in the tertiary structure, which we referred to as binding site

1. Strong interactions between the two regions of insulin and N terminus of IAPP have previously been observed by Gilead *et al.* [174]. Because of the importance of the segment in membrane association, it has been subjected to many experiments in the aim of understanding toxicity of IAPP. Segment 1-19 of IAPP disrupted both synthetic anionic membranes and β -cells under physiological conditions, whereas C-terminus embracing residues 20-29 which assumed to form the hydrophobic core of higher level aggregates was largely free in solution in a less structured manner [193]. IAPP₁₋₁₉ was induced to be transiently helical when IAPP associated with membrane and α -helix was thought to be an intermediate state of hIAPP on pathway towards fibrillization [152, 194, 195]. In contrast, C terminus (IAPP₂₀₋₃₇) functioned differently to trigger the aggregation process which benefited from its hydrophobicity and mobility in aqueous environment [195]. Considering that the exact segment mediated insulin binding, an inhibitory mechanism that insulin acted as a competitor against membrane to keep a balance between adsorption and release of IAPP without amyloid conversion was suggested. Meanwhile, due to the weak intermolecular interaction, insulin was not a powerful competitor; Knight *et al.* found that 10 times or higher concentration of insulin was required to reach a comparable inhibitory level in the presence of DOPG than that in the absence of membrane [192]. They also unveiled that rIAPP relocated insulin crystal to anionic membranes physically, indicating the ability of rIAPP to bind to the two components simultaneously. The crucial effect of membrane was to enhance the two dimensional crowding of IAPP on the membrane surface. The tri-particle interaction between IAPP, insulin and membrane may reduce the concentration of IAPP on the

Discussion

membrane and consequently the enrichment effect rather than membrane interaction was blocked in the insulin induced amyloidogenesis inhibitory process.

hIAPP has only two positively charged residues at extracellular pH=7.0 and three at intracellular pH=6.0. However, the abilities of membranes to catalyze hIAPP aggregation and the consequential membrane damages were obviously dependent on the compositions of neutral and negatively charged lipids [195]. The highly anionic membrane had the most pronounced effect on accelerating hIAPP aggregation and even the nonamyloidogenic rIAPP can be cytotoxic when the membrane was purely consisted of negatively charged lipids [195]. It appeared that besides crowding effects brought by membrane surface, attractive electrostatic interactions played critical roles in modulating hIAPP-membrane interactions. Among all three charged residues of hIAPP, residue H18 especially attracted interest because it is pH sensitive within the pH range of the intracellular and extracellular environments of β -cells. The residue was found to be capable of reducing the assembly rate when it was protonated [196]. Protonation of H18 reoriented the peptide to the surface of membrane from transmembrane orientation of its neutral alternative and thus reduced the disrupting effect of hIAPP₁₋₁₉ at pH 6.0 [152]. We have shown that protonated form of H18 exhibited a higher tendency for insulin binding and it seemed that charged residue His or Arg at position 18 induced more helix than neutral His.

The transient existence of helical structure has been widely detected, albeit how the converting of α -helical peptides to β -sheet rich fibrils takes place on the membrane remains unclear. Insulin is also capable of inducing helical structure on IAPP. Previous NMR study has identified a helix-like conformation when rIAPP bound to

Discussion

insulin [104]. The helical complexation of IAPP-insulin was suggested in the same manner as hIAPP helical dimerization recently [177]. Role of insulin in disrupting aggregation was deduced that it blocks the interface of IAPP dimerization which was on the pathway to fibrillization. We also reported a two-helix-stacking binding mode during hIAPP(His⁺)-insulin complexation. Charged long side chain of Arg has been found to be capable of stabilizing helix by shielding backbone hydrogen bonds and also forming polar contact with the fourth residue upstream [197]. We believed that charged R/H18 acted in such manner to maintain helical structure and accounted for the high propensity for ordered structures.

However, the helix based inhibitory mechanism cannot be exclusive, considering the low sampling of α -helix (~10%) in REMD simulations and 10%-20% helical composition estimated in the NMR study [198]. We have shown that the conformations of insulin-bound IAPP were quite heterogeneous in terms of binding sites and modes, and these complexes with IAPP in coiled structures were of the equal stability to helix-based complexes. We believed that the conformation similarity between membrane-bound and insulin-bound IAPP was probably insignificant. The fact that insulin competed to bind to the same sequence segment of hIAPP as membranes may be the key to prohibition of amyloidogenesis and helix-based inhibitory mechanism could be oversimplified.

8. Conclusion

Over the past decades, the understanding of amyloidogenesis and the related pathology has been significantly deepened. Several revised nucleation growth mechanisms have been introduced to elaborate the sigmoidal growth pattern of aggregation. High resolution structures and dynamics of mature fibrils under certain conditions were obtained. Pathologically important intermediate oligomers have been captured and purified to study their aggregation ability and toxicity. Amyloidogenic proteins were also found to interact with other biomolecules such as membranes and other proteins, as well as small molecules including organic compounds and ions. The interplay between amyloidogenic proteins and cellular membranes has been associated with amyloidogenesis induced cell apoptosis. The interactions with low molecular weight protein/peptidomimetics and small molecules were drawn special attention due to the inhibitory activities of these interacting partners. However, more insights are still needed into this active field. More details are needed to resolve the overall aggregation process, especially the nucleation stage which is featured by the complexity of intermediate species and the pathological significance. High resolution depiction of interactions between amyloidogenic protein and other entities with biological importance (such as toxicity, catalysis, and inhibition of amyloid aggregation) will be of great value to understand its pathology and also to develop potent anti-aggregation drugs. On the basis of the up-to-date knowledge, the current studies using molecular dynamics simulations have provided complementary and more detailed interaction pictures of amyloidogenesis related phenomena.

Conclusion

We chose one of the amyloidogenic peptides, IAPP, as the study object. Three segments of IAPP were studied on their aggregation behaviors, rIAPP₂₀₋₂₉, hIAPP₂₀₋₂₉, and hIAPP₂₂₋₂₇. rIAPP₂₀₋₂₉ was known to be nonamyloidogenic, whose segments only formed amorphous aggregates in our simulation. Segment hIAPP₂₀₋₂₉ was capable of aggregating into partially structured β -sheet oligomers. The conformational reorganization of rapidly formed, amorphous aggregates into competent nucleus followed two pathways. The reptation mechanism which converts unstructured peptides into β -strands without detachment from the amorphous aggregate is essential at a high peptide concentration. When we increased the system size from tetramer to heptamer, new insight came out from what happened in the early stage of nucleation. The early aggregates of segment hIAPP₂₂₋₂₇ were found to adopt a double-layered β -sheet arrangement, which was known as the steric zipper formed by side chains in microcrystals and fibrils. The stacking interactions of side chains occurred in the very early stage, and the blockage of the stacking was capable of abolishing fibrillization. The finding indicated that the specific side chain contacts guided the molecular recognition during peptide self-assembly, which explained why the aggregation activities were divergent among proteins with different primary sequences.

We also studied the interactions of IAPP with both its aggregation catalyst (DOPC) and inhibitor (resveratrol). In a thermodynamic view, DOPC increased the thermal stability of low-level β -sheet oligomers and prevented them from dissociation; whereas resveratrol made them more soluble at high temperatures. Lipid and resveratrol molecules are all amphiphilic and their nonpolar groups mainly conduct the interactions with peptide aggregates. Lipid bound at the hydrophobic patches on

Conclusion

peptide oligomers. Accelerating aggregation by lipid molecules originated from lowering the probability of dissociation of the transient small β -sheet oligomers so that the reaction was pushed towards increasing the oligomer size. In contrast, resveratrol competed with inter-sheet side chains for stacking on the surfaces of the single-layered β -sheet. A large amount of contacts between hydrophobic residues and nonpolar groups of resveratrol was greatly engaged in forming resveratrol-peptide interfaces, indicating the nature of binding between two entities was still hydrophobic interactions. In this circumstance, the normal double-layered arrangement for early species was missing and the single-layered β -sheet oligomer was incapable of growing into fibrils.

Insulin co-exists with hIAPP *in vivo* and was regarded as a protein inhibitor of hIAPP aggregation even in the presence of membranes. Thereby we set up a system of the insulin-IAPP₉₋₂₀ complex and attempted to pinpoint the interaction interfaces whose information can help rationalize the development of protein inhibitors. The simulations identified the exact binding regions on insulin and IAPP in line with experiments. The interfaces of the heterogeneous complex were characterized by the abundance in polar interactions (salt-bridges and hydrogen bonds) as well as aromatic interactions. The area of interfaces was quite small and flat, which made the binding affinity very low. When the pH effect was taken into account helical structures of protonated hIAPP were evidently reserved from unbound state in solution and binding on insulin became more concentrated on B chain. The resemblance between IAPP-insulin and IAPP-membrane interactions came to our notice. IAPP binding to the two components of β -cells shared common features, such as the same pH effect, the charged state in residue 18, the transient helical structures

Conclusion

at acidic pH, the involvement of N-terminus, etc. Consequently we concluded that the competition between insulin and membrane for binding to IAPP in the same sequence and in the same manner eliminated the enrichment effect on membrane and retained the soluble state of hIAPP.

For the future work, the mechanisms and conclusions we drew here need more refinement. Take the “reptation” mechanism for instance. With only four peptides, no effects for low and high peptide concentrations can be seen. A coarse graining level of peptide models should be used and the system size, thereby, can be enlarged. As to the enhancement effect on aggregation by membranes, a micellar and bilayer lipid phase might act better than a single lipid, which absolutely requires coarse graining our molecular models. Several essential factors which are attributed to the inhibitory effects of resveratrol and insulin have been identified. Combined with the principles of designing organic and protein drugs, novel small molecule and peptide inhibitors can be discovered. Similar simulation schemes can be performed on the new systems and enhanced inhibitory effects are expected optimistically. Previous experimental studies have demonstrated that changing the ionic strength of the solvent has a great impact on the aggregation mechanism leading to distinct fibril morphologies. Given the diverse kinds of ions in β cells, it would be interesting to study the impacts of different ion types and strength on the structure and dynamics of the amyloid fibrils.

References

References

1. Levinthal, C., *Are there pathways for protein folding?* J. Chim. Phys., 1968. **65**: p. 44-45.
2. Schiene, C. and G. Fischer, *Enzymes that catalyse the restructuring of proteins*. Current Opinion in Structural Biology, 2000. **10**(1): p. 40-45.
3. Hammond, C. and A. Helenius, *Quality-Control in the Secretory Pathway*. Current Opinion in Cell Biology, 1995. **7**(4): p. 523-529.
4. Haataja, L., et al., *Islet Amyloid in Type 2 Diabetes, and the Toxic Oligomer Hypothesis*. Endocr Rev, 2008: p. er.2007-0037.
5. Schubert, U., et al., *Rapid degradation of a large fraction of newly synthesized proteins by proteasomes*. Nature, 2000. **404**(6779): p. 770-774.
6. Kopito, R.R. and D. Ron, *Conformational disease*. Nat Cell Biol, 2000. **2**(11): p. E207-E209.
7. Luheshi, L.M., D.C. Crowther, and C.M. Dobson, *Protein misfolding and disease: from the test tube to the organism*. Current Opinion in Chemical Biology, 2008. **12**(1): p. 25-31.
8. Goldberg, M.S. and Lansbury P.T, Jr., *Is there a cause-and-effect relationship between alpha-synuclein fibrillization and Parkinson's disease?* Nature Cell Biology, 2000. **2**(7).
9. Bucciantini, M., et al., *Inherent toxicity of aggregates implies a common mechanism for protein misfolding diseases*. Nature, 2002. **416**(6880): p. 507-511.
10. Caughey, B. and P.T. Lansbury, *PROTOFIBRILS, PORES, FIBRILS, AND NEURODEGENERATION: Separating the Responsible Protein Aggregates from The Innocent Bystanders*. Annual Review of Neuroscience, 2003. **26**(1): p. 267-298.
11. Dobson, C.M., *Protein folding and misfolding*. Nature, 2003. **426**(6968): p. 884-890.
12. Dobson, C.M., *Protein misfolding, evolution and disease*. Trends in Biochemical Sciences, 1999. **24**(9): p. 329-332.
13. Fandrich, M., M.A. Fletcher, and C.M. Dobson, *Amyloid fibrils from muscle myoglobin*. Nature, 2001. **410**(6825): p. 165-166.
14. LeBrasseur, N., *Polyamino acids take amyloid form*. J. Cell Biol., 2002. **159**(4): p. 538-a-539.
15. Chiti, F. and C.M. Dobson, *Protein misfolding, functional amyloid, and human disease*. Annual Review of Biochemistry, 2006. **75**: p. 333-366.
16. Jimenez, J.L., et al., *The protofilament structure of insulin amyloid fibrils*. Proc Natl Acad Sci U S A, 2002. **99**(14): p. 9196-201.
17. Opie, E.L., *THE RELATION OF DIABETES MELLITUS TO LESIONS OF THE PANCREAS. HYALINE DEGENERATION OF THE ISLANDS OF LANGERHANS*. J. Exp. Med., 1901. **5**(5): p. 527-540.
18. Westermark, P. and E. Wilander, *The influence of amyloid deposits on the islet volume in maturity onset diabetes mellitus*. Diabetologia, 1978. **15**(5): p. 417-421.
19. Goldsburly, C., et al., *Amyloid Fibril Formation from Full-Length and Fragments of Amylin*. Journal of Structural Biology, 2000. **130**(2-3): p. 352-362.

References

20. Luca, S., et al., *Peptide Conformation and Supramolecular Organization in Amylin Fibrils: Constraints from Solid-State NMR*. Biochemistry, 2007. **46**(47): p. 13505-13522.
21. Wiltzius, J.J.W., et al., *Atomic structure of the cross- β spine of islet amyloid polypeptide (amylin)*. Protein Sci, 2008. **17**(9): p. 1467-1474.
22. Goldsbury, C.S., et al., *Polymorphic fibrillar assembly of human amylin*. J Struct Biol, 1997. **119**(1): p. 17-27.
23. Schmidt, M., et al., *Comparison of Alzheimer Abeta(1-40) and Abeta(1-42) amyloid fibrils reveals similar protofilament structures*. Proceedings of the National Academy of Sciences, 2009. **106**(47): p. 19813-19818.
24. Van Melckebeke, H., et al., *Atomic-resolution three-dimensional structure of HET-s(218-289) amyloid fibrils by solid-state NMR spectroscopy*. J Am Chem Soc. **132**(39): p. 13765-75.
25. Ferguson, N., et al., *General structural motifs of amyloid protofilaments*. Proc Natl Acad Sci U S A, 2006. **103**(44): p. 16248-53.
26. Palotay, J.L. and C.F. Howard, Jr., *Insular amyloidosis in spontaneously diabetic nonhuman primates*. Vet Pathol Suppl, 1982. **7**: p. 181-92.
27. Johnson, K.H. and J.B. Stevens, *Light and electron microscopic studies of islet amyloid in diabetic cats*. Diabetes, 1973. **22**(2): p. 81-90.
28. Hubbard, G.B., et al., *Spontaneous pancreatic islet amyloidosis in 40 baboons*. Journal of Medical Primatology, 2002. **31**(2): p. 84-90.
29. Glenner, G.G., E.D. Eanes, and C.A. Wiley, *Amyloid Fibrils Formed from a Segment of the Pancreatic-Islet Amyloid Protein*. Biochemical and Biophysical Research Communications, 1988. **155**(2): p. 608-614.
30. Westermark, P., et al., *Islet Amyloid Polypeptide - Pinpointing Amino-Acid-Residues Linked to Amyloid Fibril Formation*. Proceedings of the National Academy of Sciences of the United States of America, 1990. **87**(13): p. 5036-5040.
31. Betsholtz, C., et al., *Islet Amyloid Polypeptide (Iapp) - Cdna Cloning and Identification of an Amyloidogenic Region Associated with the Species-Specific Occurrence of Age-Related Diabetes-Mellitus*. Experimental Cell Research, 1989. **183**(2): p. 484-493.
32. Porat, Y., et al., *Inhibition of islet amyloid polypeptide fibril formation: a potential role for heteroaromatic interactions*. Biochemistry, 2004. **43**(45): p. 14454-62.
33. Scrocchi, L.A., et al., *Design of peptide-based inhibitors of human islet amyloid polypeptide fibrillogenesis*. J Mol Biol, 2002. **318**(3): p. 697-706.
34. Abedini, A., F. Meng, and D.P. Raleigh, *A Single-Point Mutation Converts the Highly Amyloidogenic Human Islet Amyloid Polypeptide into a Potent Fibrillization Inhibitor*. J. Am. Chem. Soc., 2007. **129**(37): p. 11300-11301.
35. Tracz, S.M., et al., *Role of aromatic interactions in amyloid formation by peptides derived from human Amylin*. Biochemistry, 2004. **43**(50): p. 15901-8.
36. Wu, C., H. Lei, and Y. Duan, *The role of Phe in the formation of well-ordered oligomers of amyloidogenic hexapeptide (NFGAIL) observed in molecular dynamics simulations with explicit solvent*. Biophys J, 2005. **88**(4): p. 2897-906.
37. Marek, P., et al., *Aromatic Interactions Are Not Required for Amyloid Fibril Formation by Islet Amyloid Polypeptide but Do Influence the Rate of Fibril Formation and Fibril Morphology*. Biochemistry, 2007. **46**(11): p. 3255-3261.

References

38. Green, J., et al., *Full-length rat amylin forms fibrils following substitution of single residues from human amylin*. J Mol Biol, 2003. **326**(4): p. 1147-56.
39. Sakagashira, S., et al., *Missense mutation of amylin gene (S20G) in Japanese NIDDM patients*. Diabetes, 1996. **45**(9): p. 1279-81.
40. Lee, S.C., et al., *The islet amyloid polypeptide (amylin) gene S20G mutation in Chinese subjects: evidence for associations with type 2 diabetes and cholesterol levels*. Clin Endocrinol (Oxf), 2001. **54**(4): p. 541-6.
41. Petty, S.A. and S.M. Decatur, *Experimental Evidence for the Reorganization of beta-strands within aggregates of the Abeta(16-22) Peptide*. J. Am. Chem. Soc., 2005. **127**(39): p. 13488-13489.
42. Plakoutsi, G., et al., *Evidence for a Mechanism of Amyloid Formation Involving Molecular Reorganisation within Native-like Precursor Aggregates*. Journal of Molecular Biology, 2005. **351**(4): p. 910-922.
43. Serio, T.R., et al., *Nucleated Conformational Conversion and the Replication of Conformational Information by a Prion Determinant*. Science, 2000. **289**(5483): p. 1317-1321.
44. Shen, C.L., et al., *Light scattering analysis of fibril growth from the amino-terminal fragment beta(1-28) of beta-amyloid peptide*. Biophysical Journal, 1993. **65**(6): p. 2383-2395.
45. Carulla, N., et al., *Molecular recycling within amyloid fibrils*. Nature, 2005. **436**(7050): p. 554-8.
46. Murphy, R.M., *Kinetics of amyloid formation and membrane interaction with amyloidogenic proteins*. Biochimica Et Biophysica Acta-Biomembranes, 2007. **1768**(8): p. 1923-1934.
47. Ono, K., M.M. Condon, and D.B. Teplow, *Structure-neurotoxicity relationships of amyloid beta-protein oligomers*. Proceedings of the National Academy of Sciences of the United States of America, 2009. **106**(35): p. 14745-14750.
48. Sandberg, A., et al., *Stabilization of neurotoxic Alzheimer amyloid-beta oligomers by protein engineering*. Proc Natl Acad Sci U S A, 2010. **107**(35): p. 15595-600.
49. Bernstein, S.L., et al., *Amyloid-beta protein oligomerization and the importance of tetramers and dodecamers in the aetiology of Alzheimer's disease*. Nature Chemistry, 2009. **1**(4): p. 326-331.
50. Fawzi, N.L., et al., *Kinetics of Amyloid beta Monomer-to-Oligomer Exchange by NMR Relaxation*. Journal of the American Chemical Society, 2010. **132**(29): p. 9948-9951.
51. Milojevic, J., et al., *Understanding the molecular basis for the inhibition of the Alzheimer's Abeta-peptide oligomerization by human serum albumin using saturation transfer difference and off-resonance relaxation NMR spectroscopy*. J Am Chem Soc, 2007. **129**(14): p. 4282-90.
52. Milojevic, J., A. Raditsis, and G. Melacini, *Human serum albumin inhibits Abeta fibrillization through a "monomer-competitor" mechanism*. Biophys J, 2009. **97**(9): p. 2585-94.
53. Kaye, R., C.G. Glabe, and W. Indu Kheterpal and Ronald, *Conformation-Dependent Anti-Amyloid Oligomer Antibodies*, in *Methods in Enzymology* 2006, Academic Press. p. 326-344.
54. Kaye, R., et al., *Common structure of soluble amyloid oligomers implies common mechanism of pathogenesis*. Science, 2003. **300**(5618): p. 486-489.

References

55. Necula, M., et al., *Small Molecule Inhibitors of Aggregation Indicate That Amyloid beta Oligomerization and Fibrillization Pathways Are Independent and Distinct*. J. Biol. Chem., 2007. **282**(14): p. 10311-10324.
56. Ross, C.A. and M.A. Poirier, *Opinion: What is the role of protein aggregation in neurodegeneration?* Nat Rev Mol Cell Biol, 2005. **6**(11): p. 891-8.
57. Santini, S., N. Mousseau, and P. Derreumaux, *In silico assembly of Alzheimer's Abeta16-22 peptide into beta-sheets*. J Am Chem Soc, 2004. **126**(37): p. 11509-16.
58. Urbanc, B., et al., *In silico study of amyloid β -protein folding and oligomerization*. Proceedings of the National Academy of Sciences of the United States of America, 2004. **101**(50): p. 17345-17350.
59. Nguyen, H.D. and C.K. Hall, *Molecular dynamics simulations of spontaneous fibril formation by random-coil peptides*. Proceedings of the National Academy of Sciences of the United States of America, 2004. **101**(46): p. 16180-16185.
60. Ma, B. and R. Nussinov, *Molecular dynamics simulations of alanine rich {beta}-sheet oligomers: Insight into amyloid formation*. Protein Science, 2002. **11**(10): p. 2335-2350.
61. Gsponer, J., U. Haberthuer, and A. Caflisch, *The role of side-chain interactions in the early steps of aggregation: Molecular dynamics simulations of an amyloid-forming peptide from the yeast prion Sup35*. Proceedings of the National Academy of Sciences of the United States of America, 2003. **100**(9): p. 5154-5159.
62. Klimov, D.K. and D. Thirumalai, *Dissecting the Assembly of A[beta]16-22 Amyloid Peptides into Antiparallel [beta] Sheets*. Structure, 2003. **11**(3): p. 295-307.
63. Petty, S.A. and S.M. Decatur, *Intersheet rearrangement of polypeptides during nucleation of beta-sheet aggregates*. Proceedings of the National Academy of Sciences of the United States of America, 2005. **102**(40): p. 14272-14277.
64. Cheon, M., et al., *Structural Reorganisation and Potential Toxicity of Oligomeric Species Formed during the Assembly of Amyloid Fibrils*. PLoS Computational Biology, 2007. **3**(9): p. e173.
65. Li, D.-W., et al., *Formation and Growth of Oligomers: A Monte Carlo Study of an Amyloid Tau Fragment*. PLoS Comput Biol, 2008. **4**(12): p. e1000238.
66. Nguyen, P.H., et al., *Monomer adds to preformed structured oligomers of Abeta-peptides by a two-stage dock-lock mechanism*. Proceedings of the National Academy of Sciences, 2007. **104**(1): p. 111-116.
67. Reddy, G., J.E. Straub, and D. Thirumalai, *Dynamics of locking of peptides onto growing amyloid fibrils*. Proceedings of the National Academy of Sciences, 2009: p. -.
68. Dupuis, N.F., et al., *Human islet amyloid polypeptide monomers form ordered beta-hairpins: a possible direct amyloidogenic precursor*. J Am Chem Soc, 2009. **131**(51): p. 18283-92.
69. Tarus, B., J.E. Straub, and D. Thirumalai, *Structures and free-energy landscapes of the wild type and mutants of the Abeta(21-30) peptide are determined by an interplay between intrapeptide electrostatic and hydrophobic interactions*. J Mol Biol, 2008. **379**(4): p. 815-29.

References

70. Lorenzo, A., et al., *Pancreatic islet cell toxicity of amylin associated with type-2 diabetes mellitus*. *Nature*, 1994. **368**(6473): p. 756-760.
71. Janson, J., et al., *The mechanism of islet amyloid polypeptide toxicity is membrane disruption by intermediate-sized toxic amyloid particles*. *Diabetes*, 1999. **48**(3): p. 491-498.
72. Saafi, E.L., et al., *Ultrastructural evidence that apoptosis is the mechanism by which human amylin evokes death in RINm5F pancreatic islet beta-cells*. *Cell Biology International*, 2001. **25**(4): p. 339-350.
73. Butler, A.E., et al., *Increased β -Cell Apoptosis Prevents Adaptive Increase in β -Cell Mass in Mouse Model of Type 2 Diabetes: Evidence for Role of Islet Amyloid Formation Rather Than Direct Action of Amyloid*. *Diabetes*, 2003. **52**(9): p. 2304-2314.
74. Knight, J.D., J.A. Hebda, and A.D. Miranker, *Conserved and Cooperative Assembly of Membrane-Bound Alpha-Helical States of Islet Amyloid Polypeptide*. *Biochemistry*, 2006. **45**(31): p. 9496-9508.
75. Meier, J.J., et al., *Inhibition of human IAPP fibril formation does not prevent beta-cell death: evidence for distinct actions of oligomers and fibrils of human IAPP*. *Am J Physiol Endocrinol Metab*, 2006. **291**(6): p. E1317-1324.
76. Mina, E.W. and C.G. Glabe, *Cellular Membranes as Targets in Amyloid Oligomer Disease Pathogenesis*, in *Advances in Alzheimer's and Parkinson's Disease* 2008. p. 381-386.
77. Kim, Y.J. and R. Takahashi, *Role of polyunsaturated fatty acids for misfolding protein aggregations - Implication for neurodegenerative diseases*, in *Integrated Molecular Medicine for Neuronal and Neoplastic Disorders* 2006. p. 11-20.
78. Ma, Z. and G.T. Westermark, *Effects of free fatty acid on polymerization of islet amyloid polypeptide (IAPP) in vitro and on amyloid fibril formation in cultivated isolated islets of transgenic mice overexpressing human IAPP*. *Mol Med*, 2002. **8**(12): p. 863-8.
79. Welch, K. and J. Yuan, *[alpha]-Synuclein oligomerization: a role for lipids?* *Trends in Neurosciences*, 2003. **26**(10): p. 517-519.
80. Johansson, A.S., et al., *Docosahexaenoic acid stabilizes soluble amyloid-beta protofibrils and sustains amyloid-beta-induced neurotoxicity in vitro*. *Febs Journal*, 2007. **274**(4): p. 990-1000.
81. Gellermann, G.P., et al., *Paired helical filaments contain small amounts of cholesterol, phosphatidylcholine and sphingolipids*. *Biological Chemistry*, 2006. **387**(9): p. 1267-1274.
82. Gellermann, G.P., et al., *Raft lipids as common components of human extracellular amyloid fibrils*. *Proceedings of the National Academy of Sciences of the United States of America*, 2005. **102**(18): p. 6297-6302.
83. Klein, T.R., et al., *Prion rods contain small amounts of two host sphingolipids as revealed by thin-layer chromatography and mass spectrometry*. *Biological Chemistry*, 1998. **379**(6): p. 655-666.
84. Sparr, E., et al., *Islet amyloid polypeptide-induced membrane leakage involves uptake of lipids by forming amyloid fibers*. *FEBS Letters*, 2004. **577**(1-2): p. 117-120.
85. Domanov, Y.A. and P.K.J. Kinnunen, *Islet Amyloid Polypeptide Forms Rigid Lipid-Protein Amyloid Fibrils on Supported Phospholipid Bilayers*. *Journal of Molecular Biology*, 2008. **376**(1): p. 42-54.

References

86. Jayasinghe, S.A. and R. Langen, *Lipid membranes modulate the structure of islet amyloid polypeptide*. *Biochemistry*, 2005. **44**(36): p. 12113-9.
87. Olofsson, A., et al., *Negatively Charged Phospholipid Membranes Induce Amyloid Formation of Medin via an [alpha]-Helical Intermediate*. *Journal of Molecular Biology*, 2007. **374**(1): p. 186-194.
88. Kaye, R., et al., *Conformational transitions of islet amyloid polypeptide (IAPP) in amyloid formation in vitro*. *J Mol Biol*, 1999. **287**(4): p. 781-96.
89. Knight, J.D. and A.D. Miranker, *Phospholipid Catalysis of Diabetic Amyloid Assembly*. *Journal of Molecular Biology*, 2004. **341**(5): p. 1175-1187.
90. Engel, M.F.M., et al., *Islet amyloid polypeptide inserts into phospholipid monolayers as monomer*. *Journal of Molecular Biology*, 2006. **356**(3): p. 783-789.
91. Anguiano, M., R.J. Nowak, and P.T. Lansbury, *Protofibrillar Islet Amyloid Polypeptide Permeabilizes Synthetic Vesicles by a Pore-like Mechanism that May Be Relevant to Type II Diabetes*. *Biochemistry*, 2002. **41**(38): p. 11338-11343.
92. Kagan, B.L., R. Azimov, and R. Azimova, *Amyloid Peptide Channels*. *Journal of Membrane Biology*, 2004. **202**(1): p. 1-10.
93. Quist, A., et al., *Amyloid ion channels: a common structural link for protein-misfolding disease*. *Proc Natl Acad Sci U S A*, 2005. **102**(30): p. 10427-32.
94. Mirzabekov, T.A., M.C. Lin, and B.L. Kagan, *Pore formation by the cytotoxic islet amyloid peptide amylin*. *J Biol Chem*, 1996. **271**(4): p. 1988-92.
95. Engel, M.F.M., et al., *Membrane damage by human islet amyloid polypeptide through fibril growth at the membrane*. *Proceedings of the National Academy of Sciences*, 2008: p. 0708354105.
96. Green, J.D., et al., *Atomic force microscopy reveals defects within mica supported lipid bilayers induced by the amyloidogenic human amylin peptide*. *Journal of Molecular Biology*, 2004. **342**(3): p. 877-887.
97. Taylor, M., et al., *Development of a proteolytically stable retro-inverso peptide inhibitor of beta-amyloid oligomerization as a potential novel treatment for Alzheimer's disease*. *Biochemistry*, 2010. **49**(15): p. 3261-72.
98. Li, H., et al., *Biophysical characterization of Abeta42 C-terminal fragments: inhibitors of Abeta42 neurotoxicity*. *Biochemistry*, 2010. **49**(6): p. 1259-67.
99. Tatarek-Nossol, M., et al., *Inhibition of hIAPP Amyloid-Fibril Formation and Apoptotic Cell Death by a Designed hIAPP Amyloid- Core-Containing Hexapeptide*. *Chemistry & Biology*, 2005. **12**(7): p. 797-809.
100. Taniguchi, S., et al., *Inhibition of heparin-induced tau filament formation by phenothiazines, polyphenols, and porphyrins*. *J Biol Chem*, 2005. **280**(9): p. 7614-23.
101. Mishra, R., et al., *Small-molecule inhibitors of islet amyloid polypeptide fibril formation*. *Angew Chem Int Ed Engl*, 2008. **47**(25): p. 4679-82.
102. Mishra, R., et al., *Inhibiting islet amyloid polypeptide fibril formation by the red wine compound resveratrol*. *Chembiochem*, 2009. **10**(3): p. 445-9.
103. Jiang, P., et al., *pH-Dependent interactions of human islet amyloid polypeptide segments with insulin studied by replica exchange molecular dynamics simulations*. *J Phys Chem B*, 2010. **114**(31): p. 10176-83.
104. Wei, L., et al., *Residual Structure in Islet Amyloid Polypeptide Mediates Its Interactions with Soluble Insulin*. *Biochemistry*, 2009. **48**(11): p. 2368-2376.

References

105. Saraogi, I., et al., *Synthetic α -Helix Mimetics as Agonists and Antagonists of Islet Amyloid Polypeptide Aggregation*. *Angewandte Chemie*, 2010. **122**(4): p. 748-751.
106. Luheshi, L.M., et al., *Sequestration of the A β Peptide Prevents Toxicity and Promotes Degradation In Vivo*. *PLoS Biol*, 2010. **8**(3): p. e1000334.
107. Porat, Y., A. Abramowitz, and E. Gazit, *Inhibition of amyloid fibril formation by polyphenols: structural similarity and aromatic interactions as a common inhibition mechanism*. *Chem Biol Drug Des*, 2006. **67**(1): p. 27-37.
108. Evers, F., et al., *Elucidating the Mechanism of Lipid Membrane-Induced IAPP Fibrillogenesis and Its Inhibition by the Red Wine Compound Resveratrol: A Synchrotron X-ray Reflectivity Study*. *Journal of the American Chemical Society*, 2009. **131**(27): p. 9516-9521.
109. Esteras-Chopo, A., et al., *A Molecular Dynamics Study of the Interaction of d-Peptide Amyloid Inhibitors with Their Target Sequence Reveals a Potential Inhibitory Pharmacophore Conformation*. *Journal of Molecular Biology*, 2008. **383**(1): p. 266-280.
110. Wu, C., et al., *Binding Modes of Thioflavin-T to the Single-Layer [β]-Sheet of the Peptide Self-Assembly Mimics*. *Journal of Molecular Biology*, 2009. **394**(4): p. 627-633.
111. Wu, C., et al., *The Binding of Thioflavin T and Its Neutral Analog BTA-1 to Protofibrils of the Alzheimer's Disease A β 16-22 Peptide Probed by Molecular Dynamics Simulations*. *Journal of Molecular Biology*, 2008. **384**(3): p. 718-729.
112. Wu, C., et al., *Dual Binding Modes of Congo Red to Amyloid Protofibril Surface Observed in Molecular Dynamics Simulations*. *Journal of the American Chemical Society*, 2007. **129**(5): p. 1225-1232.
113. Chang, W.E., et al., *Molecular Dynamics Simulations of Anti-Aggregation Effect of Ibuprofen*. *Biophysical Journal*, 2010. **98**(11): p. 2662-2670.
114. Lemkul, J.A. and D.R. Bevan, *Destabilizing Alzheimer's A β 42 Protofibrils with Morin: Mechanistic Insights from Molecular Dynamics Simulations*. *Biochemistry*, 2010. **49**(18): p. 3935-3946.
115. Convertino, M., et al., *9,10-Anthraquinone hinders beta-aggregation: how does a small molecule interfere with Abeta-peptide amyloid fibrillation?* *Protein Sci*, 2009. **18**(4): p. 792-800.
116. Schlick, T., *Molecular Modeling and Simulation: An Interdisciplinary Guide* 2002: Springer-Verlag New York, Inc. 656.
117. Ponder, J.W. and D.A. Case, *Force fields for protein simulations*, in *Protein Simulations* 2003. p. 27-85.
118. McCammon, J.A., B.R. Gelin, and M. Karplus, *Dynamics of folded proteins*. *Nature*, 1977. **267**(5612): p. 585-590.
119. Karplus, M. and J.A. McCammon, *Molecular dynamics simulations of biomolecules*. *Nat Struct Mol Biol*, 2002. **9**(9): p. 646-652.
120. Rhee, Y.M. and V.S. Pande, *Multiplexed-Replica Exchange Molecular Dynamics Method for Protein Folding Simulation*. *Biophys. J.*, 2003. **84**(2): p. 775-786.
121. Periole, X. and A.E. Mark, *Convergence and sampling efficiency in replica exchange simulations of peptide folding in explicit solvent*. *The Journal of Chemical Physics*, 2007. **126**(1): p. 014903-11.

References

122. Rao, F. and A. Caflisch, *Replica exchange molecular dynamics simulations of reversible folding*. The Journal of Chemical Physics, 2003. **119**(7): p. 4035-4042.
123. Seibert, M.M., et al., *Reproducible Polypeptide Folding and Structure Prediction using Molecular Dynamics Simulations*. Journal of Molecular Biology, 2005. **354**(1): p. 173-183.
124. Zhang, W., C. Wu, and Y. Duan, *Convergence of replica exchange molecular dynamics*. The Journal of Chemical Physics, 2005. **123**(15): p. 154105-9.
125. Nymeyer, H., *How Efficient Is Replica Exchange Molecular Dynamics? An Analytic Approach*. J. Chem. Theory Comput., 2008. **4**(4): p. 626-636.
126. Zheng, W., et al., *Simulating replica exchange simulations of protein folding with a kinetic network model*. Proceedings of the National Academy of Sciences, 2007. **104**(39): p. 15340-15345.
127. Trebst, S., M. Troyer, and U.H.E. Hansmann, *Optimized parallel tempering simulations of proteins*. The Journal of Chemical Physics, 2006. **124**(17): p. 174903-6.
128. Sindhikara, D., Y. Meng, and A.E. Roitberg, *Exchange frequency in replica exchange molecular dynamics*. The Journal of Chemical Physics, 2008. **128**(2): p. 024103-10.
129. David Van Der Spoel, E.L., Berk Hess, Gerrit Groenhof, Alan E. Mark Herman, J. C. Berendsen, *GROMACS: Fast, flexible, and free*. Journal of Computational Chemistry, 2005. **26**(16): p. 1701-1718.
130. Kabsch, W. and C. Sander, *Dictionary of protein secondary structure: Pattern recognition of hydrogen-bonded and geometrical features*. Biopolymers, 1983. **22**(12): p. 2577-2637.
131. Mu, Y., P.H. Nguyen, and G. Stock, *Energy landscape of a small peptide revealed by dihedral angle principal component analysis*. Proteins, 2005. **58**(1): p. 45-52.
132. Onufriev, A., D. Bashford, and D.A. Case, *Exploring protein native states and large-scale conformational changes with a modified generalized born model*. Proteins, 2004. **55**(2): p. 383-94.
133. D.A. Case, T.A.D., T.E. Cheatham, III, C.L. Simmerling, J. Wang, R.E. Duke, R. Luo, K.M. Merz, D.A. Pearlman, M. Crowley, R.C. Walker, W. Zhang, B. Wang, S. Hayik, A. Roitberg, G. Seabra, K.F. Wong, F. Paesani, X. Wu, S. Brozell, V. Tsui, H. Gohlke, L. Yang, C. Tan, J. Mongan, V. Hornak, G. Cui, P. Beroza, D.H. Mathews, C. Schafmeister, W.S. Ross, and P.A. Kollman, *AMBER 9*. University of California, San Francisco, 2006.
134. Berendsen, H.J.C., et al., *Interaction models for water in relation to protein hydration*. Intermolecular Forces, 1981: p. 331-342.
135. Lindahl, E., B. Hess, and D. van der Spoel, *GROMACS 3.0: a package for molecular simulation and trajectory analysis*. Journal of Molecular Modeling, 2001. **7**(8): p. 306-317.
136. Jorgensen, W.L. and J. Tirado-Rives, *The OPLS [optimized potentials for liquid simulations] potential functions for proteins, energy minimizations for crystals of cyclic peptides and crambin*. J. Am. Chem. Soc., 1988. **110**(6): p. 1657-1666.
137. Jorgensen, W.L., D.S. Maxwell, and J. Tirado-Rives, *Development and Testing of the OPLS All-Atom Force Field on Conformational Energetics and Properties of Organic Liquids*. J. Am. Chem. Soc., 1996. **118**(45): p. 11225-11236.

References

138. Hess, B., et al., *LINCS: A linear constraint solver for molecular simulations*. Journal of Computational Chemistry, 1997. **18**(12): p. 1463-1472.
139. Darden, T., D. York, and L. Pedersen, *Particle mesh Ewald: An $N \cdot \log(N)$ method for Ewald sums in large systems*. The Journal of Chemical Physics, 1993. **98**(12): p. 10089-10092.
140. Betsholtz, C., et al., *Sequence divergence in a specific region of islet amyloid polypeptide (IAPP) explains differences in islet amyloid formation between species*. FEBS Lett, 1989. **251**(1-2): p. 261-4.
141. Ritzel, R.A., et al., *Human islet amyloid polypeptide oligomers disrupt cell coupling, induce apoptosis, and impair insulin secretion in isolated human islets*. Diabetes, 2007. **56**(1): p. 65-71.
142. Humphrey, W., A. Dalke, and K. Schulten, *VMD: visual molecular dynamics*. J Mol Graph, 1996. **14**(1): p. 33-8, 27-8.
143. Ashburn, T.T., M. Auger, and P.T. Lansbury, *The structural basis of pancreatic amyloid formation: isotope-edited spectroscopy in the solid state*. J. Am. Chem. Soc., 1992. **114**(2): p. 790-791.
144. Griffiths, J.M., et al., *Rotational Resonance Solid-State NMR Elucidates a Structural Model of Pancreatic Amyloid*. J. Am. Chem. Soc., 1995. **117**(12): p. 3539-3546.
145. Jack, E., et al., *The Organization of Aromatic Side Groups in an Amyloid Fibril Probed by Solid-State ^2H and ^{19}F NMR Spectroscopy*. J. Am. Chem. Soc., 2006. **128**(25): p. 8098-8099.
146. Madine, J., et al., *Structural Insights into the Polymorphism of Amyloid-Like Fibrils Formed by Region 20-29 of Amylin Revealed by Solid-State NMR and X-ray Fiber Diffraction*. Journal of the American Chemical Society, 2008. **130**(45): p. 14990-15001.
147. Wu, C., H. Lei, and Y. Duan, *Formation of partially ordered oligomers of amyloidogenic hexapeptide (NFGAIL) in aqueous solution observed in molecular dynamics simulations*. Biophys J, 2004. **87**(5): p. 3000-9.
148. Cecchini, M., et al., *Replica exchange molecular dynamics simulations of amyloid peptide aggregation*. J Chem Phys, 2004. **121**(21): p. 10748-56.
149. Kameda, T. and S. Takada, *Secondary structure provides a template for the folding of nearby polypeptides*. Proc Natl Acad Sci U S A, 2006. **103**(47): p. 17765-70.
150. Sharon, R., et al., *The Formation of Highly Soluble Oligomers of α -Synuclein Is Regulated by Fatty Acids and Enhanced in Parkinson's Disease*. 2003. **37**(4): p. 583-595.
151. Welch, K. and J. Yuan, *α -Synuclein oligomerization: a role for lipids?* Trends in Neurosciences, 2003. **26**(10): p. 517-519.
152. Nanga, R.P.R., et al., *Structures of Rat and Human Islet Amyloid Polypeptide IAPP1-19 in Micelles by NMR Spectroscopy*. Biochemistry, 2008. **47**(48): p. 12689-12697.
153. Alakoskela, J.-M., et al., *Characteristics of Fibers Formed by Cytochrome c and Induced by Anionic Phospholipids* Biochemistry, 2006. **45**(45): p. 13447-13453.
154. Zhao, H., E.K.J. Tuominen, and P.K.J. Kinnunen, *Formation of Amyloid Fibers Triggered by Phosphatidylserine-Containing Membranes*. Biochemistry, 2004. **43**(32): p. 10302-10307.
155. Radovan, D., N. Opitz, and R. Winter, *Fluorescence microscopy studies on islet amyloid polypeptide fibrillation at heterogeneous and cellular*

References

- membrane interfaces and its inhibition by resveratrol. *FEBS Lett*, 2009. **583**(9): p. 1439-45.
156. Tenidis, K., et al., *Identification of a penta- and hexapeptide of islet amyloid polypeptide (IAPP) with amyloidogenic and cytotoxic properties*. *Journal of Molecular Biology*, 2000. **295**(4): p. 1055-1071.
 157. Gazit, E., *Mechanisms of amyloid fibril self-assembly and inhibition. Model short peptides as a key research tool*. *FEBS J*, 2005. **272**(23): p. 5971-8.
 158. Shao, Y., et al., *Advances in methods and algorithms in a modern quantum chemistry program package*. *Physical Chemistry Chemical Physics*, 2006. **8**(27): p. 3172-3191.
 159. M. J. Frisch, G.W.T., H. B. Schlegel, G. E. Scuseria, M. A. Robb, J. R. Cheeseman, G. Scalmani, V. Barone, B. Mennucci, G. A. Petersson, H. Nakatsuji, M. Caricato, X. Li, H. P. Hratchian, A. F. Izmaylov, J. Bloino, G. Zheng, J. L. Sonnenberg, M. Hada, M. Ehara, K. Toyota, R. Fukuda, J. Hasegawa, M. Ishida, T. Nakajima, Y. Honda, O. Kitao, H. Nakai, T. Vreven, J. A. Montgomery, Jr., J. E. Peralta, F. Ogliaro, M. Bearpark, J. J. Heyd, E. Brothers, K. N. Kudin, V. N. Staroverov, R. Kobayashi, J. Normand, K. Raghavachari, A. Rendell, J. C. Burant, S. S. Iyengar, J. Tomasi, M. Cossi, N. Rega, J. M. Millam, M. Klene, J. E. Knox, J. B. Cross, V. Bakken, C. Adamo, J. Jaramillo, R. Gomperts, R. E. Stratmann, O. Yazyev, A. J. Austin, R. Cammi, C. Pomelli, J. W. Ochterski, R. L. Martin, K. Morokuma, V. G. Zakrzewski, G. A. Voth, P. Salvador, J. J. Dannenberg, S. Dapprich, A. D. Daniels, Ö. Farkas, J. B. Foresman, J. V. Ortiz, J. Cioslowski, and D. J. Fox, , *Gaussian 09. Gaussian, Inc., Wallingford CT*. 2009.
 160. Dupradeau, F.Y., et al., *The R.E.D. tools: advances in RESP and ESP charge derivation and force field library building*. *Physical Chemistry Chemical Physics*, 2010. **12**(28): p. 7821-7839.
 161. Kaminski, G.A., et al., *Evaluation and Reparametrization of the OPLS-AA Force Field for Proteins via Comparison with Accurate Quantum Chemical Calculations on Peptides*. *Journal of Physical Chemistry B*, 2001. **105**(28): p. 6474-6487.
 162. Frisch, G.S.a.M.J., *A continuous surface charge formalism for the polarizable continuum model of solvation*. in prep, 2009.
 163. Steinbrecher, T., D.L. Mobley, and D.A. Case, *Nonlinear scaling schemes for Lennard-Jones interactions in free energy calculations*. *J Chem Phys*, 2007. **127**(21): p. 214108.
 164. Mobley, D.L., et al., *Small molecule hydration free energies in explicit solvent: An extensive test of fixed-charge atomistic simulations*. *J Chem Theory Comput*, 2009. **5**(2): p. 350-358.
 165. Lanning, J.D., et al., *Chaperone-like N-methyl peptide inhibitors of polyglutamine aggregation*. *Biochemistry*, 2010. **49**(33): p. 7108-18.
 166. Nelson, R. and D. Eisenberg, *Recent atomic models of amyloid fibril structure*. *Current Opinion in Structural Biology*, 2006. **16**(2): p. 260-265.
 167. Nelson, R., et al., *Structure of the cross-beta spine of amyloid-like fibrils*. *Nature*, 2005. **435**(7043): p. 773-778.
 168. Lukinius, A., et al., *Co-localization of islet amyloid polypeptide and insulin in the B cell secretory granules of the human pancreatic islets*. *Diabetologia*, 1989. **32**(4): p. 240-244.
 169. Nishi, M., et al., *Conservation of the Sequence of Islet Amyloid Polypeptide in Five Mammals is Consistent with Its Putative Role as an Islet Hormone*.

References

- Proceedings of the National Academy of Sciences, 1989. **86**(15): p. 5738-5742.
170. Knight, J.D., J.A. Williamson, and A.D. Miranker, *Interaction of membrane-bound islet amyloid polypeptide with soluble and crystalline insulin*. Protein Sci, 2008. **17**(10): p. 1850-1856.
 171. Westermark, P., et al., *Effects of beta cell granule components on human islet amyloid polypeptide fibril formation*. FEBS Lett, 1996. **379**(3): p. 203-6.
 172. Janciauskiene, S., et al., *B cell granule peptides affect human islet amyloid polypeptide (IAPP) fibril formation in vitro*. Biochem Biophys Res Commun, 1997. **236**(3): p. 580-5.
 173. Smith, G.D., W.A. Pangborn, and R.H. Blessing, *The structure of T6 human insulin at 1.0 Å resolution*. Acta Crystallogr D Biol Crystallogr, 2003. **59**(Pt 3): p. 474-82.
 174. Gilead, S., H. Wolfenson, and E. Gazit, *Molecular mapping of the recognition interface between the islet amyloid polypeptide and insulin*. Angew Chem Int Ed Engl, 2006. **45**(39): p. 6476-80.
 175. Stites, W.E., *Protein-protein Interactions: Interface Structure, Binding Thermodynamics, and Mutational Analysis*. Chemical Reviews, 1997. **97**(5): p. 1233-1250.
 176. Singh, N.J., et al., *Comprehensive Energy Analysis for Various Types of pi-Interaction*. Journal of Chemical Theory and Computation, 2009. **5**(3): p. 515-529.
 177. Wiltzius, J.J., et al., *Atomic structures of IAPP (amylin) fusions suggest a mechanism for fibrillation and the role of insulin in the process*. Protein Sci, 2009. **18**(7): p. 1521-30.
 178. Wiltzius, J.J.W., et al., *Atomic structure of the cross-beta spine of islet amyloid polypeptide (amylin)*. Protein Sci, 2008. **17**(9): p. 1467-1474.
 179. Alessandro Mascioni, F.P.U.I.A.R.G.V., *Conformational preferences of the amylin nucleation site in SDS micelles: An NMR study*. Biopolymers, 2003. **69**(1): p. 29-41.
 180. U. Ilangovan, A.R., *Conformational studies of human islet amyloid peptide using molecular dynamics and simulated annealing methods*. Biopolymers, 1998. **45**(1): p. 9-20.
 181. Lomakin, A., et al., *On the nucleation and growth of amyloid beta-protein fibrils: detection of nuclei and quantitation of rate constants*. Proc Natl Acad Sci U S A, 1996. **93**(3): p. 1125-9.
 182. Ladiwala, A.R.A., et al., *Resveratrol Selectively Remodels Soluble Oligomers and Fibrils of Amyloid A beta into Off-pathway Conformers*. Journal of Biological Chemistry, 2010. **285**(31): p. 24228-24237.
 183. Jiang, P., W.X. Xu, and Y.G. Mu, *Amyloidogenesis Abolished by Proline Substitutions but Enhanced by Lipid Binding*. PLoS Computational Biology, 2009. **5**(4): p. e1000357.
 184. Campioni, S., et al., *A causative link between the structure of aberrant protein oligomers and their toxicity*. Nature Chemical Biology, 2010. **6**(2): p. 140-147.
 185. Paravastu, A.K., et al., *Molecular structural basis for polymorphism in Alzheimer's beta-amyloid fibrils*. Proceedings of the National Academy of Sciences of the United States of America, 2008. **105**(47): p. 18349-18354.
 186. Ritter, C., et al., *Correlation of structural elements and infectivity of the HET-s prion*. Nature, 2005. **435**(7043): p. 844-848.

References

187. Sawaya, M.R., et al., *Atomic structures of amyloid cross-beta spines reveal varied steric zippers*. Nature, 2007. **447**(7143): p. 453-457.
188. Jahn, T.R., et al., *The Common Architecture of Cross-beta Amyloid*. Journal of Molecular Biology, 2010. **395**(4): p. 717-727.
189. Meng, F.L., et al., *The Flavanol (-)-Epigallocatechin 3-Gallate Inhibits Amyloid Formation by Islet Amyloid Polypeptide, Disaggregates Amyloid Fibrils, and Protects Cultured Cells against IAPP-Induced Toxicity*. Biochemistry, 2010. **49**(37): p. 8127-8133.
190. Ehrnhoefer, D.E., et al., *EGCG redirects amyloidogenic polypeptides into unstructured, off-pathway oligomers*. Nature Structural & Molecular Biology, 2008. **15**(6): p. 558-566.
191. Roberts, B.E., et al., *A synergistic small-molecule combination directly eradicates diverse prion strain structures*. Nature Chemical Biology, 2009. **5**(12): p. 936-946.
192. Knight, J.D., J.A. Williamson, and A.D. Miranker, *Interaction of membrane-bound islet amyloid polypeptide with soluble and crystalline insulin*. Protein Sci, 2008. **17**(10): p. 1850-6.
193. Brender, J.R., et al., *A Single Mutation in the Nonamyloidogenic Region of Islet Amyloid Polypeptide Greatly Reduces Toxicity*. Biochemistry, 2008. **47**(48): p. 12680-12688.
194. Apostolidou, M., S.A. Jayasinghe, and R. Langen, *Structure of {alpha}-Helical Membrane-bound Human Islet Amyloid Polypeptide and Its Implications for Membrane-mediated Misfolding*. J. Biol. Chem., 2008. **283**(25): p. 17205-17210.
195. Engel, M.F.M., *Membrane permeabilization by Islet Amyloid Polypeptide*. Chemistry and Physics of Lipids, 2009. **160**(1): p. 1-10.
196. Abedini, A. and D.P. Raleigh, *The Role of His-18 in Amyloid Formation by Human Islet Amyloid Polypeptide*. Biochemistry, 2005. **44**(49): p. 16284-16291.
197. Garcia, A.E. and K.Y. Sanbonmatsu, *Alpha-helical stabilization by side chain shielding of backbone hydrogen bonds*. Proc Natl Acad Sci U S A, 2002. **99**(5): p. 2782-7.
198. Lin, Z., et al., *Solution structure of eggcase silk protein and its implications for silk fiber formation*. Proceedings of the National Academy of Sciences, 2009. **106**(22): p. 8906-11.

Publications

1. **Jiang, P.**, Li, W., Shea, J.-E. & Mu, Y. Resveratrol inhibits the formation of multiple-layered β -sheet oligomers of the human islet amyloid polypeptide segment 22-27. *Submitted*.
2. **Jiang, P.**, Wei, L., Pervushin, K. & Mu, Y. (2010). pH-dependent interactions of human islet amyloid polypeptide segments with insulin studied by replica exchange molecular dynamics simulations. *J Phys Chem B* 114, 10176-83.
3. **Jiang, P.**, Xu, W. & Mu, Y. (2009). Amyloidogenesis abolished by proline substitutions but enhanced by lipid binding. *PLoS Comput Biol* 5, e1000357.
4. Wei, L., **Jiang, P.**, Yau, Y. H., Summer, H., Shochat, S. G., Mu, Y. & Pervushin, K. (2009). Residual structure in islet amyloid polypeptide mediates its interactions with soluble insulin. *Biochemistry* 48, 2368-76.
5. Xu, W., **Jiang, P.** & Mu, Y. (2009). Conformation preorganization: effects of S20G mutation on the structure of human islet amyloid polypeptide segment. *J Phys Chem B* 113, 7308-14.
6. Xu, W., **Jiang, P.**, Li, W. & Mu, Y. (2009). Assembly dynamics of two-beta sheets revealed by molecular dynamics simulations. *J Chem Phys* 130, 164709.
7. Wu, B., **Jiang, P.**, Mu, Y. & Wilmouth, R. C. (2009). Cancer Osaka thyroid (Cot) phosphorylates Polo-like kinase (PLK1) at Ser137 but not at Thr210. *Biol Chem* 390, 1271-7.
8. Bai, Y., Liu, S., **Jiang, P.**, Zhou, L., Li, J., Tang, C., Verma, C., Mu, Y., Beuerman, R. W. & Pervushin, K. (2009). Structure-dependent charge density as a determinant of antimicrobial activity of peptide analogues of defensin. *Biochemistry* 48, 7229-39.